



HAL
open science

Cavitation & supercavitation : obtenir un projectile profilé stable

Thibault Guillet

► **To cite this version:**

Thibault Guillet. Cavitation & supercavitation : obtenir un projectile profilé stable. Fluid mechanics [physics.class-ph]. Institut Polytechnique de Paris, 2019. English. NNT : 2019IPPAX007 . tel-02511334

HAL Id: tel-02511334

<https://theses.hal.science/tel-02511334>

Submitted on 18 Mar 2020

HAL is a multi-disciplinary open access archive for the deposit and dissemination of scientific research documents, whether they are published or not. The documents may come from teaching and research institutions in France or abroad, or from public or private research centers.

L'archive ouverte pluridisciplinaire **HAL**, est destinée au dépôt et à la diffusion de documents scientifiques de niveau recherche, publiés ou non, émanant des établissements d'enseignement et de recherche français ou étrangers, des laboratoires publics ou privés.



INSTITUT
POLYTECHNIQUE
DE PARIS

NNT : 2019IPPAX007

Thèse de doctorat



Cavitation & Supercavitation : From a bluff to a stable streamlined projectile

Thèse de doctorat de l'Institut Polytechnique de Paris
préparée à l'École polytechnique

École doctorale n°626 École Doctorale de l'Institut Polytechnique de Paris (ED IP
Paris)

Spécialité de doctorat : Ingénierie Mécanique et Énergétique

Thèse présentée et soutenue à Palaiseau, le 19 décembre 2019, par

THIBAUT GUILLET

Composition du Jury :

Detlef Lohse Professeur, University of Twente	Président
Irmgard Bischofberger Professeure assistante, Massachusetts Institute of Technology	Rapporteure
Olivier Cadot Professeur, University of Liverpool	Rapporteur
Sunghwang Jung Professeur associé, Cornell University	Examineur
Christophe Clanet Directeur de Recherche, École polytechnique	Directeur de thèse
Caroline Cohen Professeure Assistante, École polytechnique	Co-directrice de thèse
David Quéré Directeur de Recherche, ESPCI	Co-encadrant

Remerciements

Firstly, I would like to thank all the jury members to have made it to the campus during the worst times of the French public transportations strike. Thanks to Irmgard Bishofberger and Olivier Cadot for carefully reading the manuscript and for their remarks. I would like to thank Detlef Lohse for his questions and remarks which will really impact the continuation of this work. I acknowledge Sunny Jung for his comments and for accepting to follow the defense through skype.

Je souhaiterais remercier David de m'avoir communiqué sa passion pour la science, la recherche et les matières molles : sans sa contribution, je ne me serais jamais lancé dans l'aventure de la thèse. Merci de m'avoir envoyé chez Sid Nagel à Chicago en stage de troisième année : tu m'as donné l'opportunité de faire mes premiers pas dans la recherche dans une équipe formidable. Pendant la thèse, malgré ton emploi du temps extrêmement chargé, tu as toujours répondu présent (tout du moins après un nombre d'appels suffisant). Tu as la fantastique capacité de sublimer le travail de tes thésards et thésardes ; j'espère avoir appris ne serait-ce qu'une infime partie de tes talents de rédaction.

Merci beaucoup à Christophe. Je ne sais pas trop comment tu résumerais cette thèse ... J'hésite entre "on a pas beaucoup avancé, mais on a bien rigolé !" ou "c'était super mais on a rien compris". Plus sérieusement, un grand merci pour toutes les fois où tu m'as sorti de galères : théoriques, numériques ou expérimentales. Je ressortais toujours de ton bureau avec plein de nouvelles idées - pas toujours bonnes - mais surtout en ayant fait le plein de motivation. Merci aussi d'avoir désamorcé les situations administratives compliquées, comme lorsqu'au mois de juin, trois de tes thésardes et thésards n'étaient toujours pas inscrits à l'école doctorale.

Un grand merci à Caroline : je ne sais pas trop comment je pourrais résumer tout ce que tu m'as apporté pendant ces trois ans. Merci pour tous les moments que nous avons passé à discuter des projets de thèse : simulations, modèles et surtout expériences. Et on n'a pas fait qu'en discuter : depuis les expériences faites à RedBull à Los Angeles, jusqu'aux tests où il fallait frapper le plus fort possible contre les murs du préfa (pas toujours avec les poings), en passant par le voyage en Autriche ! Tu fais partie de ces chercheurs et chercheuses qui s'émerveillent devant toutes les expériences : cela est très motivant ! Particularité spéciale : plus le dispositif est à l'arrache, plus il te plaît !

Un immense merci à Juliette : tu as fait énormément pour cette thèse. Grâce à toi, le dispositif expérimental final est impressionnant : il t'aura fallu moins d'une semaine pour démontrer que le dispositif initial de ton stage, préparé pendant plusieurs semaine avec Caroline, était inopérant ... Sans ton apport, cette thèse ne serait pas grand chose. Merci aussi de m'avoir aidé sur les autres projets, en particulier à monter le canal pendant plusieurs jours (semaines ?). Ce fut un plaisir de travailler avec toi et je te souhaite le meilleur pour la suite de ta thèse : je serai ravi de suivre tes avancées.

Merci à Kevin : ton implication dans ma thèse ne transparait que très peu et pourtant je sais qu'elle a été déterminante. Tu as toujours pris de ton temps libre pour essayer de répondre à mes questions, qu'elles soient stupides ou extrêmement complexes. Tu es très généreux : tu fais des problèmes des autres tes problèmes. J'aurais aimé pouvoir t'aider autant que tu m'a aidé ... Je te souhaite beaucoup de courage pour l'année difficile qui se présente.

Un grand merci à Romain : sans toi aucun de mes dispositifs expérimentaux n'auraient leur forme actuelle. C'était toujours agréable de faire des tours au centre de tri afin de récupérer des matériaux pour les expériences. Et bien entendu, à chaque passage, nous récupérions au moins : un écran de PC, une bobine avec un coeur en fonte de 10 kg et un appareil électronique qui encombrerait le préfa pendant 3 mois avant de retourner à la décharge ... Je te souhaite plein de réussite pour Phyling !

Merci à Martin de m'avoir permis de rentrer doucement dans la thèse avec un projet qu'il avait déjà débuté. Merci pour l'aide que tu m'a apporté pour la réalisations des expériences et pour l'écriture de l'article.

Merci beaucoup à Pierre et Ambre : ce fut un plaisir de partager ces trois années avec vous. Des meilleurs moments (apéros, soirées pizzas...) aux plus affreux (une journée avec les pieds mouillés passée proche de Saporò).

Merci à tous les membres du préfa : Tim pour nos échanges sur les arcanes du web et pour ton aide dans le combat permanent pour le réglage du thermostat, JiPhi pour toute l'aide que tu m'a apporté et pour tes scuds, Tom pour les bons moments passés en déplacements, Bcube pour tes leçons de beatbox. Ainsi qu'aux nouveaux occupants, Charlie et Antoine, j'espère que vous perpétuerez les bonnes traditions du préfa. Un grand merci aux membres de la compagnie des interfaces que j'aurais aimé pouvoir côtoyer plus souvent : Joachim, Pierre, Saurabh et Aditya...

Je souhaiterais remercier particulièrement les ITA du LadhyX qui ont toujours été présents lorsque j'ai eu besoin d'eux. Un grand merci à Sandrine, Magali et Delphine : particulièrement lorsqu'il a fallu gérer la commande BMP. Un grand merci à Caroline pour toute l'aide qu'elle m'a apportée dans la conception des différentes pièces des dispositifs expérimentaux, à Dani et Toai pour leur soutien IT, à Avin et Antoine qui ont dû s'arracher les cheveux avec la sécurité du préfa.

Merci à Guilhem qui m'a fait confiance pour encadrer l'équipe représentant l'X à l'IPT pendant trois ans aux côtés de Daniel et Fabian. Cette expérience a été extrêmement enrichissante ! Un grand merci aux élèves, j'espère que vous aurez autant appris que moi et que vous garderez un bon souvenir de vos après-midis au préfa. Pour la première année : Corentin, Lucien, Pierre, Félix, Déborah et Alexis ; pour la deuxième année : Quentin, Fang, Clément, Julie, Angel, Anthony et Amaury pour la deuxième année ; pour la dernière année : Mathieu, Tristan, Kyrlo, Han Yu et Alexandre.

Merci aux anciens de l'équipe : Jacopo, Raphaëlle et Guillaume. Vous avez tout de suite répondu présent pour discuter de vos parcours et vous m'avez beaucoup aidé à faire mon choix.

Un grand merci à tous mes coéquipiers du Vincennes Volley Club qui m'ont aidé à me vider la tête pendant ces trois années de thèse. Je souhaite remercier particulièrement Eric qui m'a beaucoup aidé au moment de rejoindre SGR.

Merci beaucoup à tous mes amis pour tous les moments que j'ai pu passer avec eux pendant ces trois années et pour le soutien qu'ils m'ont apporté. Merci à Pierre-Philippe pour les weekends de l'intelligence et pour tout le reste. Merci à Louis pour les soirées raclettes, bonnes bouffes et jeux. Merci aussi à Paul et Agathe pour les soirées jeux (j'espère qu'on finira par éradiquer toutes ces maladies), Eric et Léa pour les moments de souffrance partagés en montagne, Marco, Caro, Léo, Nicolas, Guillaume et Martina même si on ne vous voit plus, Côme et toute sa famille rémoise, Louis, Samuel et toutes les autres personnes qui comptent pour moi.

Enfin, merci à ma famille. En particulier à mes parents, qui, même s'ils n'ont pas toujours compris ce que je faisais, ont toujours été là pour me soutenir, spécialement quand j'étais à l'étranger. J'espère avoir hérité d'une petite partie de l'optimisme et du dynamisme de mon père ainsi que la rigueur et l'organisation de ma mère. Merci à vous, ainsi qu'aux parents de Lucie, d'avoir participé à l'organisation du pot.

Merci à mes grands-parents, je sais que vous auriez tous aimé être présent pour voir un de vos petit-fils devenir docteur. Merci pour tous ce que vous avez fait pour moi quand j'étais petit : vacances à Royan, lectures dans le lit, après-midis à aller voir passer les trains ... J'ai beaucoup appris de vous. Je vous souhaite plein de bonheur.

Merci à Philippe de m'avoir introduit à l'escalade, au surf, au longboard ... Je souhaite aussi remercier tout le reste de ma famille, qui sera toujours là pour me soutenir.

Merci à mes deux frères qui m'ont toujours poussé à me dépasser. Depuis mon plus jeune âge quand Nicolas me faisait croire qu'il me poussait en vélo alors qu'en fait il venait de m'apprendre à en faire. Jusqu'à quelques mois en arrière, lorsque Henri a su trouver les mots, et peut être les médicaments aussi, pour me faire arriver au sommet du Mont-Blanc, alors que ce n'était pas gagné vu mon état en entrant dans le refuge Vallot.

Merci à Chameau de s'assurer que je suis bien réveillé tout les matins. Saches seulement que le matin peut commencer plus tard que 5h30, surtout le weekend.

Merci à Lucie de partager ma vie et de faire en sorte que chaque jour soit meilleur que le précédent : tu es la meilleure des équipières.

Résumé substantiel

Les sous-marins, bien qu’existants depuis plus de 100 ans, n’ont que peu évolués dans leur forme. Etant des véhicules non-profilés, et, aux vues de l’évolution de leur vitesse maximale, on peut se demander s’ils parviendront à dépasser la vitesse de 100 m/s.

En effet, pour un objet non-profilé métrique, la puissance nécessaire pour atteindre cette vitesse est d’environ 1 GW. Cependant, il est connu que l’utilisation de carénages autour d’un corps non-profilé permet de diminuer la trainée qu’il subit par un facteur 10. Ce gain substantiel est directement retranscrit sur la puissance de propulsion nécessaire pour se déplacer à une vitesse donnée. Ce gain, appliqué à un sous-marin, permettrait d’envisager qu’il se déplace à 100 m/s. Cette thèse a pour objectif de déterminer s’il est possible d’obtenir de telles réductions de trainée grâce à la présence d’une bulle de gaz, éventuellement créée par cavitation, dans le sillage d’un projectile non-profilé, tout en conservant sa stabilité. Elle est séparée en trois parties qui sont brièvement résumées dans ce qui suit.

Dans une première partie, nous étudions la modification de trainée induite par l’injection d’air dans le sillage d’une sphère, c’est-à-dire un projectile non-profilé modèle. Pour ce faire, nous avons développé un canal hydraulique à veine verticale dont la vitesse maximale d’écoulement est de 6 m/s. Le projectile étudié est fixé à des capteurs de force et de l’air peut être injecté à débit variable dans son sillage. Dès que cette injection d’air se fait à un débit suffisant, nous observons qu’une grande bulle d’air s’accroche au niveau du plan équatorial de la sphère. Nous démontrons que l’extension spatiale de cette bulle est limitée par la croissance de perturbations à l’interface entre l’air et l’eau. Ainsi, sa longueur est uniquement déterminée par un paramètre adimensionnel reliant la vitesse caractéristique de l’air dans la bulle à celle de l’écoulement de l’eau. La mesure de la trainée de la sphère montre que l’injection d’air n’induit pas nécessairement une réduction de trainée. En effet, dans le régime super-critique, nous montrons qu’une faible injection d’air peut induire une augmentation, jusqu’à un facteur 5, de la trainée de la sphère. Plus généralement, l’injection d’air entraîne la suppression de la crise de trainée.

Dans une deuxième partie, nous évaluons la possibilité de faciliter l’apparition de cette bulle grâce à la cavitation. Ainsi, nous étudions la croissance de bulles de cavitation dans un fluide accéléré. Nous utilisons une tour d’impact afin de générer des accélérations contrôlées et reproductibles sur des réservoirs confinés. Suite à ces accélérations, nous mesurons une dépression dans la zone opposée au point d’impact et nous montrons qu’elle est similaire à une pression hydrostatique où l’accélération maximale du réservoir remplace la constance gravitationnelle. De plus, nous montrons qu’il est nécessaire de relâcher la condition d’incompressibilité du contenant, par exemple en équipant le réservoir d’une paroi flexible, afin d’observer la croissance des bulles de cavitation. Nous démontrons que la taille maximale atteinte par une bulle de cavitation, quantifiant l’énergie qu’elle a emmagasiné, est déterminée par l’accélération maximale et le temps caractéristique de l’impact. Finalement, le dispositif peut être adapté afin de mieux comprendre l’origine des dommages lors d’une commotion cérébrale. Nous démontrons que le potentiel de destruction de bulles de cavitation se développant dans la boîte crânienne que nous prédisons est corrélé aux observations heuristiques faites lors de commotions cérébrales résultant d’un choc frontal.

Enfin, dans une troisième partie, nous nous intéressons à la stabilité de la trajectoire des projectiles résultant de la croissance d'une bulle de gaz dans le sillage d'un objet non-profilé. Nous les modélisons par des projectiles profilés avec une répartition de masse inhomogène. Après l'impact de tels projectiles à la surface d'un bain d'eau, nous observons que leur trajectoire n'est pas nécessairement rectiligne. En effet, en fonction de la vitesse d'impact du projectile et de la position de son centre de gravité, trois types de trajectoire peuvent être observées. L'apparition de trajectoires courbes résulte d'un équilibre entre la force de portance (déstabilisatrice) et la poussée d'Archimède (stabilisatrice). Après avoir caractérisé les projectiles utilisés en soufflerie, nous démontrons que leur trajectoire peut être prédite en résolvant les équations quasi-statiques du mouvement.

Contents

Introduction	1
0.1 Can a bluff body go up to 100 m/s underwater?	3
0.1.1 Evaluation of the required power	3
0.1.2 Origins of the drag	4
0.1.3 Streamlining a projectile	5
0.2 Cavitation onset	7
0.2.1 Pressure distribution around a cylinder	7
0.2.2 Cavitation	8
0.3 Supercavitation	9
0.3.1 Entry in the regime	9
0.3.2 Drag reduction	10
0.4 Statement of the problem and approach	12
I cavitation onset and bubble growth induced by acceleration under free and confined conditions	13
Chapter 1 Short review on cavitation onset and bubble dynamics	15
1.1 Cavitation in accelerated container	16
1.2 Bubble growth	17
1.3 Bubble collapse and cavitation damage	19
1.4 Statement of the problem: Application to brain concussion	21
Chapter 2 Bubble apparition in a confined environment	25
2.1 Pressure drop in the <i>contrecoup</i> region	26
2.1.1 Description of the experimental set-up	26
2.1.2 Pressure drop	27
2.2 Incompressibility and cavitation	28
Chapter 3 Influence of the shock duration on the bubble dynamic	31
3.1 Methods	32
3.1.1 Shock duration	32
3.1.2 Radius of the cavitation bubble	33
3.1.3 Numerical methods	33
3.2 Bubble dynamics	36
3.2.1 Rayleigh-Plesset equation	36
3.2.2 Maximum radius of a bubble	36
3.2.3 Low acceleration regime	37
3.2.4 High acceleration regime	37
3.3 Damaging potential	39
3.4 Futur developments	40
3.4.1 Bubble interaction	41
3.4.2 In-vivo Measurements	42
II Characterisation of a supercavitating sphere near the drag crisis	45
Chapter 4 Short review on ventilated cavities	47

4.1	Generalities on ventilated cavities	48
4.2	Ventilated cavities in the wake of projectiles	49
4.2.1	Dimensional analysis	49
4.2.2	Length of the cavity and shedding process	49
4.2.3	Influence of the blockage ratio	51
4.2.4	Drag reduction: application to spheres	51
4.3	Statement of the problem	53
Chapter 5	Experimental set-up	55
5.1	Hydraulic tunnel construction	56
5.2	Flow in the empty test-section	56
5.3	Drag measurements	57
5.3.1	Validation of the measurement set-up	57
5.3.2	Drag coefficient of a sphere	58
Chapter 6	In-crisis drag modification	61
6.1	Morphology of the bubbles	62
6.2	Bubble length	63
6.2.1	Bubble length measurements	63
6.2.2	Surface instability properties	65
6.3	In-crisis force measurements	67
6.3.1	Drag of a sphere with air injection at its back	69
6.3.2	Drag modification	69
6.3.3	Application to supercavitation	70
III	Stability of the trajectory of the streamlined projectile	73
Chapter 7	Short review on water entry and path instabilities	75
7.1	Water entry	76
7.1.1	Cavity formation	76
7.1.2	Slender bodies	77
7.2	Path instabilities	78
7.3	Statement of the problem	79
7.4	Experimental details	79
7.4.1	Trajectory reconstruction	79
7.4.2	Projectiles	80
7.4.3	Releasing method	80
Chapter 8	Path instabilities of streamlined bodies	83
8.1	Experimental Results	84
8.1.1	Nature of the trajectory	84
8.1.2	Quasi-planar trajectories	86
8.2	Equations of motion and closing parameters	87
8.2.1	Presentation of the model	87
8.2.2	Lift and Drag	88
8.2.3	Position of the aerodynamic center	89
8.2.4	Dissipative torque	90
8.3	Results and discussion	91
8.3.1	Solution of the equation of motion	91
8.3.2	Critical velocity and growth time	92
8.3.3	Quantitative comparison and dive depth	94

8.4	Controlling the instability	96
	Conclusion	99
	Appendices	105
	Appendix A List of publication	107
	Appendix B International Physicists' Tournament	109
	Bibliography	119

INTRODUCTION

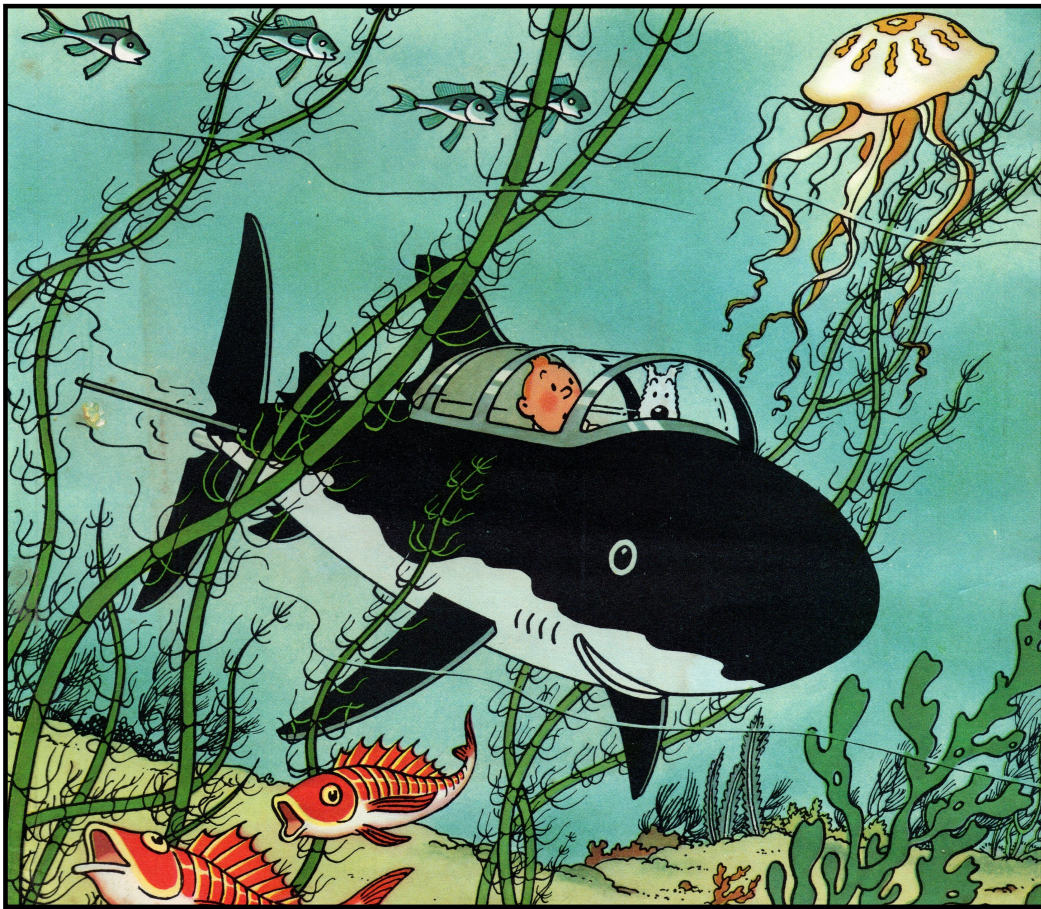


Figure 1: Drawing of the front page of *Red Rackham's Treasure*, by Hergé 1944.

The publication of *Red Rackham's Treasure* in 1944 followed the early development of submarines in the navy, such that, at this time, the invention of Professor Cuthbert Calculus was still uncanny to most of the readers. Since then, even though submarines have completely changed (size, shape, propulsion technique...), their maximum speed is still below 100 m/s. Which leaves the following question open: Can a bluff body go up to 100 m/s underwater?

0.1 Can a bluff body go up to 100 m/s underwater?

0.1.1 Evaluation of the required power

When a body travels underwater at a velocity U , it experiences a drag force D resisting to its motion. This force is generally expressed as follows [1]:

$$D = \frac{1}{2} \rho S C_D U^2 \quad (1)$$

where ρ denotes the density of water, S the cross-stream surface of the body and C_D the drag coefficient. The drag coefficient depends on both the geometry of the object considered and the Reynolds number $Re = UL/\nu$, which compares the inertial effects to the viscous effects in the flow [1]. In this expression, L is the characteristic size of the body and ν the kinematic viscosity of the fluid.

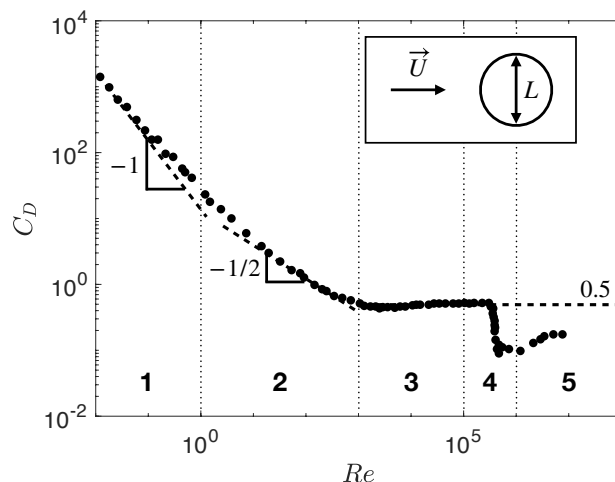


Figure 2: Experimental measurements of the drag coefficient C_D of a sphere of diameter L as a function of the Reynolds number $Re = UL/\nu$. In this expression, U is the flow velocity and ν the kinematic viscosity of the fluid. Five characteristic regimes are identified in this curve. Figure reproduced from [1].

The evolution of the drag coefficient with the Reynolds number is plotted, for a sphere, in figure 2. The curve can be separated in five characteristic regimes. In the first regime, below $Re \approx 1$, drag is dominated by viscous effects and we have $C_D \propto Re^{-1}$. Between $Re \approx 1$ and $Re \approx 10^3$, *i.e.* in the second regime, drag is dominated by the viscous effects in the boundary layer and we have $C_D \propto Re^{-1/2}$. Between $Re \approx 10^3$ and $Re \approx 10^5$ and the drag is dominated by inertial effects, C_D is constant and has a value around 0.5. This regime (3) bounds sub-critical domain. Indeed, around $Re \approx 3 \times 10^5$, the drag coefficient drops to 0.1: this is called the drag crisis and is identified in figure 2 as the fourth characteristic regime. After that, the drag slowly increases up to ~ 0.2 at $Re = 10^7$: this is the beginning of the supercritical domain (5).

Going back to our initial question, Professor Calculus' submarine is metric (*i.e.* $L \sim 1$ m) and going at 100 m/s, the corresponding Reynolds number of the water flow around it $Re \sim 10^8$. In this regime, for a bluff body, $C_D \sim 1$, and the power P necessary to reach this velocity is:

$$P = DU = \frac{1}{2} \rho S C_D U^3 \sim 10^9 \text{ W} \quad (2)$$

This power is on the order of the one produced by a nuclear power plant (the expected power of the "EPR Flamanville" is 1.7 GW) and, today, it appears ridiculous to think that we could design a submarine with such propulsion power. However, this would technically become feasible if we managed to reduce the power necessary, and hence, the drag coefficient of the submarine, by a factor 100.

0.1.2 Origins of the drag

Let us remind that the drag of a projectile travelling underwater at high Reynolds number, far from the free surface, has two components, namely the skin friction and the pressure drag. Both components rely on the viscous properties of the the fluid as an inviscid flow at constant velocity does not generate any drag.

Skin friction originates from the friction between the fluid and the surface of the object: in other words, through viscous effects and the non-slip condition, the fluid entrains the

object. As a consequence, the skin friction mainly depends on the flow in the boundary layers, *i.e.* the regions near the surface of the object, where viscosity dominates. Locally, the contribution of the skin friction to a unit surface δS is $\delta D_F = \eta \delta S \frac{\partial u}{\partial y}$, where u is the tangential component of flow velocity, $\partial u / \partial y$ its gradient normal to the surface and η the dynamical viscosity of the fluid. From this expression, we deduce that this component of the drag depends on the total wetted area of the projectile.

Pressure drag arises from the pressure difference between the upstream and downstream faces of the projectile. As a consequence, it is strongly correlated to the streamwise asymmetry of the flow: for instance to the development of structures in the wake of the projectile. This component of the drag depends on the frontal area of the projectile.

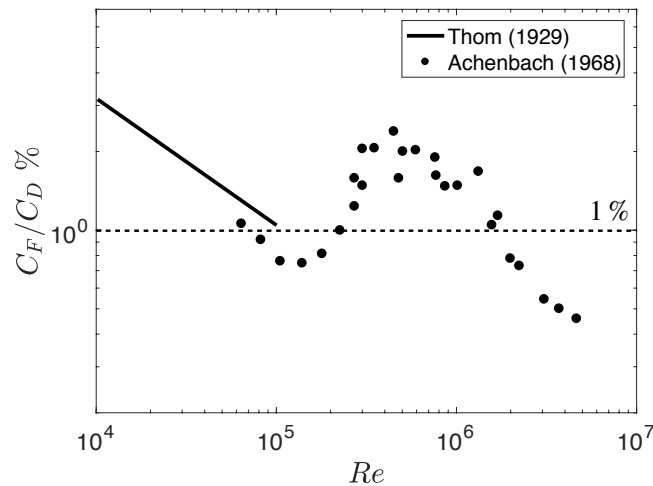


Figure 3: Contribution of the skin friction to the total drag (C_F/C_D) as a function of the Reynolds number. Figure reproduced from [2]. Dot are experimental data corrected to account for the finite width of the tunnel. Solid line is a semi-theoretical prediction in the sub-critical regime drawn from [3].

The relative contribution of the skin friction and the pressure drag to the drag coefficient are respectively written C_F and C_P , such that $C_D = C_F + C_P$. Due to the physical phenomena at play, the relative contribution of the two drags depends on the Reynolds number of the flow. At low Reynolds numbers ($Re < 1$), the flow is dominated by viscous effects and the pressure drag is negligible $C_D \sim C_F$. For Reynolds numbers between 10^4 and 10^7 the contribution of the skin friction to the total drag C_F/C_D is plotted in figure 3, reproduced from [2]. We observe that, in that range of Reynolds number, the skin friction typically represent 1 % of the total drag. More precisely, the contribution of the skin drag is slightly decreasing: it passes from 3 % at $Re \sim 10^4$ to ~ 0.3 % at $Re \sim 5 \times 10^6$.

This suggests that in the regime of interest ($Re > 10^5$), skin friction is negligible and the efforts to reduce the drag should be focused on the pressure drag.

0.1.3 Streamlining a projectile

A technique to reduce the pressure drag consists in using fairing around a bluff body to make it streamlined. This effect is particularly used in mechanical sports (Formula 1, Moto GP) or bicycle: The effect of fairings is striking when comparing the velocity record of recumbent bike. On the one hand, without fairing, the maximum velocity is around 74 km/h, outdoor on a flat 200 m section. The recumbent bike used for this record is similar to the one used by Aurélien Bonneteau to break the indoor hour record in 2012 (56.7 km)

shown in figure 4(a). On the other hand, on a fully faired bike, shown in figure 4(b), Todd Reichert reached 144.2 km/h over an outdoor section of 200 m. Assuming that the power

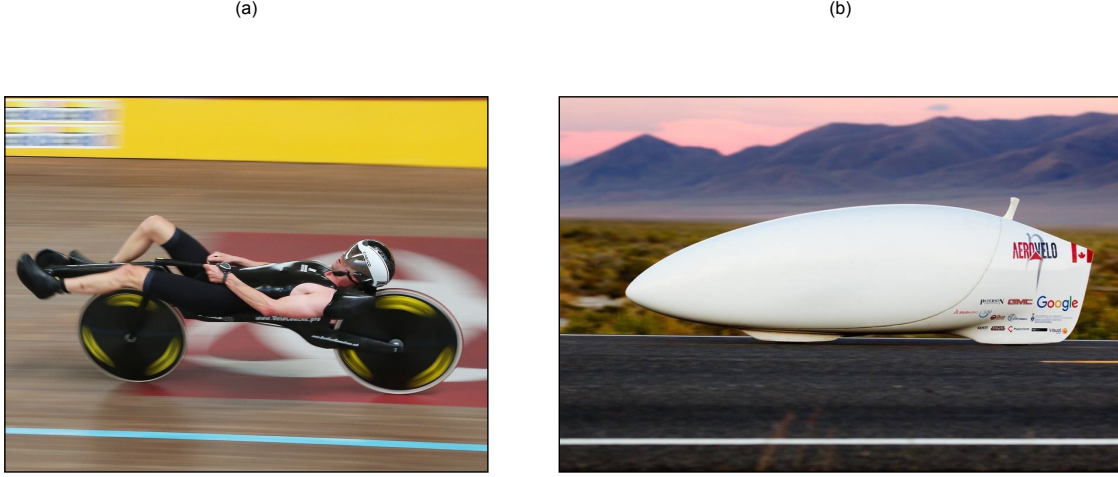


Figure 4: (a) Picture of Aurélien Bonneteau for his attempt to beat the hour record on track in 2012. He managed to bike 56.7 km in an hour. The peak record for a 200 m section on a similar bike is 74 km/h. (b) Picture of the fully faired bike used to break the record of velocity on a 200 m section in 2016. The velocity reached was 144.2 km/h on a slightly downhill section (-0.6% slope).

generated by the two cyclists is equivalent, we compute the drag coefficient gain of adding fairings using equation (2):

$$\frac{(SC_D)_{streamlined}}{SC_D} = \left(\frac{U_{streamlined}}{U} \right)^3 \approx 13.5\% \quad (3)$$

Although it does not completely suppress the pressure drag (this would correspond to $\frac{(SC_D)_{streamlined}}{SC_D} \sim 3\%$), adding fairing on a bluff body generate a important drag reduction. The gain on the drag coefficient is greater as the frontal surface of the bike has been slightly increased by the presence of fairing. The history of fairing in human powered vehicles is thoroughly discussed in [4].

The gain on the drag coefficient can be precisely evaluated from wind tunnel measurements. Figure 5 presents the drag coefficient of a streamlined body of revolution in the range of Reynolds number between 10^4 to 10^8 . In this range, the drag coefficient is mostly decreasing: it passes from 0.3 at $Re = 10^4$ to 0.03 at $Re = 10^8$. The minimum value of the drag coefficient (0.02) is reached in the drag crisis, for $Re \sim 2 \times 10^6$. This corresponds to a drag coefficient of $\sim 10\%$ when compared to the one of a sphere.

Both observations suggest that streamlining a projectile leads to drag reduction up to a factor 10. In this thesis, we investigate cavitation as a way of streamlining a projectile travelling underwater.

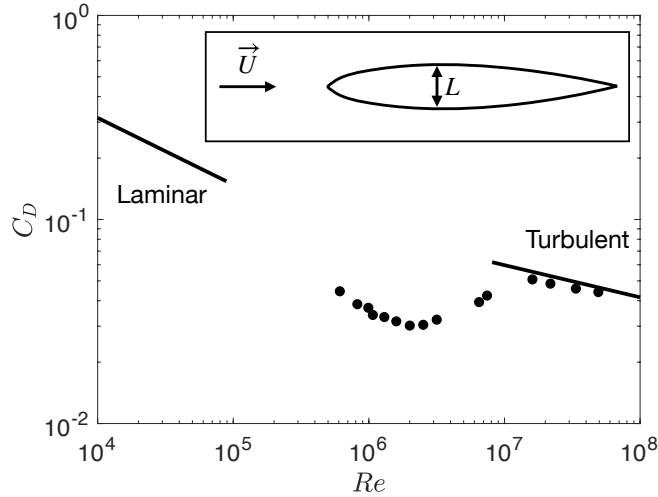


Figure 5: Drag coefficient C_D of a streamlined body of revolution as a function of the Reynolds number $Re = UL/\nu$. Figure reproduced from [1]. Solid lines indicate the trends for sub and super critical regimes. Dots are experimental data. The profile of the projectile used is the one of the R101 airship and is sketched in the inset. Drag coefficient is based on frontal area.

0.2 Cavitation onset

0.2.1 Pressure distribution around a cylinder

When a projectile travels underwater, the pressure distribution in the fluid is modified. At high Reynolds number, the pressure field around a two-dimensional projectile can easily be evaluated assuming that the flow is potential.

Let us consider a cylinder of radius R in a cross flow of velocity \vec{U} , far from the projectile. This situation is sketched in figure 6(a). For a potential flow, writing $\vec{u}(r, \theta)$ the streamwise velocity and $\vec{v}(r, \theta)$ the cross-stream velocity, we have:

$$\begin{cases} u(r, \theta) = U \left(1 - \cos(2\theta) \left(\frac{R}{r} \right)^2 \right) \\ v(r, \theta) = -U \sin(2\theta) \left(\frac{R}{r} \right)^2 \end{cases} \quad (4)$$

Using Bernoulli, we express the pressure at the boundary of the cylinder:

$$p_s = p_\infty + \frac{1}{2} \rho U^2 (1 - 4 \sin^2 \theta) \quad (5)$$

This relation is plotted in figure 6(b) and compared with measurements taken from [2] for Reynolds numbers ranging from 10^5 to 3.6×10^6 . Potential theory matches well the experimental data up to $\Phi = 50^\circ$. Beyond this value, for all Reynolds the pressure is found to reach a plateau, such that $C_p = (p_s - p_\infty)/(\frac{1}{2} \rho U^2)$ lies between -1.25 and -0.4. The discrepancies between potential theory and experiments comes from the fact that the boundary layer is neglected, in particular the flow separation it induces and the wake it creates.

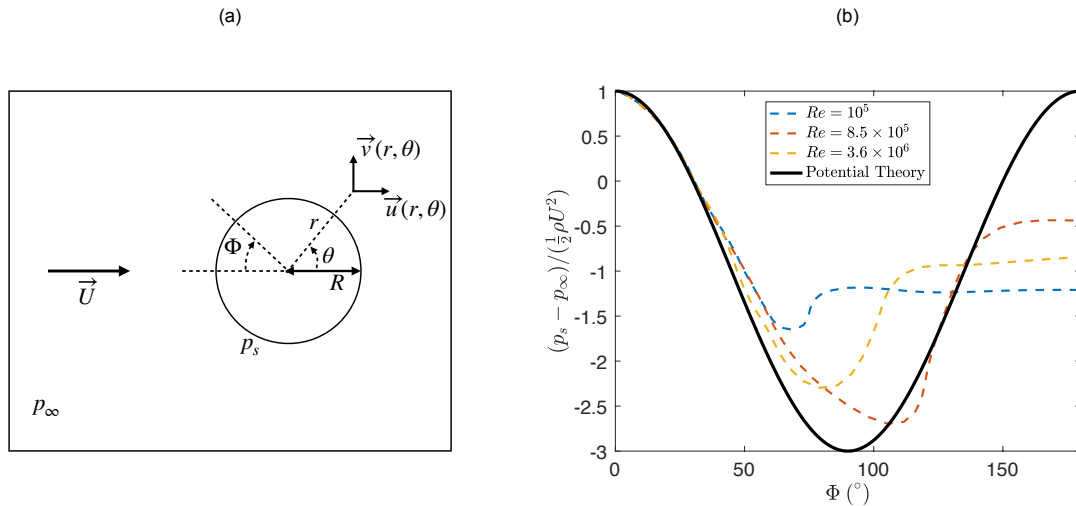


Figure 6: (a) Sketch of a cylinder in a cross-flow of velocity U . The pressure far from the cylinder is p_∞ . The cylinder has a radius R and as a pressure p_s at its surface. The streamwise velocity of the fluid is $\vec{u}(r, \theta)$ and the cross-stream velocity is written $\vec{v}(r, \theta)$. (b) Pressure coefficient $C_p = (p_s - p_\infty) / (\frac{1}{2} \rho U^2)$ as a function of the position on the cylinder surface Φ , where $U^2 = u^2 + v^2$. Potential theory (equation (5)) is drawn in solid black line. Experimental data are taken from [2] and plotted in dashed line. Reynolds number is varied between 10^5 and 3.6×10^6 .

In all the cases, we observe that both experimentally and theoretically, we expect a pressure drop around the projectile. The physics of which lies in the fact that the space occupied by the object reduces the path of the fluid: in the incompressible limit, this constraint induces an increase of velocity and thus a decrease of the pressure. The magnitude of this pressure drop grows with the velocity of the flow. Theoretically, the minimum pressure is reached at the equatorial plane of the cylinder and has a value:

$$p_s^{min} = p_\infty - \frac{3}{2} \rho U^2 \quad (6)$$

0.2.2 Cavitation

We deduce from equation (6) that it exists a velocity U_{cav} for which the pressure reaches the vapor pressure of water. The vapor pressure $P_{vap}(T)$ is defined as the pressure at which the water is in equilibrium with its own vapor for a fixed temperature T [5]. The phase diagram of water is sketched in figure 7(a). We note that the vapor pressure of water grows with T . At $T = 25^\circ\text{C}$, the vapor pressure of water is 2.3×10^3 Pa. At atmospheric pressure ($P = 1013$ hPa), the vapor pressure is reached at $T = 100^\circ\text{C}$.

Excepting metastable cases, when $P = P_{vap}$, a phase transition is observed. The transition from liquid to gas at constant pressure (increasing T), is easily observed in cooking pot and is called ebullition. Conversely, the transition from liquid to gas at constant temperature (decreasing P), is less common and referred as cavitation.

For water flowing around a cylinder, this transition is expected for:

$$p_\infty - \frac{3}{2} \rho U_{cav}^2 = P_{vap} \Rightarrow U_{cav} = \sqrt{\frac{2}{3} \frac{p_\infty - P_{vap}}{\rho}} \approx 8.1 \text{ m/s} \quad (7)$$

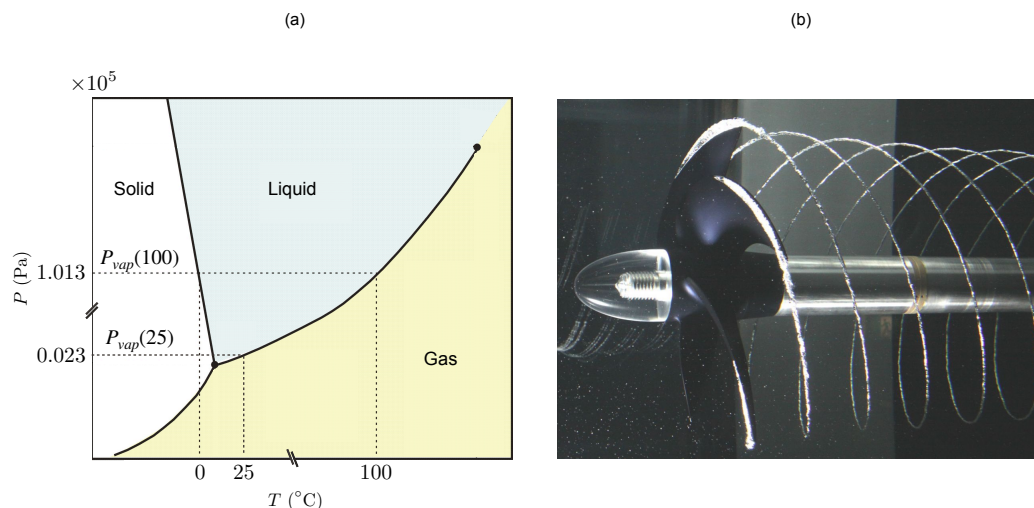


Figure 7: (a) Phase diagram of water as a function of its temperature T and its pressure P . The vapor pressure of water is written P_{vap} . (b) Picture of the cavitation trail observed behind a ship propeller at the Cavitation Research Laboratory of the Australian Maritime College (<http://www.amc.edu.au/facilities/cavitation>).

Cavitation is thus expected roughly above 10 m/s. This velocity is typically reached at the tip of the blades of ship propellers where it is known that cavitation is observed as illustrated by the picture of figure 7(b), taken from the Cavitation Research Laboratory of the Australian Maritime College website. In this picture, we observe that bubbles are created on the low pressure side of the boat propeller blades. An helicoidal wake of bubbles is then created by the advection of bubbles in the wake of the blades.

According to the results obtained for a cylinder in a potential flow (equation (5)), the dimensionless parameter that governs the pressure at the boundary of an object travelling underwater, and hence the creation of vapor bubbles in a flow [6, 7], called the cavitation number σ , writes:

$$\sigma = \frac{p_{\infty} - P_{vap}}{\frac{1}{2}\rho U^2} \quad (8)$$

0.3 Supercavitation

0.3.1 Entry in the regime

From the definition of the cavitation number (8), we expect cavitation bubble to nucleate in a flow wherever $\sigma \sim 1$. For a two dimensional wedge, the influence of the cavitation number on the phase transition is shown in figure 8 adapted from [8]. For $\sigma = 1.4$, we indeed observe a trail of bubbles created in the near wake of the cavitator. These bubbles then display a characteristic wake pattern.

As the cavitation number is decreased, the bubbles invade a larger region of the wake of the wedge. For σ below 1.23, a large bubble starts pinning at the rim of the wedge. The characteristic streamwise size of this bubble grows when σ is reduced. Above $\sigma = 0.78$ the interface of the bubble is largely turbulent and unstationnary. However, for $\sigma = 0.69$ the instabilities at the interface of the large bubble have almost disappeared. This regime, in which a large cavitation bubble is pinned on the cavitator is called supercavitation.

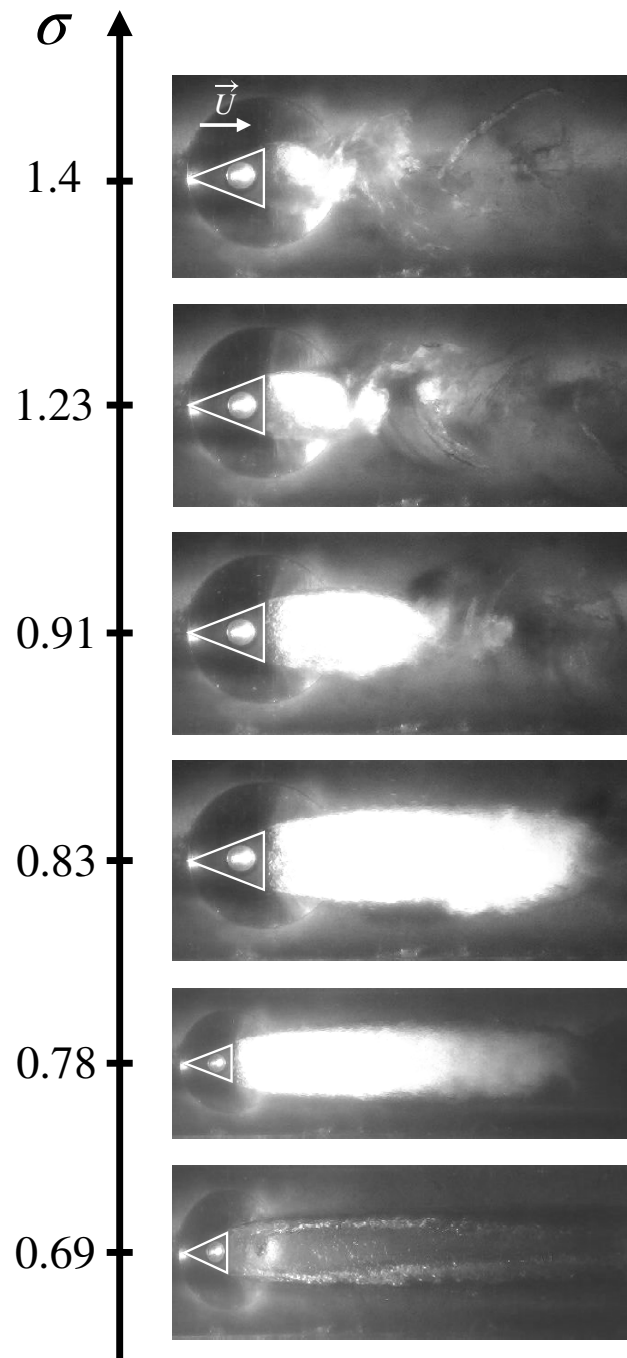


Figure 8: Picture of a 45° angle wedge and its wake in a cavitation tunnel for various cavitation numbers. Figure adapted from [8]. Cavitation number is $\sigma = (p_\infty - P_{vap})/1/2\rho U^2$, where p_∞ is the pressure far from the projectile, P_{vap} the vapor pressure of water, ρ its density and U the velocity of the flow. The base of the cavitator is 2 cm. The shutter speed is below $1/50000$ s.

0.3.2 Drag reduction

One major advantage of this cavitation regime is that the wake of the projectile is modified. At high Reynolds number, for a bluff body, the main component of the drag arises from the pressure difference between the upstream and downstream surfaces of the projectile. This pressure difference as well as the structures in the wake come from the symmetry breaking

due to the boundary layer separation [1].

Since the cavitation bubble tends to "streamline" the solid that moves through water, the main consequence of the modification of the wake of the projectile in the supercavitation regime is a reduction of its drag. Numerous studies have focused on the determination of the drag reduction via the computation of the stationary shape of the bubble. All those studies are thoroughly reviewed in [6, 7]. However, it is interesting to note that all theoretical studies assume a potential flow, a constant pressure in the gas and they neglect evaporation. The closure condition of the cavity is widely discussed and the different models includes: releasing the free-surface dynamical conditions at a fixed point (open wake model) [9], the use of an "image object" onto which the cavity closes (Riabouchinsky model) [10], having a jet flowing back into the cavity (re-entrant jet model) [11].

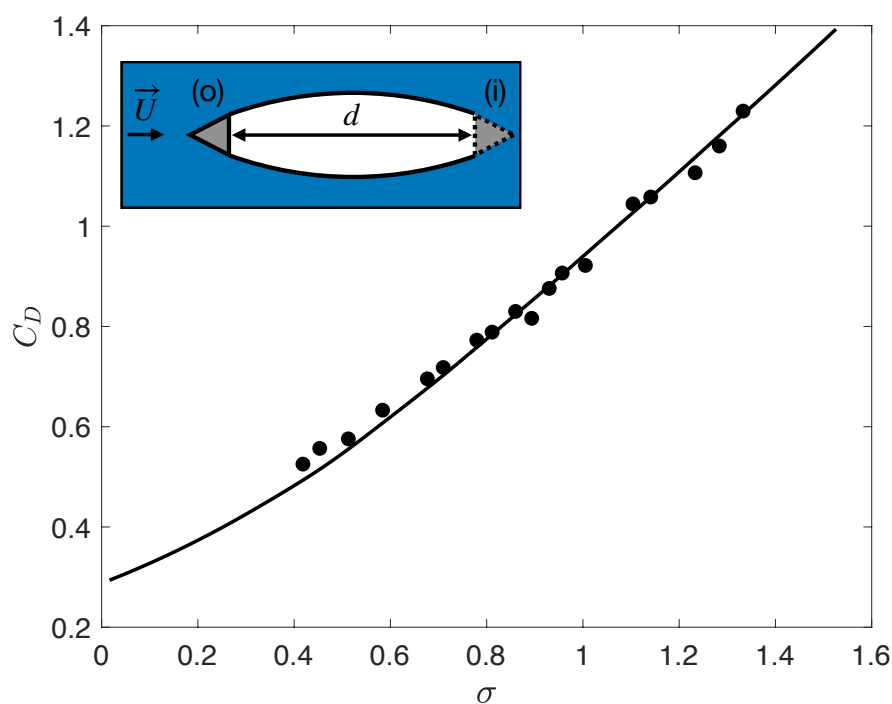


Figure 9: Drag coefficient of a 30° wedge as a function of the cavitation number σ . Figure adapted from [12]. Experimental data are corrected to account for the finite width of the test section. Solid line is the Riabouchinsky model [10]. Inset: sketched of the Riabouchinsky model. The closing of the cavity is imposed on a image (i) of the wedge placed at a distance d downstream the object (o).

Figure 9 shows the drag of a 30° wedge as a function of the cavitation number σ and compare it with the Riabouchinsky model. In this model, the distance d between the downstream image (i) onto the cavity closes and the object (o) is a free parameter which grows with σ as sketched in the inset. The rest of the figure is adapted from [12]. We observe that the drag coefficient is reduced when σ is decreased: it passes from ~ 1.2 for $\sigma = 1.4$ to ~ 0.5 for $\sigma = 0.4$. In other words, drag is reduced by the elongation of the cavitation bubble. C_D tends to 0.3 when the cavitation number goes to 0. Riabouchinsky model describes well the experimental data, which are corrected to account for the finite width of the test-section.

0.4 Statement of the problem and approach

This thesis is dedicated to the experimental and theoretical study of cavitation and supercavitation. It is decomposed in three different parts:

- In Part I, we focus on the cavitation onset and the early growth of a cavitation bubble. To that end, cavitation is triggered by an hydrostatic-like pressure drop following the acceleration of a closed container. We will study both the influence of the confinement on the vapor production and the dependence of the bubble dynamic on the time evolution of the acceleration. This unsteady induction of cavitation can be used to facilitate the entry in the supercavitation regime, model the early stages of the launch of torpedoes or missiles or to better understand the implication of cavitation in brain concussion. This last application is the main point of interest of Part I.
- In Part II, we present the experimental set-up developed to determine the hydrodynamic properties of a supercavitating sphere. We create a system analogous to supercavitation by replacing the phase transition of water by a controlled air injection in the wake of the sphere. We concentrate on the influence of the bubble on the drag crisis of the sphere.
- In Part III, we consider that a supercavitating is analogous to a streamlined projectile with inhomogeneous mass distribution. We focus on determining the condition under which, such projectiles, follow straight trajectories following their impact on water. This work can be apply to predict the trajectory stability of projectile such has missiles or torpedoes as well as to understand the way birds like gannet dive.

PART I

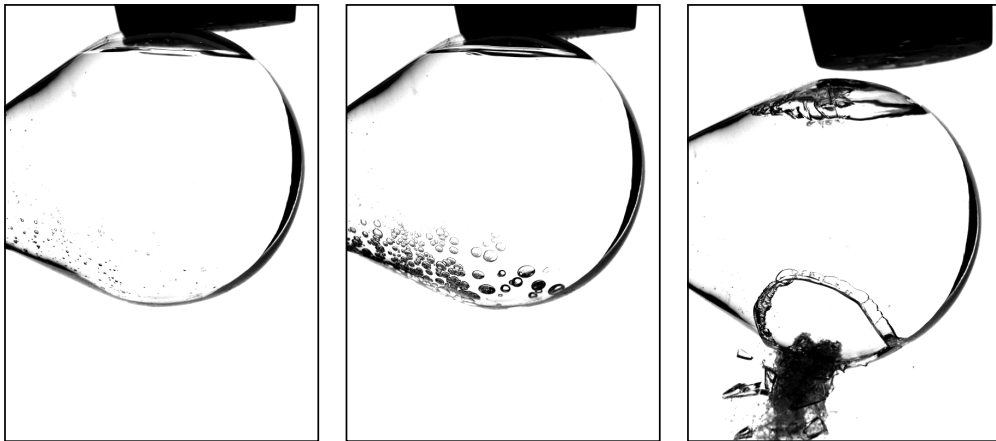
CAVITATION ONSET AND BUBBLE GROWTH INDUCED BY ACCELERATION UNDER FREE AND CONFINED CONDITIONS



Decreasing the pressure of a liquid below its vapor pressure can trigger a phase transition through the nucleation of gas bubbles. This phenomenon is called cavitation. We wish to characterise the early stage of the growth of cavitation bubbles developing near a projectile travelling underwater. However, in such a system, the velocities required to reach a pressure drop high enough to observe cavitation are challenging to obtain in a simple experimental set-up. In this part, we study the dynamic of a bubble growing in a low pressure region of a fluid created through the acceleration of its container. In a first chapter, we quickly review the state of the art of cavitation in accelerated container. We then present our experimental set-up and show how the confinement of cavitation bubble change their threshold of apparition. Finally, the third chapter focus on the study on bubble dynamics in accelerated container. Through this part, we show that this framework allows us to investigate whether cavitation can be the cause of the damages observed in the brain following a shock on the head, the so-called brain concussion.

1

SHORT REVIEW ON CAVITATION ONSET AND BUBBLE DYNAMICS



Fluid container accelerated when hit by a hammer: Cavitation bubbles grow in the region opposite of the point of impact and shatter the reservoir.

Contents

1.1	Cavitation in accelerated container	16
1.2	Bubble growth	17
1.3	Bubble collapse and cavitation damage	19
1.4	Statement of the problem: Application to brain concussion .	21

1.1 Cavitation in accelerated container

A simple method to accelerate a container filled with fluid is to impact it with, for example, a mallet. This situation is sketched in figure 1.1(a), taken from [13]: a reservoir partially filled with a height h of fluid initially at rest at atmospheric pressure p_r is hit by a hammer. The corresponding maximum acceleration a of the container can easily reach 900 g. Intuitively, we can predict that the shock will induce a pressure modification in the container: as the reservoir is impacted, it instantaneously moves downward while water, due to inertia, will only move after a delay, resulting in a reduction of the pressure in the region opposite of impact.

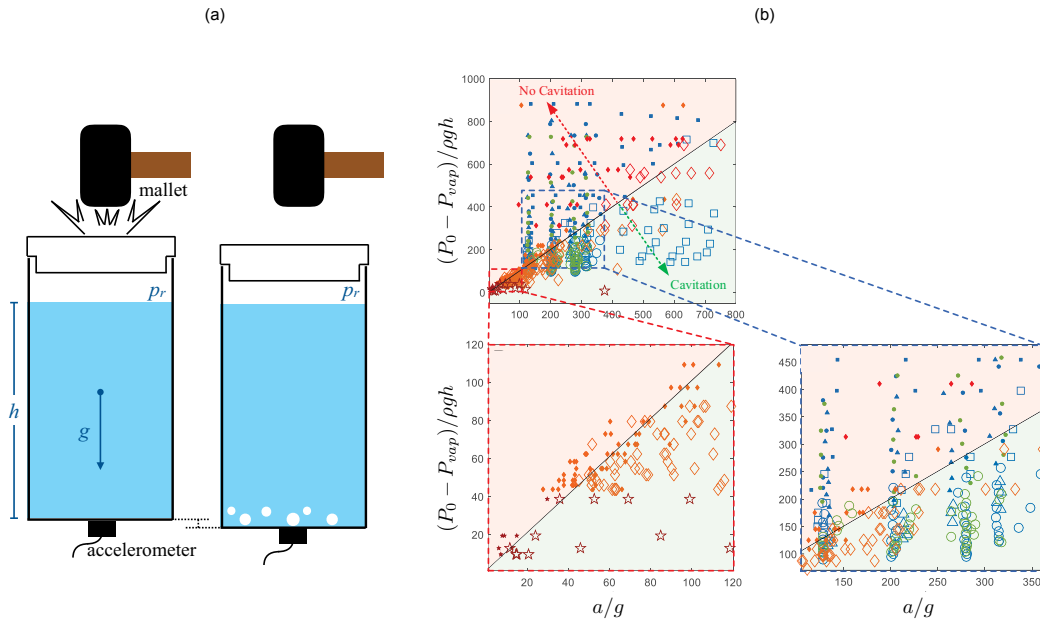


Figure 1.1: (a) Sketch of a simple set-up used to study cavitation in accelerated containers taken from [13]. A reservoir partially filled with a height h of fluid initially at rest at atmospheric pressure p_r is vertically hit by a hammer. The acceleration of the container is measured with an accelerometer located at the bottom of the reservoir. The experiment is filmed with a fast-camera to check for the potential apparition of cavitation bubbles. (b) Outcome of the experiment described in (a) in the diagram $(a/g, (p_r - P_{vap})/\rho gh)$ adapted from [13]. g denotes the gravitational constant, P_{vap} the vapor pressure of the fluid and ρ its density. The solid black line represents the curve for which the cavitation number Ca is equal to 1, where $Ca = (p_r - P_{vap})/\rho ah$. Open symbols are tries for which cavitation events have been recorded and conversely for filled symbols. Shape and color of the symbols are for different fluids (water, silicon oil, ethanol) and size of containers. Height of the fluid is varied from 1 to 200 mm.

However, the cavitation number σ , previously introduced, cannot account for this inertial pressure drop and hence, cannot be the relevant dimensionless number in this problem. To that end, a new cavitation number Ca was introduced by Pan & *al.* [13]:

$$Ca = \frac{p_r - P_{vap}}{\rho ah} \quad (1.1)$$

where P_{vap} is the vapor pressure of the fluid and ρ its density. This formula suggests that the pressure drop necessary for cavitation bubble to grow $(p_r - P_{vap})$ is an hydrostatic-like pressure (ρah) where gravity g has been replaced by the characteristic acceleration a

of the shock. The experiment described before can then be performed while measuring the acceleration a and filming the container to check for cavitation bubbles. The figure 1.1(b), reproduced from [13], displays the results in the diagram $(a/g, (p_r - P_{vap})/\rho gh)$. The dimensionless acceleration of the shock a/g is extensively varied from 20 to 800 (changing the intensity of the hit) and the parameter $(p_r - P_{vap})/\rho gh$ is varied from ~ 10 to 1000 (changing the fluid and its height h). Over the whole range of parameters, most of the experiments in which cavitation events have been recorded (open symbols) lies below the curve Ca and reciprocally for tries where no cavitation bubbles were detected (filled symbols).

This cavitation number and the experimental results suggest that the pressure drop in an accelerated column of fluid scales as ρah . However, this does not tell us how this relation is modified when the container does not have a free surface and is fully filled. Additionally, the study of the dynamic of the cavitation bubble in such a set-up is left open. These questions are the main interests of our work, and before addressing them, let us briefly review the literature on bubble dynamic.

1.2 Bubble growth

To study the dynamic of the cavitation bubble, let us consider the situation sketched in figure 1.2(a): a spherical gas bubble of radius R is immersed in a fluid of varying pressure $P(t)$, far from the bubble. In this section, we derive the Rayleigh-Plesset equation which governs the dynamic of R . For greater details, the reader is referred to the original derivation by Rayleigh [14] and Plesset [15] or to the enlightened explanations gathered in [16, 7, 6].

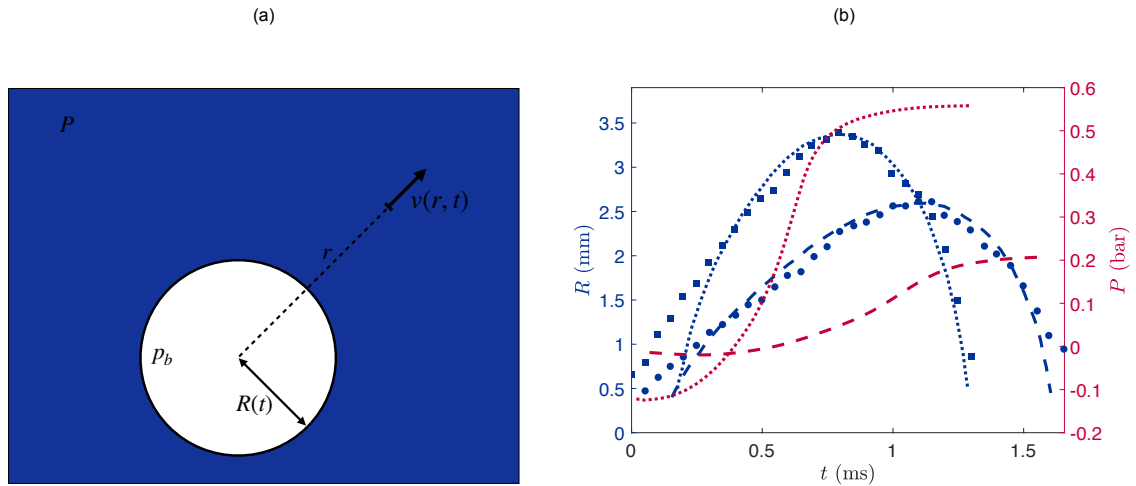


Figure 1.2: (a) Schematic of a spherical bubble in a spherically symmetric environment. The bubble has a radius $R(t)$ and an inner pressure p_b . The particle of fluid at distance r from the center of the bubble has a purely radial velocity $v(r, t)$. The pressure of the fluid far from the bubble is P . (b) Time evolution of the radius R of two bubbles as they go through a varying pressure field P . Figure reproduced from [15]. Blue lines correspond to the theoretical evolution of R computed with equation (1.9) for the experimentally measured pressure evolution drawn in red line. The corresponding experimental measurements are displayed in blue squares and dots.

For a flow with spherical symmetry, the incompressibility of the fluid imposes $\text{div}(\vec{v}) = 0$

which yields, assuming that there is no mass transport through the bubble interface:

$$v = \frac{R^2 \dot{R}}{r^2} \quad (1.2)$$

The fluid flow is governed by the Navier-Stokes equation which, when projected along the radial direction, reads as follows:

$$\rho \frac{\partial v}{\partial t} + \rho v \frac{\partial v}{\partial r} = -\frac{\partial p}{\partial r} + \eta \left(\frac{1}{r} \frac{\partial^2 (rv)}{\partial r^2} - \frac{2v}{r^2} \right) \quad (1.3)$$

Where η denotes the dynamic viscosity of the outer fluid and $p(r, t)$ its pressure at a distance r from the center of the bubble. Substituting v with its expression (1.2), we find that the viscous term is strictly null and we obtain:

$$\rho \frac{R^2 \ddot{R} + 2R\dot{R}^2}{r^2} - \rho \frac{2R^4 \dot{R}^2}{r^5} = -\frac{\partial p}{\partial r} \quad (1.4)$$

Integrating between $r = R(t)$ and $r = \infty$ where $p(\infty) = P(t)$ we obtain:

$$\rho \frac{R^2 \ddot{R} + 2R\dot{R}^2}{r} - \rho \frac{R^4 \dot{R}^2}{2r^4} = p(R) - P(t) \quad (1.5)$$

The pressure in the outer fluid at the interface of the bubble $p(R)$ can further be evaluated through the continuity of the radial stress across the bubble interface:

$$p(R) = p_b - \frac{4\eta \dot{R}}{R} - \frac{2\gamma}{R} \quad (1.6)$$

where $p_b(R)$ is the pressure of the gaz inside the bubble and γ the surface tension between the liquid and the gas. Substituting this expression in equation (1.5) yields the Rayleigh-Plesset equation:

$$R\ddot{R} + \frac{3}{2}\dot{R}^2 + \frac{4\nu\dot{R}}{R} + \frac{2\gamma}{\rho R} = \frac{p_b - P_\infty}{\rho} \quad (1.7)$$

$p_b(R)$ can itself be expressed assuming that the gas transformation in the bubble is isothermal and that the bubble is initially at rest with the surrounding liquid of pressure P_0 :

$$p_b(R) = \left(P_0 + \frac{2\gamma}{R_0} \right) \left(\frac{R_0}{R} \right)^3 \quad (1.8)$$

with R_0 being the initial radius of the bubble and P_{vap} the vapor pressure of water. Injecting this relation in the Rayleigh-Plesset equation gives:

$$R\ddot{R} + \frac{3}{2}\dot{R}^2 + \frac{4\nu\dot{R}}{R} + \frac{2\gamma}{\rho R} = \frac{P_{vap} + \left(P_0 + \frac{2\gamma}{R_0} \right) \left(\frac{R_0}{R} \right)^3 - P(t)}{\rho} \quad (1.9)$$

This equation was first confronted to experimental data by Plesset in 1949 [15]. The cavitation bubble was created in a cavitation tunnel and then travelled through a spatially varying pressure field, resulting in a time evolution of its radius. This evolution could be followed using a fast-camera. Figure 1.2(b), reproduces two of the time evolution of the radius of the bubble from [15]. This suggests that as the pressure difference is negative, the bubble grows. When the outer pressure exceeds the inner pressure, the bubble keeps growing with inertia, but then rapidly collapses.

1.3 Bubble collapse and cavitation damage

Cavitation has been thoroughly studied for boat propeller applications. Indeed, a propeller or the rotor of a hydraulic pump is composed of streamlined blades with a concave and a convex side. When rotating towards the concave side, the blades produce a pressure difference between their two sides. In particular, a low pressure zone will appear on the convex side, called the suction side. As shown before, when the rotor velocity is high enough, the pressure on the suction side can go below the vapor pressure of water, and hence, trigger the nucleation of cavitation bubble. This phenomenon has been shown to have two consequences on the propeller operation. First, it reduces its efficiency and changes the optimal shape of a propeller [17]. Second, it erodes the blades and dramatically shortens its life expectancy [18, 19, 20].

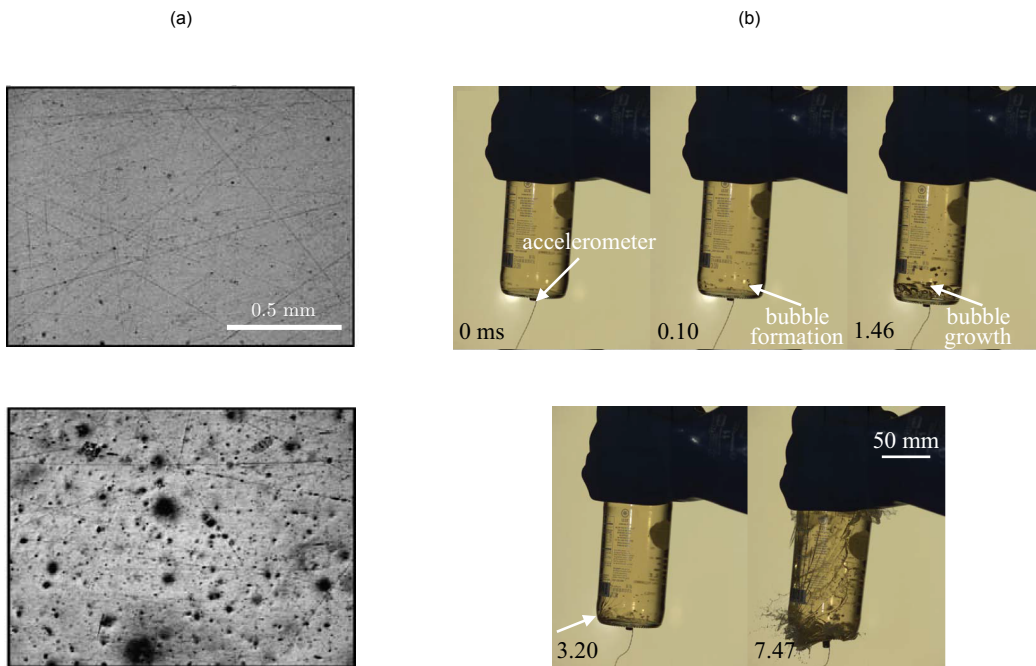


Figure 1.3: (a) Pictures of a copper plate composing the suction side of an hydrofoil taken from [21]. Top panel: before being exposed to cavitation. Bottom panel: after one hour of exposition to cavitation in a cavitation tunnel. 4.98 % of the surface is damaged. (b) Chronophotography of a glass bottle partially filled with water and impacted with a mallet at $t = 0$. Bubbles appear 0.1 ms after the shock in the region opposite to impact (*contrecoup* location) and grow until reaching their maximum radius at $t \approx 1.46$ ms, after which they rapidly collapse. At $t = 3.2$ ms, all the bubbles have disappeared and the glass is fractured in the *contrecoup* region, while it surprisingly remains intact at the impact point. Later, the entire bottle is shattered.

The damaging potential of cavitation is shown in the two pictures presented in figure 1.3(a), taken from [21]. The suction side of a hydrofoil (*i.e.* the side potentially exposed to cavitation) is made of an initially undamaged copper plate (upper panel). The hydrofoil is then placed in a cavitation tunnel of maximal velocity 20 m/s for one hour, such that cavitation bubbles form on the suction side. The bottom picture of figure 1.3(a) shows the suction side after being exposed to cavitation: nearly 5 % of the surface is damaged by pits.

As noted in [13], cavitation bubbles are also damaging when growing in accelerated containers. This phenomenon is illustrated in the chronophotography reproduced from [13] in figure

1.3(b) where the effect of the impact of a hammer on a glass reservoir partially filled with water is followed. Time origin is fixed at impact, and cavitation bubbles quickly appear in the *contrecoup* area (at $t \approx 0.1$ ms), that is, the region with size comparable to that of the hammer and located opposite to it. Bubbles then grow and reach their maximum size (a few millimeters) at $t \approx 1.46$ ms, after which they collapse in less than 2 ms, which fractures the glass at $t \approx 3.2$ ms. Remarkably, the glass is fractured at the point of collapse of cavitation bubbles while it remains intact at the point of impact of the hammer, suggesting that the collapse of cavitation bubbles is responsible for the damages. At later times, the whole container is shattered.

The collapse of a cavitation bubble has been identified as the cause of a local increase of the pressure on a solid boundary nearby. This was illustrated in [22] and is reproduced in figure 1.4(a), where the collapse of a cavitation bubble on a photoelastic material is recorded. After the disparition of the bubble ($t = 0$), fringes pattern develop around the point of collapse in the material, which suggests that a large variation of pressure has been triggered. 10 microseconds after the end of the collapse, the fringes cover an area of diameter roughly one centimeter. The magnitude of this large pressure variation is quantitatively measured in the same study [22] and reproduced in figure 1.4(b): at the point on the surface nearest to the bubble collapse, the pressure is found to increase up to ~ 21 Mpa. The total duration of the pressure increase is $\sim 10 \mu\text{s}$.

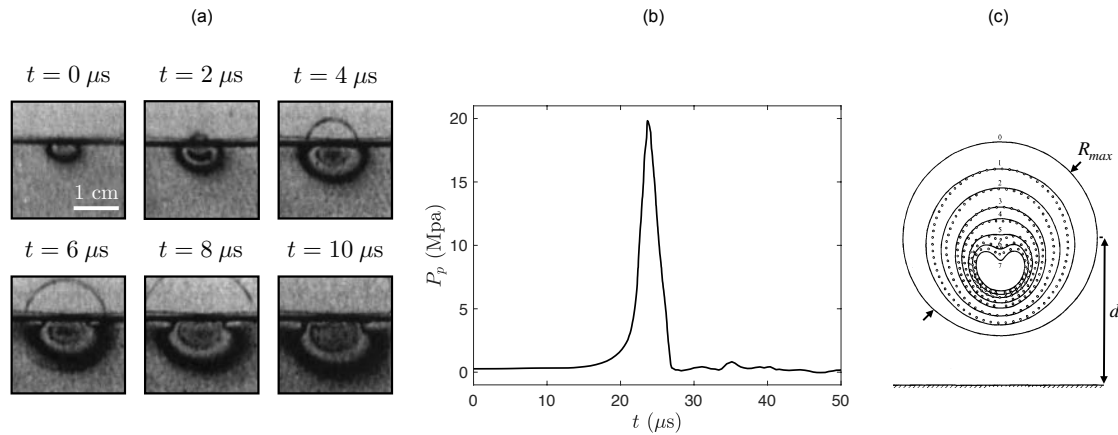


Figure 1.4: (a) Collapse of a cavitation bubble near a photoelastic material reproduced from [22]. The bubble collapse ends at $t = 0$. The bubble maximum radius is $R_{max} = 3.5$ mm and it is initially located 0.21 mm away from the solid boundary. Fringes are observed in the photoelastic material and a shock wave can be observed in the fluid using Schlieren imaging. (b) Time evolution of the pressure at the wall P_p after the collapse of a bubble of maximum radius $R_{max} = 3.5$ mm and located a distance $d = 1$ mm of the boundary. The figure is reproduced from [22]. (c) Comparison of the experimental shape of a bubble collapsing near a solid boundary. Figure adapted from [23]. Solid line is the theoretical prediction from [24]. Time step is $3.3 \mu\text{s}$. The bubble has a maximum radius $R_{max} = 2.6$ mm and is initially located at a distance $d = 3.9$ mm from the surface.

The local increase of the pressure on the boundary is the cause of the deterioration of the surface. Two main mechanisms are at play during the collapse of a cavitation bubble in the creation of this pressure increase: the emission of a shock wave [25, 26] and the creation of a fast moving jet [27, 28]. However, their relative contribution to the damages is still debated [22, 29].

The shock wave can be observed using Schlieren imaging: it starts propagating at the collapse and is observed $4 \mu\text{s}$ after it in 1.4(a). At a distance r from the bubble, the peak

pressure of the shock wave P_p was shown to scale as [30, 6]:

$$P_p \approx 100P_\infty \frac{R_{max}}{r} \quad (1.10)$$

where R_{max} denotes the maximum radius of the bubble.

When a cavitation bubble collapses near a solid boundary, a jet is created. The jet is found to be directed towards the boundary. The formation of the jet can be intuitively understood assuming potential flow: a collapsing bubble behaves as a sink and its mirror image with respect to the wall needs to be considered to respect the impermeability boundary condition. As a consequence, the bubble collapses in a pressure gradient perpendicular to the wall which results in the deformation of its interface and the creation of the re-entrant jet. The early development of the jet was observed experimentally in [23] and compared with theoretical prediction from [24]. The results, from [23] are presented in figure 1.4(c). The bubble, before the collapse, has a maximum radius $R_{max} = 2.6$ mm and is located at a distance $d = 3.9$ mm from the boundary. Roughly $16 \mu s$ after the beginning of the collapse, the interface at the point opposite to the solid boundary starts to curve in, resulting in the creation of the jet. At later times, beyond the scope of the theoretical study presented here, the jet is found to impact the boundary at a velocity up to 200 m/s. This impact could be the cause of the local increase of the pressure in the material.

1.4 Statement of the problem: Application to brain concussion

The study of cavitation in an accelerated and confined environment is relevant for defenses applications: the launch of missiles and torpedoes from submarines or the acceleration phases of propellers. Additionally, the damages caused by the collapse of cavitation bubbles are often listed as a possible cause of the brain concussion following a violent impact on the head. In such applications, avoiding or at least reducing the damages induced by the collapse of cavitation bubbles is crucial.

The application of cavitation to the understanding of mild Traumatic Brain Injuries (mTBI) particularly caught our attention: the experiment of a mallet impacting a fluid container sketched in figure 1.1(a) seems to be a direct model of a shock on the head. Indeed, the container represents the cranial vault while brain tissues and physiological fluids are modelled by the water (they have a relative density close to 1 and are mainly composed of water).

So far, mTBI are known to be a common consequence of linear shocks on the head, in motorized vehicle accidents or sports [31, 32]. Their detection and prevention is a major medical concern not only because they can be lethal, but also because they are often involved in the early development of neuronal diseases [33, 34, 35]. One of these disease is the Chronic Traumatic Encephalopathy (CTE), which results from repetitive brain trauma [36], and was diagnosed on an important rate of U.S. football players. Figure 1.5(a), taken from [36], presents coronal sections of a normal brain (top) and of a brain displaying a CTE (bottom): the pathological brain shows dilatation of the ventricles, atrophy and shrinkage of cerebral structures.

The severity of the damages following a linear impacts on the head are commonly classified by the so-called Wayne State University (WSTC) curve [37, 38]. Characterizing shocks by their peak acceleration a and timespan τ , the WSTC, drawn in figure 1.5(b), has a

hyperbolic-like behavior that draws a frontier between innocuous and acute shocks. The curve was empirically constructed on post-mortem and animal experiments, and data lying above it imply a probability of brain concussion greater than 50 %, which shows that linear shocks become lethal when having strong acceleration or long duration. As seen in figure 1.5(b), the WSTC curve also captures observations in American football (squares and dots), where colors (red or green) indicate the occurrence of brain concussion or not. A more precise analysis reveals that the curve is not hyperbolic, as seen for instance for typical shocks in football where the acceleration threshold of damage decreases from ~ 100 g for $\tau \approx 5$ ms to ~ 70 g for $\tau \approx 15$ ms, denoting g as the acceleration of gravity. For shorter shocks, the WSTC also predicts that the critical acceleration of damage dramatically increases, rising to a value as high as ~ 400 g for $\tau \approx 1$ ms. The WSTC is the starting point for the derivation of most severity indexes for linear shocks. Above the threshold, lesions in the brain tissues are usually found in the so-called contrecoup area, opposite to impact [39].

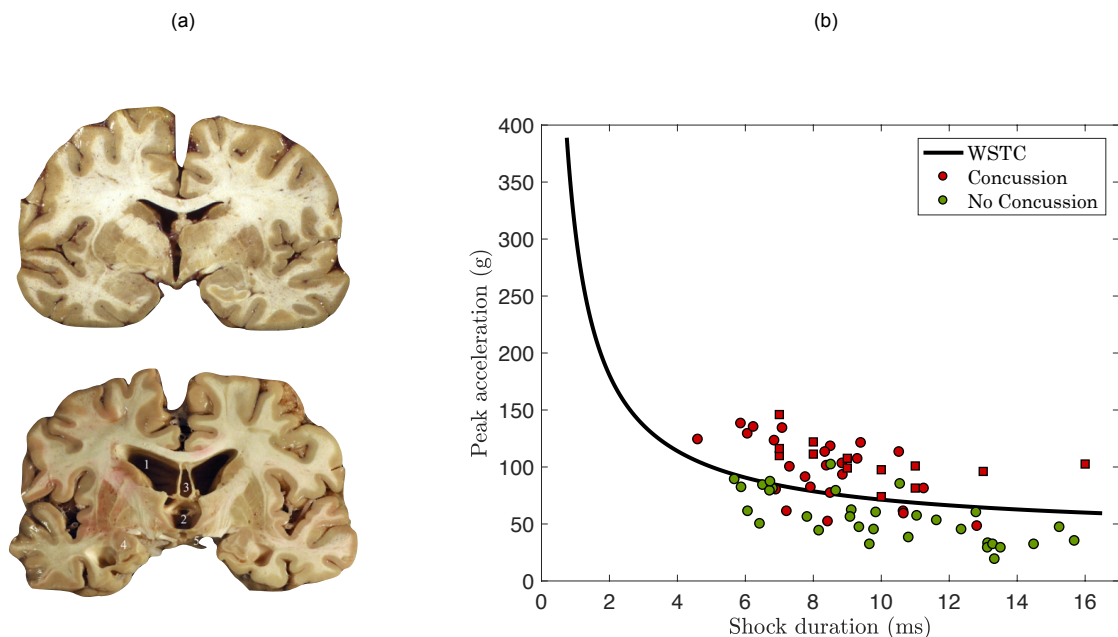


Figure 1.5: (a) Comparison of coronal sections of brains: a normal one (top) and another showing Chronic Traumatic Encephalopathy (CTE). Figure 1.5(a) taken from [36]. The pathological brain presents severe dilatation of ventricles II (1) and III (2), cavum septum pellucidum (3), marked atrophy of the medial temporal lobe structures (4), and shrinkage of the mammillary bodies (5). (b) The Wayne State University Tolerance Curve [37] (WSTC, solid line) empirically quantifies the head tolerance towards shocks with peak acceleration and characteristic duration. For a shock above the curve, the probability of brain concussion is larger than 50%. Data are recorded for shocks on football players (dots: Pellman 2003 [40]; squares: Broglio 2010 [41]) where the characteristic time of the shock was computed from the Severity Index (SI). The color indicates if concussion (red) is observed, or not (green).

However, there is no widely accepted damaging mechanism: traumas might arise from the local increase of shear stress in brain tissues, from large variation of intracranial pressure [42, 43] or from the collapse of cavitation bubbles [44, 45, 46]. As a consequence, WSTC remains heuristic and fails to capture all the experimental observation.

In the rest of this part, we focus on studying the possibility of cavitation being a cause of mTBI. To that end, we propose to make the simple experimental set-up sketched in figure 1.1(a) closer to the real cranial vault by using a completely filled container. This is expected

to change the onset of cavitation as the pressure at the bottom of the tank was determined by both the acceleration of the shock and the ambient air pressure in the container.

As for defense applications, evaluating the damaging potential of the cavitation bubbles is also crucial. To that end, equation (1.10) suggests that the maximum radius of a cavitation bubble is a good proxy for assessing its damaging potential. To determine its maximum radius, we wish to study the dynamic of the growth of a cavitation bubble in an accelerated fluid container. In particular, we would like to determine if it is governed by Rayleigh-Plesset equation.

Finally, the heuristic observations gathered in the WSTC state that the severity of the damages following a shock is uniquely determined by both its maximum acceleration and its characteristic timespan. This raises two questions regarding a scenario of mTBI based on cavitation: Does the damaging potential of a cavitation bubble in an accelerated container depends on these two parameters? If so, can it be analytically evaluated?

In chapter 2, we present an experimental set-up, analogous to the cranial vault, which allows us to monitor the growth of the confined cavitation bubbles and measures both the pressure and the acceleration of the container.

In chapter 3, we focus on determining the damaging potential of a cavitation bubble in such an experimental set-up. To that end, we study, both experimentally and theoretically the dynamic of the cavitation bubbles.



2

BUBBLE APPARITION IN A CONFINED ENVIRONMENT

The large majority of the work presented in the two following chapters was realized in collaboration with Juliette Amauger, at that time, intern in the group. This work would not have been nearly as good without her implication and determination to overcome the (numerous) difficulties.

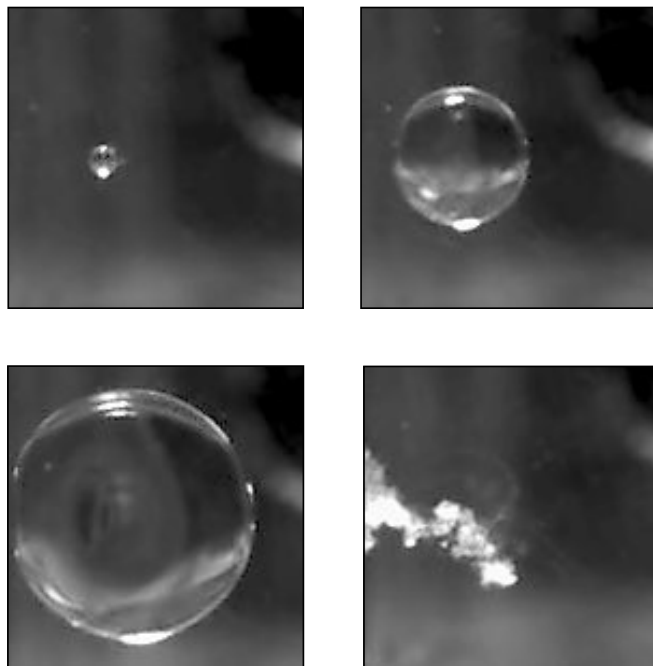


Illustration of the growth and the collapse of a bubble recorded using the experimental set-up described in this chapter.

Contents

2.1	Pressure drop in the <i>contrecoup</i> region	26
2.2	Incompressibility and cavitation	28

2.1 Pressure drop in the *contrecoup* region

2.1.1 Description of the experimental set-up

The set-up we use to study the growth of confined cavitation bubbles during a shock is sketched in figure 2.1. Cavitation occurs in a water container, made of transparent acrylic, which has a square base of side 5 cm and a length L . This reservoir, drawn in the left panel of figure 2.1, is hermetically sealed with a membrane located at its bottom. The bending stiffness K of the membrane can be tuned from 1 to 10^9 N/m. In this chapter, flexible membrane will refer to a membrane with $K \approx 1$ N/m while rigid will refer to a membrane with $K \approx 10^9$ N/m.

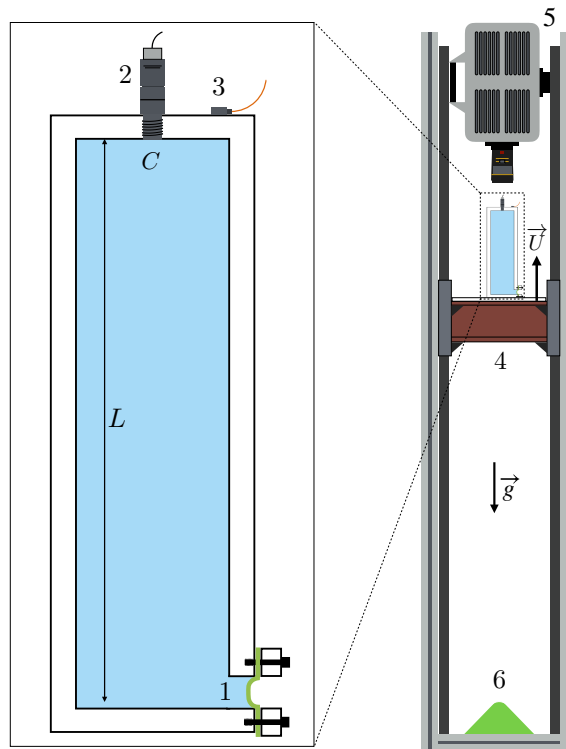


Figure 2.1: Set-up for the study of cavitation bubble growth generated by an acceleration under a controlled confinement. Left panel: fluid container. An acrylic reservoir (length $L = 16.5$ cm and square section of side 5 cm) equipped with a flexible membrane (1) at its bottom is filled with degassed water. At point C (the *contrecoup* area, opposite to impact), pressure and acceleration are measured with a capacitive transducer (2) and with a piezoelectric accelerometer (3). Right panel: impact device. The reservoir is fixed on the falling stage (4) of a three-meters drop tower and experiments are recorded from the top with a high-speed video camera (5). The characteristics of the impact on the ground are tuned with a damper (6) that fixes both the shock acceleration and duration. The vertical velocity of the falling stage, positive when directed upward, is written \vec{U} .

The container is clamped on the falling stage of a three-meters high drop tower sketched in the right panel of figure 2.1. The falling stage is then impacted at a vertical velocity \vec{U} on a damper, resulting in the application of a vertical acceleration \vec{U} on the reservoir. The height of the fall as well as the damper characteristics can be adjusted to modify the properties of the shock (shape of the acceleration signal, maximum acceleration...). The region C, opposite to the point of impact, the so-called *contrecoup* area, is video recorded either from

the side or from above using a fixed fast-camera filming up to 20,000 frames per second. Additionally the pressure P in this region and the acceleration \dot{U} of the tank during a shock are measured using a pressure transducer and an accelerometer. Both sensors sample at a frequency of 10 kHz. The dynamic of a bubble initially nucleating in the *contrecoup* area is followed and correlated to the pressure and acceleration measurements.

2.1.2 Pressure drop

During a shock, the pressure $P(t)$ in the *contrecoup* region is $P(t) = P_0 - \delta P(t)$, where P_0 denotes the static pressure and $\delta P(t)$ the dynamic pressure which varies during a shock. For a container equipped with a flexible membrane ($K \approx 1$ N/m), synchronous measurements of the acceleration \dot{U} of the container and of the dynamic pressure $\delta P(t)$ during a shock are shown in figure 2.2(a). For a shock of maximum acceleration $a \approx 60$ g and time duration of ~ 7 ms, the hydrostatic-like pressure $\rho\dot{U}L$, where ρ and L respectively denotes the density of the fluid and the length of the container, and the dynamic pressure $\delta P(t)$ are synchronized and have the same trend. They rise up from 0 at the beginning of the shock ($t = 0$) to ~ 1 bar at $t \approx 7$ ms before going back to zero at $t \approx 13$ ms. In this situation, the total pressure $P = P_0 - \delta P(t)$ in the *contrecoup* area is decreasing during a shock corroborating the fact that bubbles growing in this region are a result of cavitation. Additionally, this suggests that, when the container is equipped with a flexible membrane, the dynamic pressure in the *contrecoup* region is linked to the acceleration of the container by the relation $\delta P \sim \rho\dot{U}L$. To check these observations on a larger scale, we define δP_m the maximum of the dynamic pressure $\delta P(t)$ during a shock.

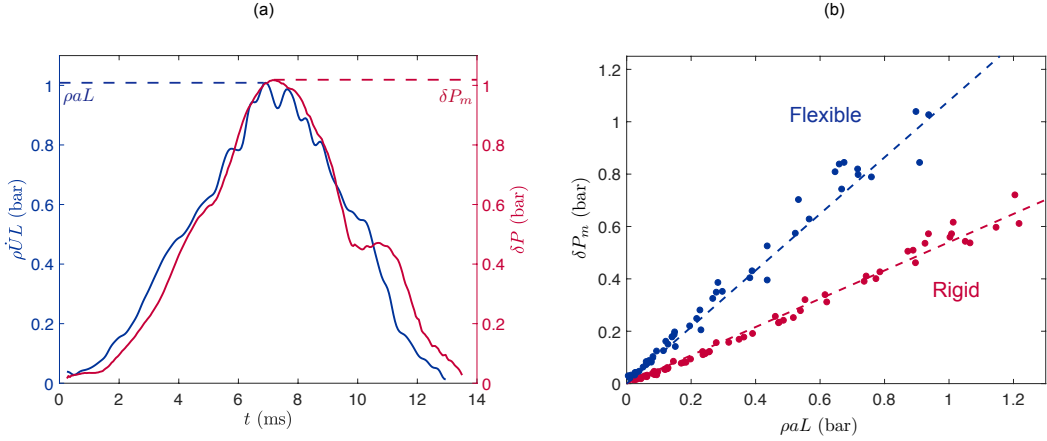


Figure 2.2: (a) Temporal evolution of the hydrostatic-like pressure $\rho\dot{U}L$ (blue) and dynamic pressure $\delta P(t)$ (red) in the area opposite of the point of impact during a shock of maximum acceleration $a \approx 60$ g and timespan $\tau \approx 7$ ms. Dynamic pressure is defined as $\delta P(t) = P_0 - P(t)$ when P_0 is the static pressure and $P(t)$ the total pressure in the *contrecoup* area. The maximum dynamic pressure is denoted δP_m and the maximum acceleration a . (b) Dynamic pressure δP_m as a function of the hydrostatic-like pressure $\rho a L$ for different flexibility of the membrane. Blue data is for a flexible membrane of bending stiffness $K \approx 1$ N/m. Red data is for a rigid membrane of bending stiffness $K \approx 10^9$ N/m. Blue dashed lined is the potential model $\delta P_m = \rho a L$ for the flexible membrane. The red dashed lined is the potential model $\delta P_m = \frac{1}{2} \rho a L$ for the rigid membrane case. Both models are plotted with no fitting parameters.

We plot δP_m as a function of the hydrostatic-like pressure $\rho a L$ for different flexibilities of the membrane in figure 2.2(b). For all membranes, δP_m has an increasing linear trend with

ρaL . This confirms that, no matter what are the properties of the container used, there is always a pressure drop in the *contrecoup* region. For a flexible membrane ($K \approx 1$ N/m, blue data), we recover the previous relation $\delta P_m = 1.03\rho aL \pm 0.08\rho aL$ for the maximum value of the pressure drop. However, when using a rigid membrane ($K \approx 10^9$ N/m, red data), we find $\delta P_m = 0.49\rho aL \pm 0.05\rho aL$.

These behaviours can be recovered theoretically in the following way: as the characteristic velocity of the reservoir filled with water when it impacts the damper is 1 – 3 m/s, the Reynolds number of the flow in the reservoir is greater than 10^5 which allow us to assume the flow to be potential. Writing U the velocity of the reservoir, aligned with the vertical axis z directed upward, the only solution for the potential Φ is $\Phi(z, t) = U(t)z$ and the unstationary Bernoulli equation writes:

$$\rho z \frac{dU}{dt} + \frac{1}{2}\rho U^2 + P + \rho g z = \text{constant} \quad (2.1)$$

The pressure at the bottom of the tank is $P_B(t) = P_B^{stat} - \delta P_B(t)$ and at the top $P(t) = P_0 - \delta P(t)$. For the rigid membrane case, the problem is fully anti-symmetric with respect to the middle of the reservoir. Hence, $\delta P_B(t) = -\delta P(t)$. Using Bernoulli equation between the top and bottom points yields $\delta P(t) = \frac{1}{2}\rho \dot{U}L$. This relation is plotted in red dashed line in figure 2.2(b) and describes well the data for the container equipped with a rigid membrane. For the flexible membrane regime, a pressure is initially imposed near the membrane. Hence, expressing Bernoulli equation between the extremities of the reservoir, we get $\delta P(t) = \rho \dot{U}L$. It is plotted in blue dashed line in figure 2.2(b) and is in good agreement with the data for the flexible membrane regime.

As a consequence, the apparition of cavitation bubbles in a confined environment depends on the properties of the container. For a flexible container, we recover that the pressure in the *contrecoup* reaches the vapor pressure of water P_{vap} for $Ca = \frac{P_0 - P_{vap}}{\rho aL} = 1$ as previously observed in [13]. However, using a rigid container will result in a delayed apparition of cavitation bubbles: the vapor pressure of water is reached in the *contrecoup* region for cavitation number as low as $1/2$. In other words, using a rigid reservoir inhibits the nucleation of cavitation bubbles.

Additionally, it is interesting to note that, in either situation, the pressure variation in the tank alone cannot be the cause of traumatic brain injuries reported in American football or boxing: head accelerations rarely overcome 150 g [47, 48] and the pressure drop below 600 g in the *contrecoup* region is negligible compared to the typical yield stress of tissues [49]. Hence, an energy focusing mechanism needs to be involved in the brain damaging process.

2.2 Incompressibility and cavitation

For a shock of maximal acceleration $a \approx 150$ g, the maximal pressure drop is $\delta P_m \sim 2.5$ bar in the flexible membrane case and $\delta P_m \sim 1.3$ bar in the rigid membrane case. The minimum absolute pressure in the *contrecoup* region $P_m = P_0 - \delta P_m$ is far below the vapor pressure of water ($P_{vap} \approx 1.3 \times 10^{-2}$ bar) in both cases, *i.e.* the cavitation number is far below $1/2$. As a consequence, we expect cavitation bubbles to nucleate in this region in both situations. To check for their growth, we observe the container from the side during a shock of maximum acceleration $a \approx 150$ g and time duration of ~ 7 ms. Figure 2.3 presents the two chronophotographies obtained for different rigidities of the membrane used.

For a flexible membrane ($K \approx 1$ N/m), we observe that, during the shock, the initially bubbles present on the wall grow until they reach their maximum size around $t = 9.6$ ms.

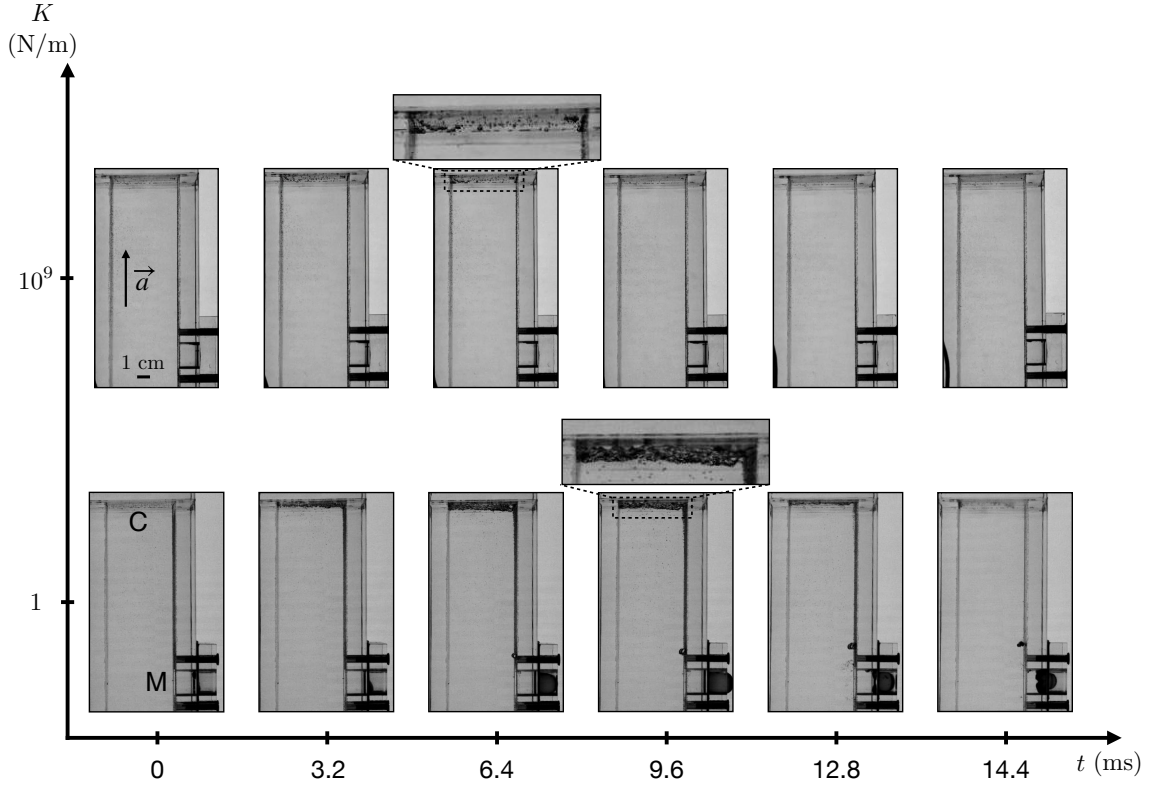


Figure 2.3: Chronophotographies of the impact of the reservoir on a damper for different values of the bending stiffness K of the membrane. The shock results in a vertical maximal acceleration $a \approx 150$ g applied on the container for a time ~ 7 ms. The contrecoup region C is located at the point opposite of impact.

At this point, they cover the whole *contrecoup* region and have a thickness close to ~ 0.5 cm. After the end of the shock, they rapidly collapse and have completely disappeared at $t = 14.4$ ms. However, for a rigid membrane ($K \approx 10^9$ N/m), the sub-millimetric bubbles initially present in the *contrecoup* area barely grow to reach a sub-millimetric maximum size around $t = 6.4$ ms. At this time, they sparsely cover the *contrecoup* area. At $t = 9.6$ ms, they already have recovered their initial size.

This simple experiment draws our attention on an important property of the container: its deformability. Indeed, when a rigid membrane is used for seal our reservoir, it can be considered as incompressible and no gas bubble can grow in such a system. However, when we use a flexible membrane, it deforms in a way that modifies the volume of the container. This is observed in the chronophotography for $K \approx 1$ N/m in figure 2.3: initially flat, the membrane deforms outward when the bubbles start to grow in the *contrecoup* region. As a consequence, having a container equipped with a flexible membrane has two consequences: first, following a shock, the pressure drop measured in the *contrecoup* area (*i.e.* region opposite of impact) is more important than when the container is completely rigid. Second, as the incompressibility condition is released, bubbles have space to nucleate and grow.

These observations do not rule out the possibility of cavitation bubbles to grow in the cranial vault. Indeed, it must itself be seen as a container with a variable volume, as known from the measurements of the variations ΔV of the intracranial volume (typically a few milliliters) accompanying the change ΔP of the intracranial pressure (typically a few millimeters of mercury) during a heart cycle [50, 51, 52]. Additionally, we adjusted the bending stiffness of the membrane used in our experimental set-up to comply with the known *in-vivo* relation $\Delta P(\Delta V)$ reported in figure 2.4. The value of the bending stiffness K of the equivalent

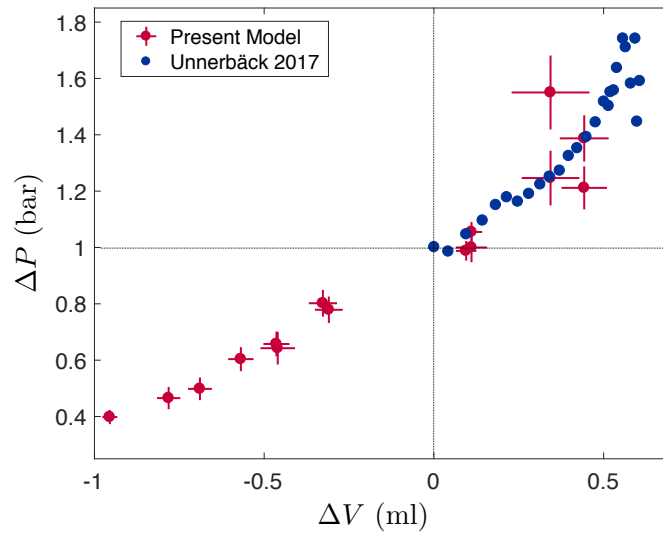
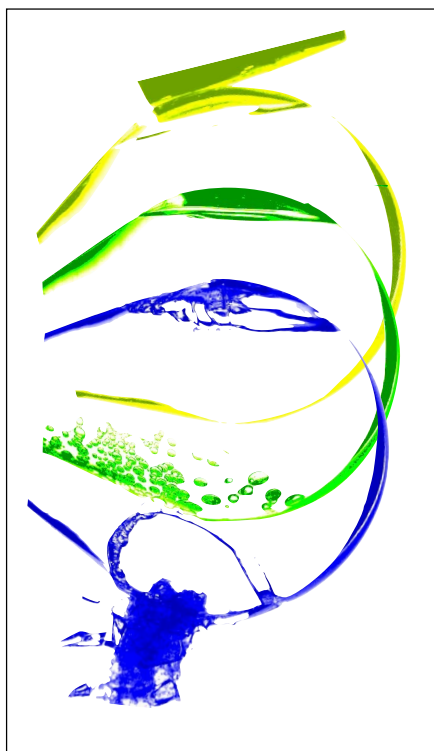


Figure 2.4: Relationship between the pressure and volume variations ΔP and ΔV , for a human head (blue data) and for our model system (red data). Both series of data overlap if we use a soft flexible membrane of bending stiffness 1 N/m. Human data are taken from Unnerbäck 2017 where peak values have been discarded. Pressure in our set-up are measured for a membrane of thickness 3.5 mm and then extrapolated for the equivalent membrane of thickness 1 mm.

membrane corresponds to the previously introduced flexible case (*i.e.* $K \approx 1$ N/m), which validates the possibility of cavitation bubbles growing in the head. For the rest of the chapter, we will focus on a container equipped with a flexible membrane.

3

INFLUENCE OF THE SHOCK DURATION ON THE BUBBLE DYNAMIC



Chronophotography of the shattering of a rounded bottom flask induced by the collapse of cavitation bubbles in the region opposite to the point of impact. Yellow is for $t = 0$ (i.e. impact of the hammer), green is for $t = 1.2$ ms and blue for $t = 6.65$ ms.

Contents

3.1	Methods	32
3.2	Bubble dynamics	36
3.3	Damaging potential	39
3.4	Futur developments	40

3.1 Methods

3.1.1 Shock duration

The set-up presented in the previous chapter allows us to measure the acceleration \dot{U} of the container during a shock. The typical time evolution of \dot{U} following the impact on a damper is plotted in figure 3.1(a). The overall shape of the signal is symmetric about the time at which the maximal acceleration is reached. Additionally, the signal is close to triangular. From such a recording, we extract the maximum acceleration of the shock a and its characteristic timespan τ , defined as the full width at half maximum, *i.e* the width of the signal at $\dot{U} = a/2$.

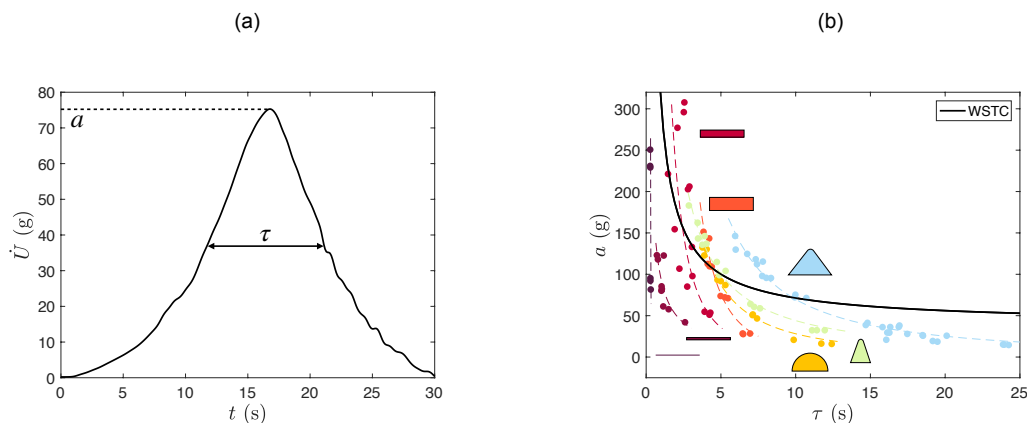


Figure 3.1: (a) Typical time evolution of the acceleration \dot{U} of the reservoir after impact on the damper ($t = 0$). a is defined as the maximum acceleration of the container during the shock. τ is the width of the signal at $\dot{U} = a/2$. In this particular case, $a = 75$ g and $\tau = 9$ ms. (b) Range of shocks accessible in the diagram (a, τ) . Properties of the shock depend on the damper and the height at which the falling mass is released. Shape and thickness of the damper is varied from flat (red-orange curves, lighter color are thicker dampers) to conical (green blue) and spherical dampers (yellow). Dashed lines are the mean trend for each damper. WSTC is plotted in solid black line.

We vary the parameters (a, τ) of an impact on a damper by changing the height at which the falling stage of the drop tower is released or by modifying the properties of the damper. The properties of the damper that are varied are its shape (cylindrical, conical, hemispherical), its thickness and its Young's modulus. As the Young's modulus of the polymer is only tunable in the range 0.2 to 0.7 MPa, we mainly vary the shape and the thickness of the damper. Doing so, the range of accessible impacts in the (a, τ) diagram is shown in figure 3.1(b). For each damper, a characteristic curve $a(\tau)$ is obtained by varying the drop height. We observe consistently that a is decreasing with the shock duration τ . Flat dampers produce shock of peak acceleration ranging from 30 to 300 g with short duration τ between 0 and 7 ms. This duration is also observed to increase with the thickness of the damper (orange curve). Other geometries of damper (hemispherical and conical) produce a smaller acceleration (0 to ~ 200 g) but a shock duration up to $\tau = 25$ ms. Overall, the region of accessible shocks with our set-up is delimited by an hyperbolic-like curve.

Most importantly, with the aim of applying this work to brain concussion, this set-up allows us to explore the relevant part of the (a, τ) diagram. Indeed, the Wayne State Tolerance Curve (WSTC), plotted in figure 3.1(b) (solid black line), goes through our accessible range of shocks from $\tau = 0$ ms up to ~ 10 ms. This is satisfactory as the WSTC is found to

depend on τ only in this range of timespan of the impact: for $\tau > 10$ ms, the WSTC is fairly flat.

3.1.2 Radius of the cavitation bubble

The aim of this chapter is to determine the influence of the shock duration on the dynamic of a cavitation bubble. To that end, only the flexible membranes ($K \approx 1$ N/m) are used as the rigid one does not allow bubble growth. However, we have seen in the previous chapter that many bubbles nucleate in the *contrecoup* area which makes the tracking of the bubble radius difficult and generate interactions [53, 54, 55, 56]. To avoid these effects, we seed degasified water with a unique bubble of radius $R_0 = 1$ mm, initially located in the *contrecoup* area. The evolution of this bubble is tracked during the shock with a fixed high-speed camera. The resulting chronophotography is shown in figure 3.2(a) for a shock of peak acceleration $a \approx 100$ g and timespan $\tau \approx 3.7$ ms. At the beginning of the shock ($t = 0$), the bubble has a radius $R \approx 1$ mm. It then slowly grows until it reaches its maximum radius R_{max} of around 1 cm at $t = 6.4$ ms. It then rapidly collapses in about a millisecond.

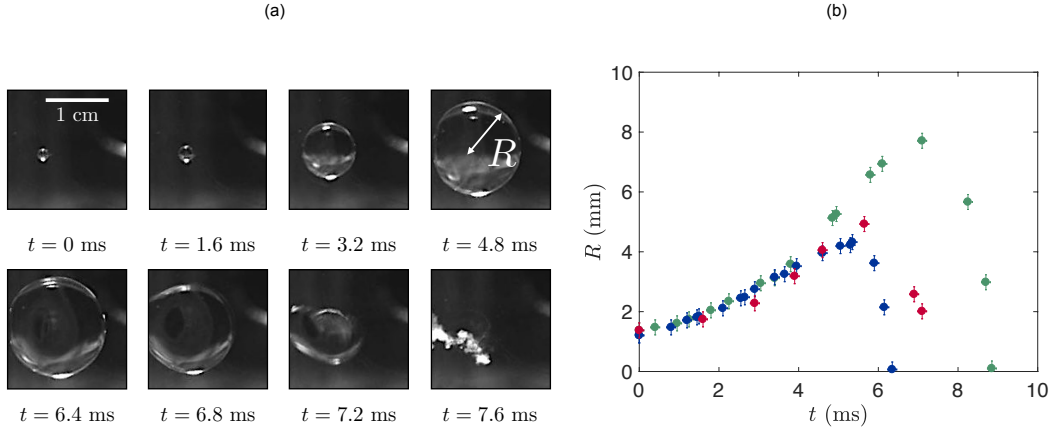


Figure 3.2: (a) Chronophotography of a single bubble growing in the *contrecoup* area during a shock of maximum acceleration $a \approx 100$ g and timespan $\tau = 3.7$ ms. A pressure sensor is used to monitor the pressure in the *contrecoup* region. The container is equipped with a flexible membrane ($K \approx 1$ N/m). (b) Time evolution of the bubble radius R . Blue data are for a shock with peak acceleration $a = 77$ g and timespan $\tau = 4.9$ ms. Red: $a = 69$ g and $\tau = 5.4$ ms. Green: $a = 82$ g and $\tau = 5.4$ ms.

The radius R is precisely tracked for different shocks and figure 3.2(b) collects data for three growths in a container equipped with a flexible membrane. In each case, we recover the previously noticed behaviour: bubbles expand to their maximum radius R_{max} before rapidly collapsing. For instance, for $a = 82$ g and $\tau = 5.4$ ms, the bubble grows from $R_0 = 1$ mm to $R_{max} = 7.5$ mm (corresponding to a volume increase by a factor 420) in 7 ms, before collapsing in about 1 ms. R_{max} is observed to increase with the acceleration a (red/green curves), but also with the shock duration τ (blue/green curves).

3.1.3 Numerical methods

We wish to compare these time evolutions of the bubble radius with solution of Rayleigh-Plesset equation. Let us recall the Rayleigh-Plesset (RP) equation:

$$\frac{3}{2}\rho\dot{R}^2 + \rho R\ddot{R} + \frac{4\eta}{R}\dot{R} + \frac{2\gamma}{R} = \Delta p \quad (3.1)$$

Where $\Delta p = p_b - P(t)$ is the pressure difference across the interface of the bubble. In the rest of the section, *ode15i*, a solver for fully implicit ordinary differential equations implemented in Matlab, is used to numerically integrate equation (3.1). We first compare the numerical solution to the analytical one in the small perturbations regime. For large perturbations, we show that we recover results of previous studies.

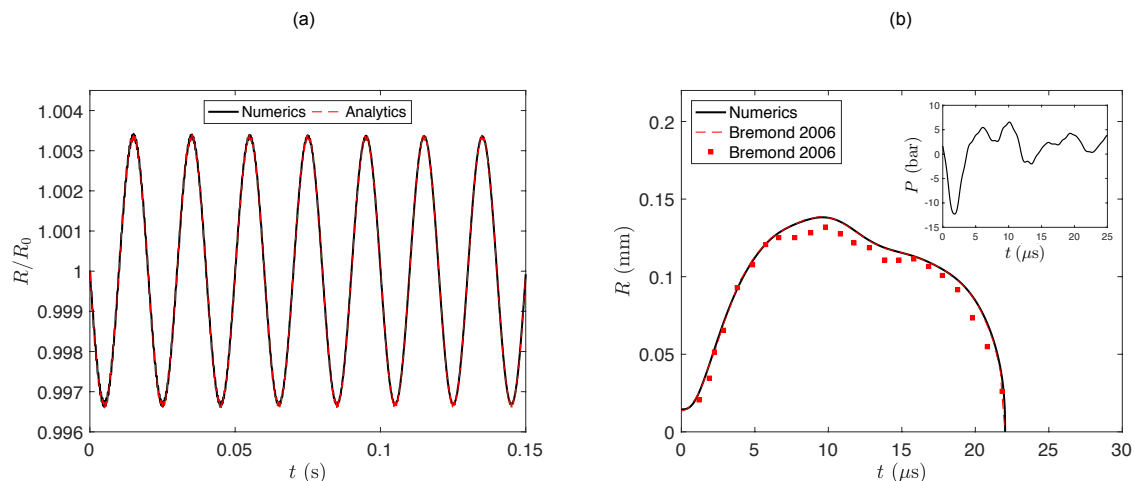


Figure 3.3: (a) Comparison between the numerical integration of Rayleigh-Plesset equation and the analytical solution of the time evolution of the dimensionless radius of the bubble R/R_0 in the small perturbations regime. The external pressure is sinusoidal: $P = P_0 + p_0 \sin(\omega t)$ with $p_0 = 0.01P_0$ and $\omega = 315 \text{ s}^{-1}$. Initial radius is 1.3 mm. Numerical integration is performed using Matlab *ode15i* and is plotted in solid black line. Analytical solution (dashed red line) is given by equation (3.6) and results from the resolution of the Rayleigh-Plesset equation truncated to the first-order. (b) Comparison between our numerical integration (solid black line) of Rayleigh-Plesset performed with *ode15i*, the numerical solution (dashed red line) and experimental data (squares) from [53] for the time evolution of the radius of the bubble in the large pressure drop regime. The bubble is initially trapped in a pit of diameter ($20 \mu\text{m}$). Integration is performed for the experimental pressure signal reported in [54, 53] and reproduced in the inset.

3.1.3.1 Small perturbations

We first consider the simple case of a bubble in an oscillating pressure field of the form: $P(t) = P_0 + p(t)$ where $p(t)$ is a sinusoidal dynamic pressure $p(t) = p_0 \sin(\omega t)$ with $p_0 \ll P_0$. For such small external perturbations, the radius of the bubble R remains close to its initial value R_0 , such that it can be written:

$$R(t) = R_0(1 + \epsilon(t)) \text{ with } \epsilon \ll 1 \quad (3.2)$$

Initially, the bubble is at rest (*i.e.* $p_b = P_0 + 2\gamma/R_0$) and its constituting gas undergoes an isothermal transformation: $p_b = (P_0 + 2\gamma/R_0) \left(\frac{R_0}{R}\right)^3$. Substituting this relation and equation (3.2) in RP equation yields, in the first-order approximation:

$$\ddot{\epsilon} + \alpha \dot{\epsilon} + \beta \epsilon = -\frac{p(t)}{\rho R_0^2} \quad (3.3)$$

where $\alpha = \frac{4\eta}{\rho R_0^2}$ and $\beta = \frac{3P_0 + 4\gamma/R_0}{\rho R_0^2}$.

For the initial radius considered ($R_0 \approx 1$ mm), $\alpha^2 - 4\beta < 0$ and the homogeneous solution of equation (3.3) takes the form:

$$\epsilon_h = \exp(-t/t_c) (A \cos(\omega_0 t) + B \sin(\omega_0 t)) \quad (3.4)$$

with $t_c = 2/\alpha$ and $\omega_0 = \sqrt{\beta - \alpha^2/4}$

A particular solution is:

$$\epsilon_p = \epsilon_0 \sin(\omega t + \Phi) \quad (3.5)$$

where $\epsilon = \frac{p_0}{\sqrt{(\beta - \omega^2)^2 + \alpha^2 \omega^2}}$ and $\Phi = \pm \pi \arctan\left(\frac{-\alpha\omega}{\beta - \omega^2}\right)$ if $\beta - \omega^2 > 0$.

Imposing the initial conditions $\epsilon(0) = \dot{\epsilon}(0) = 0$, the solution to equation (3.1) is:

$$\epsilon(t) = \epsilon_0 \left[\sin(\omega t + \Phi) + \exp(-t/t_c) \left(-\sin \Phi \cos(\omega_0 t) - \left(\frac{\sin \Phi}{\omega_0 t_c} + \frac{\omega \cos \Phi}{\omega_0} \right) \sin(\omega_0 t) \right) \right] \quad (3.6)$$

For the characteristic timespan of the impacts in our experimental set-up ($\omega \approx 315$ s⁻¹), and a perturbation pressure $p_0 = 0.01P_0$ we plot this analytical solution and the numerical integration of equation (3.1) performed using Matlab solver *ode15i* in figure 2.2(a). We observe a good agreement between the analytical solution (dashed red line) and the result of the numerical simulation (solid black line). Both curves have a sinusoidal behaviour of frequency $f = \omega/2\pi \sim 50$ Hz and an amplitude of 0.3 % of R_0 .

In the range of time scales of our experiments, numerically integrating RP using *ode15i* is efficient to recover the oscillatory behaviour predicted analytically.

3.1.3.2 Large perturbations

To determine if the solver we used also performs well for large pressure variations, we impose a pressure drop of -1.4 MPa and half-width $\tau \approx 2$ μ s and follows the time evolution of the radius of the bubble. To allow comparison with previous studies, we take the pressure signal recorded in [54, 53] as our input pressure. The time evolution of this pressure signal is plotted in the inset of figure 2.2(b).

The result of our numerical integration -using *ode15i*- is plotted in figure 2.2(b) (solid black line) alongside data (squares) and simulation (dashed red line) from the literature [53]. The two numerical simulations are in excellent agreement with each other and well describe the experimental data reported in [53].

The radius of the bubble rapidly grows from ~ 10 μ m to ~ 0.17 mm. Interestingly, this maximum value is reached at $t \approx 10$ μ s, long after the end of the pressure drop (~ 4 μ s), suggesting that inertia plays a crucial role in the overall dynamic. After that, the radius of the bubble slowly decreases to ~ 0.1 mm at $t \approx 20$ μ s before rapidly collapsing ($R = 0$ at $t \approx 22$ μ s). The relatively slow diminution of the radius in the first part of the collapse is attributed to the presence of a second pressure drop (~ 3 bar) recorded around $t = 12$ μ s.

As a consequence, the fully implicit solver for ordinary differential equations implemented in Matlab *ode15i* accurately solve the Rayleigh-Plesset equation for the characteristics time scales and large pressure drop expected in our experiments.

3.2 Bubble dynamics

3.2.1 Rayleigh-Plesset equation

Using the pressure evolution recorded experimentally, we solve the RP equation numerically. The solutions are drawn in dashed line in figure 3.4(a) and are found to describe in a satisfactory way the asymmetric behaviour. It is surprising to note that, even though this equation is based on the assumption of a spherically-symmetric flow around a spherical bubble, which break when the bubble implodes near the wall of the container, it still captures, for these cases, fairly well the collapse.

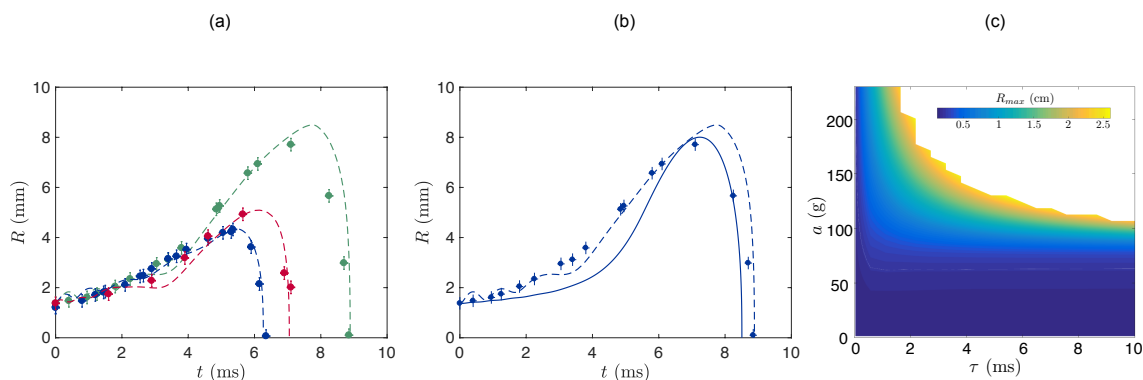


Figure 3.4: (a) Time evolution of the bubble radius R . Blue data are for a shock with peak acceleration $a = 77$ g and timespan $\tau = 4.9$ ms. Red: $a = 69$ g and $\tau = 5.4$ ms. Green: $a = 82$ g and $\tau = 5.4$ ms. Dashed lines are numerical solutions of RP equation with the experimentally measured pressure. (b) Time evolution of the bubble radius for a shock with peak acceleration $a = 77$ g and timespan $\tau = 4.9$ ms. Dashed line is the numerical solution of the Rayleigh-Plesset equation solved with the pressure measured experimentally. Solid line is the numerical solution of the Rayleigh-Plesset equation solved with a triangular pressure with peak value $\rho a L$ and half-width τ . (c) Maximum radius of a bubble in the diagram (a, τ) for a triangular time evolution of the pressure after a shock of peak acceleration a and timespan τ . The initial radius of the bubble is 1.4 mm and the bubble is located in the *contrecoup* region.

3.2.2 Maximum radius of a bubble

We focus here on the determination of the maximum radius R_{max} of the bubble and we wish to express it as a function of the couple (a, τ) . To do so, we model the time evolution of the pressure during a shock with only parameter the couple (a, τ) . Given the form of the signal of the acceleration presented in figure 3.1(a), we approximate this signal as triangular of peak value a and width at half height τ . In the flexible regime, the dynamic pressure in the *contrecoup* region is then also triangular of maximum value $\rho a L$ and half width τ . With this model signal, we solve the RP equation and plot the time evolution of the radius in figure 3.4(b). We observe that the overall asymmetric dynamics of the bubble remains unchanged when using this signal. However, while the growth is steady with the measured pressure signal, the growth rate varies with the model pressure signal: the bubble radius barely increases before $t = 4$ ms (it changes from 1.4 mm to 2.5 mm), but rapidly catches up to reach a maximum radius R_{max} close to the one measured at $t \approx 7$ ms. Overall, the model signal captures fairly well the bubble dynamics but, most importantly, it describes well the maximum radius R_{max} .

From that, we numerically integrate the RP equation for any shock determined by its couple (a, τ) . The computed maximum radius R_{max} is displayed in the (a, τ) diagram in figure 3.4(c). We first notice that, accordingly to what was previously observed, R_{max} is monotonously increasing with both the peak acceleration and the timespan of the shock. We also remark that the diagram can be split into two regimes: below $a = 60$ g, *i.e.* the low acceleration regime, maximum radius remains close to R_0 and R_{max} only depends on a . In the high acceleration regime ($a > 90$ g), R_{max} is growing rapidly with the timespan of the shock τ : for $a = 200$, R_{max} passes from 5 mm at $\tau \approx 0.5$ ms to 2.5 cm at $\tau \approx 2$ ms. These two regimes will be investigated in greater details in the next sections.

3.2.3 Low acceleration regime

In this regime, the accelerations are smaller than 60 g and, hence, the total pressure in the *contrecoup* area is always greater than the vapor pressure of water. As a consequence, apart for very short shocks ($\tau < 1$ ms), the rate of change of the pressure is small when compared to the period of deformation of the bubble. We consider that the bubble is always in quasi-static equilibrium with the surrounding fluid. This writes $p_b(R) = P(t) + \frac{2\gamma}{R}$, where p_b is the internal pressure of the bubble and P the total pressure in the *contrecoup* region. With $R > 1$ mm, this relation simplifies to:

$$p_b \approx P \quad (3.7)$$

Assuming an isothermal transformation of the gas in the bubble we can write:

$$\frac{p_b(R)}{p_b(R_0)} = \frac{\frac{4}{3}\pi R^3}{\frac{4}{3}\pi R_0^3} \quad (3.8)$$

Substituting (3.7) in (3.8) and solving for R yields an equilibrium radius R_{eq} :

$$R_{eq} \approx R_0 \left(\frac{P_0}{P} \right)^{1/3} \approx R_0 \left(\frac{P_0}{P_0 - \rho a L} \right)^{1/3} \quad (3.9)$$

where we used the potential expression of the pressure in the *contrecoup* area for a container equipped with a flexible membrane: $P = P_0 - \rho a L$.

The ratio R_{max}/R_{eq} is computed from the results of the numerical resolution of RP equation (presented in figure 3.4) and displayed as a function of τ for different values of the peak acceleration of the shock a in figure 3.5(a). We remark that all the numerical simulations curves collapse along an horizontal line of value 1, which suggests that we accurately identified the underlying mechanism of this regime. Divergences from this line arise when the pressure variation rate ($\frac{dP}{dt} \approx \frac{a}{\tau}$) is great, which is the case either for short shocks ($\tau < 2$ ms) or for the largest acceleration of this regimes ($a \approx 60$ g). Additionally, both the theoretical static equilibrium and the numerical simulation are in fair agreement with the experimental observations.

3.2.4 High acceleration regime

In the high acceleration regime, the viscous and capillary terms of the Rayleigh-Plesset equation are negligible when compared with the inertial effects: The equivalent Reynolds number is $Re = \frac{aR/\tau}{\nu} \sim 10^9 \gg 1$ and Weber number is $We = \frac{\rho(a/\tau)^2 R}{\gamma} \sim 10^{13} \gg 1$. Multiplying equation (3.1) by $R^2 \dot{R}$, we get:

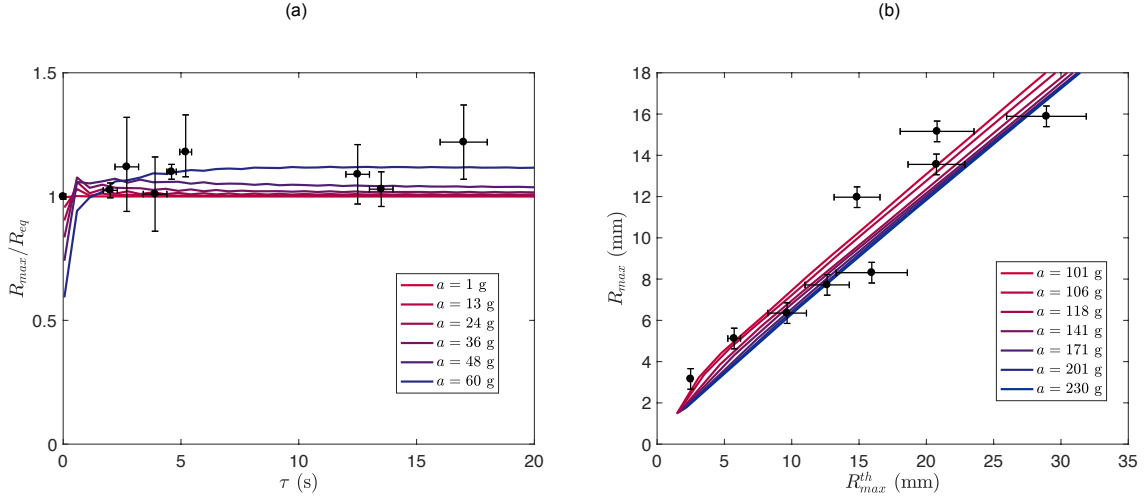


Figure 3.5: Maximum radius of the bubble in the different acceleration regimes. (a) Low acceleration regime: ratio of the maximum radius of the bubble R_{max} to its equilibrium radius R_{eq} (equation (3.9)) as a function of the timespan of the shock τ . Solid lines show numerical simulations for peak acceleration a ranging from 1 to 60 g. (b) High acceleration regime: Maximum radius R_{max} compared to its analytical value (equation (3.14)). Solid lines show numerical simulations for shock accelerations ranging from 101g to 230g.

$$\frac{d(\rho R^3 \dot{R}^2)}{dt} = 2\Delta P R^2 \dot{R} \quad (3.10)$$

which we can see as the time evolution of the kinetic energy of the fluid entrained by the bubble arising from the work of the pressure force at the bubble interface. An analytical solution of this equation exists assuming that the shock is a crenel of amplitude a and width τ , *i.e.* P is constant by part. Within the isothermal framework, we have $\Delta P = p_b - P = P_{vap} + \left(P_0 + \frac{2\gamma}{R}\right) \left(\frac{R_0}{R}\right)^3 - P$, which simplifies into $\Delta P \approx P_{vap} - P$ as $R \gg R_0$ in this regime. Hence ΔP is also constant by part. We integrate equation (3.10), and express R at the time τ , *i.e.* the end of the shock:

$$R(\tau) = R_0 + \sqrt{\frac{2\Delta P}{3\rho}} \tau \quad (3.11)$$

In a second phase, after the shock, the pressure falls back to the ambient pressure $P_0 \gg P_{vap}$ and equation (3.10) simplifies to:

$$\frac{d(\rho R^3 \dot{R}^2)}{dt} \approx -2P_0 R^2 \dot{R} \quad (3.12)$$

At maximum radius we have $\dot{R}(R_{max}) = 0$. We integrate equation (3.12) in the second phase with the initial condition given by equation (3.11) and get:

$$R_{max}^3 = \left(R_0 + \sqrt{\frac{2\Delta P}{3\rho}} \tau\right)^3 + \frac{3\rho}{2P_0} \left(R_0 + \sqrt{\frac{2\Delta P}{3\rho}} \tau\right)^3 \frac{2\Delta P}{3\rho} \quad (3.13)$$

With $P_{vap} = \rho a_v L$, we have $\Delta P = \rho(a_v - a)L$ and ultimately find:

$$R_{max} \approx R_0 + \left(\frac{3\rho}{2P_0} \right)^{\frac{1}{3}} \left(\frac{2(a - a_v)L}{3} \right)^{\frac{5}{6}} \tau \quad (3.14)$$

In figure 3.5(b), we compare our data (obtained at various a and τ) with the values expected from equation (3.14). We find a fair correlation: data align when plotted as a function of the theoretical radius. The slope of the line is around 1/2, which can be understood when plotting also the numerical solutions of the RP equation, assuming a triangular peak of acceleration instead of a crenel: the solutions are then found to fit well the data, suggesting that the numerical coefficient in the law depends on the shape chosen for the temporal evolution of the acceleration.

3.3 Damaging potential

The damaging potential of a cavitation bubble can be evaluated via the energy storage E . This energy is gathered through the work of the pressure forces across the interface of the bubble:

$$E \sim \delta P R_{max}^3 \sim \rho a L R_{max}^3 \quad (3.15)$$

This energy will be released during the collapse through a combination of local increase of temperature [57], creation of a shock wave [58, 59] and eruption of a fast jet [60, 61], if collapse occurs near a solid boundary. As presented in chapter 1, the importance of each mechanism in the damaging process is debated [62, 63], but all of them involve energy focusing, which is also the case for brain concussion.

For the parameters of the head, following the process used to obtain figure 3.4(b), we compute the maximum radius and energy of cavitation bubbles after a triangular shock with peak acceleration a and half-width τ . From that, we calculate the energy of the cavitation bubbles using equation (3.15) and we plot in figure 3.6 the iso-energy curves in a (a, τ) diagram. The energy E is varied from 0.4 mJ to 8.5 J. For small energies (blue curves in figure 3.6), the iso-energy curves are almost angular, with a plateau at large τ (>3 ms) and a strong divergence at small τ (< 0.5 ms). The plateau value is $a \approx 70$ g, that is, the acceleration necessary to generate cavitation in the *contrecoup* region. Curves get higher and smoother when increasing E , and they eventually follow a close-to-hyperbolic behavior when E is on the order of 1 J (red curves). Remarkably, a well-defined value of the energy, namely $E_D = 8.5$ J, is found to match the WSTC (dashes) in the range 0 to ~ 2 ms of shock duration. Above $\tau \approx 2$ ms, our results predict damages for higher acceleration than the WSTC. This result is coherent with the observations gathered in [64], based on cadaver and alive animal tests, suggesting that the plateau value of the curve is higher and closer to 100 g.

The value of E_D can itself be rationalized: this energy is released in a volume Ω set by the jet radius (fast jet damaging mechanism) or by the initial bubble radius (shock wave mechanism), in both cases smaller than one cubic millimeter. The corresponding local increase of pressure $p \approx E/\Omega$ is greater than 10 MPa, that is, large enough to damage all kinds of brain tissues [65] and even the skull itself [66].

For $E = E_D$, we are in the high acceleration regime and we also have $R_{max} \gg R_0$ and

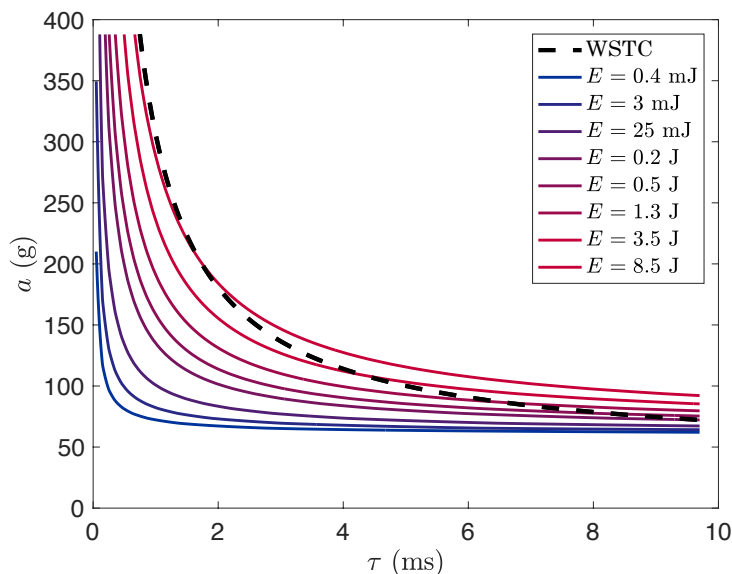


Figure 3.6: Iso-energy curves in the (a, τ) diagram and comparison with the Wayne State University Curve. The energy $E = \rho a L R_{max}^3$ released by a bubble is calculated using equation (3.15), which allows us to plot iso-energy curves in the (a, τ) diagram. Varying E between 0.4 mJ and 8.5 J generates a family of curves that gradually evolve towards the WSTC (dashes) as E increases. The value at which they match is $E_D=8.5$ J.

$a > a_v$ so that equation (3.14) becomes the simple scaling law:

$$R_{max} \sim \left(\frac{\rho}{P_0} \right)^{\frac{1}{3}} (aL)^{\frac{5}{6}} \tau \quad (3.16)$$

Hence, substituting this relation in equation (3.15), we can derive a simple severity criterion SCC for cavitation damages:

$$SCC \sim E_D \sim a^{\frac{7}{2}} \tau^3 \quad (3.17)$$

which yields a threshold acceleration a of damage scaling as $E_D/\tau^{\frac{6}{7}}$. This behavior is close to be hyperbolic in τ , and its characteristic exponent $(-6/7)$ is comparable to that of the WSTC, found to decay as τ^α with $\alpha = -0.92 \pm 0.03$. This suggests that a scenario exclusively based on cavitation not only captures most of the characteristics of traumatic brain injuries (damages appear at acceleration greater than 50 g and locate in the contrecoup region), but also quantitatively recover the observations of the heuristic WSTC: shorter shocks require larger acceleration to be harmful.

3.4 Futur developments

The work presented in this chapter lead to research focuses:

- Refinement of the experimental set-up to take into account specificities of the in-vivo system (skull, brain and cerebrospinal fluid). This include : the growth of bubbles in a confined environment, the influence of a soft solid of the bubble dynamics and the interaction between multiple bubbles.
- Development of a method to detect cavitation events in the head of a rugby player.

In the rest of the section, we briefly describe these two axis.

3.4.1 Bubble interaction

The interaction between multiple bubbles influences their dynamics and was thoroughly studied in the literature [53, 54, 55, 56]. However, most of the studies focus on the interactions between bubbles of roughly the same initial size. In the in-vivo system, we expect the initial size of the bubble to vary over large range and hence, we wish to look into the interactions of bubbles of different sizes.

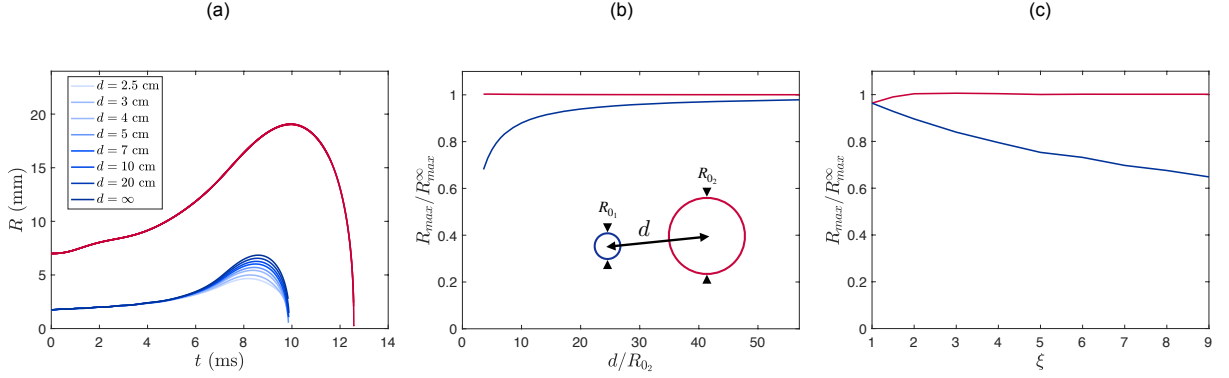


Figure 3.7: (a) Time evolution of the radius R of two asymmetric bubbles following a shock of peak acceleration $a = 70$ g and timespan $\tau = 7$ ms. Red line is the radius of the large bubble of initial value $R_{02} = 7$ mm. Blue lines are the radii of the small bubble of initial value $R_{01} = R_{02}/\xi$, with $\xi = 4$. Distance d between the center of the two bubbles is varied from 2.5 cm to infinity. Different value of d are not distinguishable for the large bubble. (b) R_{max}/R_{max}^{∞} as a function of the dimensionless distance between the bubbles d/R_{02} for a shock of peak acceleration $a = 70$ g and timespan $\tau = 7$ ms. Asymmetry between the bubbles is $\xi = R_{02}/R_{01} = 4$. R_{max} is the maximum radius of a bubble. R_{max}^{∞} is the maximum radius of a bubble when infinitely far from the other one. Red line is for the larger bubble. Blue line is for the smaller bubble. (c) R_{max}/R_{max}^{∞} as a function of the asymmetry between the bubbles $\xi = R_{02}/R_{01}$ for a shock of peak acceleration $a = 70$ g and timespan $\tau = 7$ ms. The two bubbles are separated by $d = 2.5$ cm. Red line is for the larger bubble. Blue line is for the smaller bubble.

To that end, we consider the simplest case of two bubbles of initial radius R_{01} and R_{02} , with $R_{02} > R_{01}$, which centers are separated by a distance d . In this system, the Rayleigh-Plesset equation is replaced by the following system of two coupled equations:

$$\begin{cases} \frac{3}{2}\rho\dot{R}_1^2 + \rho R\ddot{R}_1 + \frac{4\eta}{R_1}\dot{R}_1 + \frac{2\gamma}{R_1} + \rho\frac{R_2^2\ddot{R}_2 + 2R_2\dot{R}_2^2}{d} = \Delta p \\ \frac{3}{2}\rho\dot{R}_2^2 + \rho R\ddot{R}_2 + \frac{4\eta}{R_2}\dot{R}_2 + \frac{2\gamma}{R_2} + \rho\frac{R_1^2\ddot{R}_1 + 2R_1\dot{R}_1^2}{d} = \Delta p \end{cases} \quad (3.18)$$

We first solve this system for the growth of two asymmetric bubbles at various distance d following a shock of peak acceleration $a = 70$ g and timespan $\tau = 7$ ms. We define ξ the ratio of the initial radius of the two bubbles: $\xi = \frac{R_{02}}{R_{01}} > 1$. For $\xi = 4$ we plot the time evolution of the radii of the two bubbles in figure 3.7(a). We vary the distance d from 2.5 cm to infinity, *i.e.* equivalent to the study of the growth of a unique bubble. No matter how close the two bubbles are, we recover the dynamic previously observed: bubbles slowly grow to reach their maximum radius R_{max} , after what they rapidly collapse. The large bubble

(red curve), is barely affected by the presence of a small bubble in its vicinity: curves for different distances cannot be distinguished in figure 3.7(a). However, the dynamic of the small bubble (blue curve) is largely modified by the presence of the large bubble. The curve of the time evolution of the radius R_1 flattens and becomes more symmetric as the two bubbles are brought closer: when alone ($d = \infty$) the small bubble reaches a maximum radius of ~ 7 mm while it barely reaches ~ 5 mm when the two bubbles are 2.5 cm apart.

We then concentrate on the maximum radius of the bubble R_{max} , which we prove to be a quantification of the stored energy, and compare it with the maximum radius that the bubble would reach if it was alone R_{max}^∞ . We plot in figure 3.7(b) the ratio R_{max}/R_{max}^∞ as a function of the dimensionless distance d/R_{0_2} between the bubbles for $\xi = 4$. Looking at the maximum radius of the larger bubble (red curve, R_2), we retrieve the fact that it is not affected by the smaller bubble ($R_{max_2}/R_{max_2}^\infty = 1$). Nonetheless, the maximum radius of the smaller bubble is reduced by the presence of the larger one. This influence is reduced when the two bubbles are spread apart: $R_{max_1}/R_{max_1}^\infty$ onsets at ~ 0.7 when $d/R_{0_2} \approx 3.5$ and then tends to 1 when d/R_{0_2} goes to infinity ($R_{max_1}/R_{max_1}^\infty \approx 0.98$ for $d/R_{0_2} \approx 50$).

Finally, we investigate the dependence of the maximum radii on the asymmetry of the two bubble $\xi = \frac{R_{0_2}}{R_{0_1}}$ as displayed in figure 3.7(c), where R_{max}/R_{max}^∞ is plotted against ξ for $d/R_{0_2} = 3.6$. When the two bubbles are identical ($\xi = 1$), their maximum radius is slightly reduced when compared to the case of an unique bubble ($R_{max}/R_{max}^\infty \approx 0.95$). However, as soon as the asymmetry is increased, the larger bubble reaches its plateau value for its maximum radius ($R_{max_2}/R_{max_2}^\infty = 1$ for $\xi \approx 2$) while the smaller bubble has its growth inhibited ($R_{max_1}/R_{max_1}^\infty$ decreases and reach ~ 0.6 for $\xi \approx 9$).

Although this dependencies should be investigated experimentally, we can already say that interaction between bubbles should not influence the maximum damaging potential of cavitation bubbles created after a shock on the head. Indeed, it can be evaluated taking the largest nucleus which will grow to the largest bubble being only slightly influenced by others.

3.4.2 In-vivo Measurements

We wish to detect cavitation events in the head of sports players (especially in rugby or boxing) to facilitate the diagnostic of brain concussion during a game. As we mentioned before, it is currently based on an on-field clinical test which leaves more than 30 % of the concussions undetected before the end of the game. As a consequence, players face greater aftermaths and longer recovery times.

To that end, we wish to use the characteristic noise generated at the collapse of a cavitation bubble, already thoroughly studied in diverse situations [67, 68, 69]. Here we present the in-vitro illustration of the set-up we wish to develop for sports players. The experimental set-up is sketched in figure 3.8(a). Apart from the fact that two accelerometers are used, it is identical to the one previously described: it consists of a reservoir, equipped with a flexible membrane, accelerated vertically upon a shock on a damper. The first accelerometer (A_1) is located on the outer wall of the *contrecoup* region while the other (A_2) is on the falling stage of the impact tower. For a shock of peak acceleration $a = 135$ g and timespan $\tau \approx 2$ ms, the time evolution of the acceleration measured by the two accelerometers is shown in figure 3.8(b). The acceleration measured by the second accelerometer (blue curve) only consists of a typical shock of peak acceleration ~ 120 g and half-width ~ 2 ms. However, the first accelerometer not only measures roughly the same shock, but also captures a high intensity (~ 200 g) and frequency signal 8 milliseconds after the beginning of the impact. Figure 3.8(c) displays a choronophotography of the *contrecoup* region during the shock. Initially, no bubbles are present in the container. 1.5 ms after the shock, a cloud of millimetric bubbles

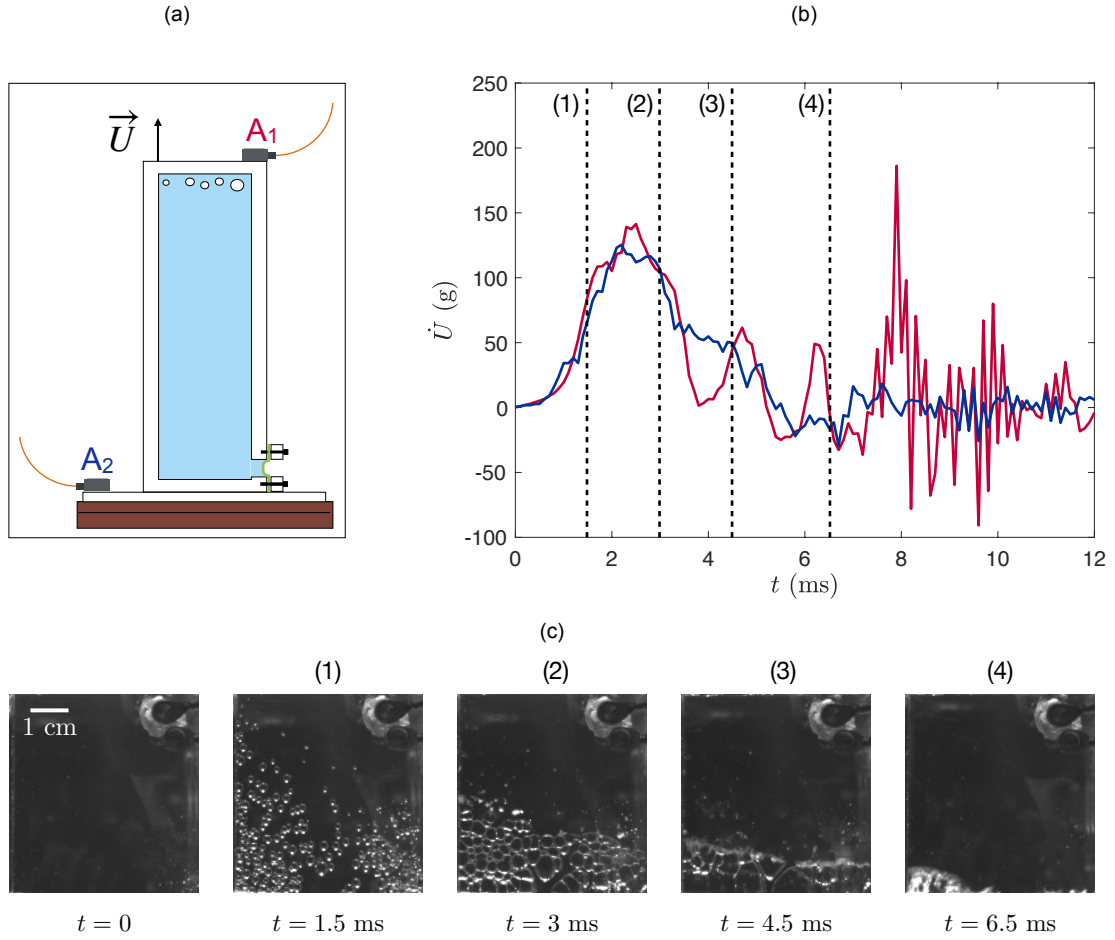


Figure 3.8: (a) Sketch of the experimental set-up used to detect in-vitro cavitation event using accelerometers. The first accelerometer (A_1) is located on the outer wall of the *contrecoup* area. The second accelerometer (A_2) is located on the falling stage of the impact tower. (b) Acceleration \dot{U} measured by two accelerometers when a container, equipped with a flexible membrane, is accelerated at a peak acceleration 145 g for $\tau \approx 2$ ms. Signal recorded by the first accelerometer is plotted in red. Signal recorded by the second accelerometer is plotted in blue. (c) Chonophotography of the *contrecoup* area. Accelerometer 1 is located on the top-right corner of the pictures.

have developed in the *contrecoup* area. After that, bubbles only grow in the bottom part of the image (suggesting that, for this shock, the acceleration is not perfectly vertical) while they collapse in the upper part of the image. At $t = 3$ ms, all bubbles start collapsing until they completely disappear shortly after $t \approx 6.5$ ms. This suggests that the signal recorded by the first accelerometer starting 7 ms after the shock corresponds to the collapse of the cavitation bubbles on the wall of the container in the *contrecoup* area.

Hence, a cavitation event in our in-vitro experimental set-up can be detected using an accelerometer placed on the outer wall of the container, near the *contrecoup* region. We expect this to be reproducible in-vivo, with rugby players.

Take home message of Part I

1. **A pressure drop** is measured in the region opposite of impact (*contrecoup* area) when a container of length L filled with water is accelerated by a shock of peak acceleration a and characteristic timespan τ . For a container equipped with a flexible membrane, the pressure drop has a magnitude $\delta P = \rho a L$ while it is $\delta P = \frac{1}{2} \rho a L$ when the container is completely rigid.
2. **Cavitation onset** in a confined environment is determined by the cavitation number Ca introduced in [13]. For a deformable container, cavitation occurs for $Ca \approx 1$. However, for non-deformable container, the **incompressibility condition** prevent bubbles from nucleating.
3. **Growth of the bubble** during a shock is accurately predicted by Rayleigh-Plesset equation. The maximum radius of the bubble R_{max} can be analytically predicted for a crenel shock. We find: $R_{max} \approx R_0 + \left(\frac{3\rho}{2P_0}\right)^{\frac{1}{3}} \left(\frac{2(a-a_v)L}{3}\right)^{\frac{5}{6}} \tau$. In particular, this shows that the **characteristic time of the shock** is a crucial parameter and that considering only the peak acceleration of the shock is not sufficient to fully capture the behaviour of cavitation bubbles in an accelerated container.
4. **Maximum radius of the bubble** quantify the energy E it stores. E is found to scale as $\delta P R_{max}^3 \sim \rho a L R_{max}^3$. This is also the damaging potential of a bubble.
5. **Damages caused by cavitation** in a brain concussion scenario can account for the overall observations gathered in the Wayne State University Tolerance Curve (WSTC).
6. This work is expected to lead to improvement of the detection of brain concussions in sports (using the characteristic noise produced at the collapse of cavitation bubbles) as well as to lead to the development of new safety gears (such as self-rigidifying necklaces that would limit cavitation bubbles).

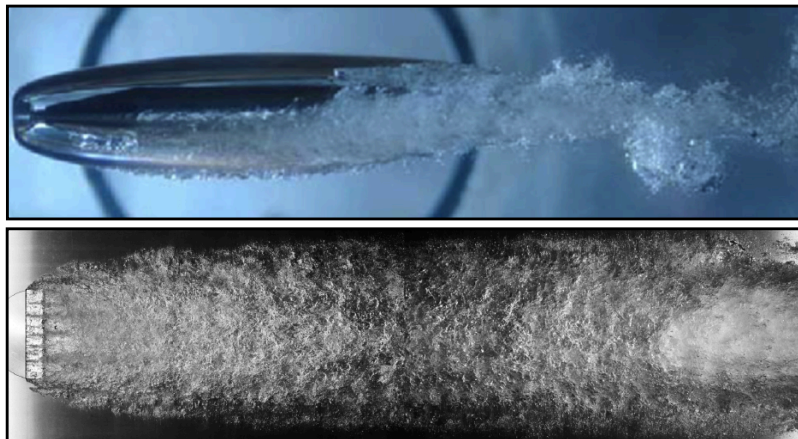
PART II

CHARACTERISATION OF A SUPERCAVITATING SPHERE NEAR THE DRAG CRISIS

We have seen in the previous part that a pressure drop can trigger the growth of cavitation bubbles. As a consequence, if an underwater projectile travels fast enough, *i.e.* at a small enough cavitation number, it enters the supercavitation regime. In this regime, the pressure around the projectile is far below the vapor pressure of the liquid, such that a large cavitation bubble develops around the projectile. We wish to quantify the drag modification induced by the presence of such a bubble. As we stated before, this regime is experimentally difficult to reproduce. However, the natural bubble created through cavitation can be mimicked via artificial gas injection. This system is called ventilated cavities and is going to be the main focus of this part. First, we briefly review earlier works on the subject. We then present our experimental set-up designed to study ventilated cavities behind spheres near the drag crisis. Finally, we focus on the main results of our study, which address how the morphology of the ventilated cavity affect the drag of the projectile.

4

SHORT REVIEW ON VENTILATED CAVITIES



Ventilated cavities behind a disk (top picture) and a fence (bottom picture).

Contents

4.1	Generalities on ventilated cavities	48
4.2	Ventilated cavities in the wake of projectiles	49
4.3	Statement of the problem	53

4.1 Generalities on ventilated cavities

The entry in the supercavitation regime necessitates a projectile moving at several tens of meters per second which largely complicates its study. It also reduces the broadness of the field of application. However, under certain conditions, gas injection (usually air) around an underwater projectile can generate a large air cavity, often referred as a ventilated cavity, which mimics the supercavitation regime. In other terms, everything happens as if the phase transition from liquid to gas of water was replaced by an artificial supply of air. Starting from this observation, one question should be addressed: is a drag reduction, the main advantage of the supercavitation regime, still measured for ventilated cavities? [70]

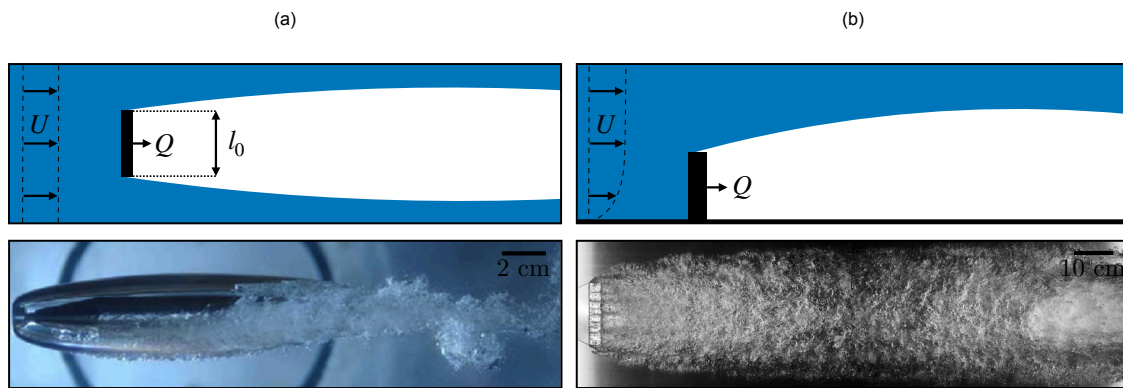


Figure 4.1: Common set-up for the study of ventilated cavity. (a) Top panel: scheme of the axisymmetric cavity set-up. An axisymmetric body of diameter l_0 is placed in a flow of water of velocity U and air is injected at its back at a volumetric rate Q . Bottom panel: picture of the cavity experimentally obtained taken from [71]. The disk is on the left-hand side of the picture and the flow is going from the left to the right. (b) Top panel: sectional drawing of the 2D cavity set-up. A fence is placed on a wall of a hydraulic tunnel and air is injected in its wake at a rate Q . Bottom panel: top view picture of the cavity experimentally obtained taken from [72]. Fence is on the left-hand side of the picture and the flow is going from the left to the right.

Even though most applications are military and concern torpedo optimisation [73, 74, 75], ventilated cavities can also reach commercial marine transportation through the improvement of hydrofoils [76, 77, 78, 79] and the drag reduction on hulls [80, 81].

As a consequence of these applications, ventilated cavities have mainly been studied in the two different configurations presented in figure 4.1. The first one, sketched in the top panel of figure 4.1(a) is an axisymmetric body (usually a disk or a wedge) of diameter l_0 , placed in a water stream of velocity U , with air injected in its near wake at a volumetric rate Q . This set-up results in the development of a nearly axisymmetric cavity pinned at the rim of the body as shown in the picture in the bottom panel of figure 4.1(a), taken from [71]. This set-up typically models projectiles and torpedoes. The second one, drawn in the top panel of figure 4.1(b), consists of a small fence placed on a wall submerged into a flow of water. When air is injected behind the fence, a nearly 2D cavity grows in the wake of the fence as shown in the picture presented in the bottom panel of figure 4.1(b), taken from [72]. This mimics the cavity that would form on the hull of a boat.

In this chapter, we concentrate on ventilated cavities in the wake of projectiles and briefly review the literature on the topic.

4.2 Ventilated cavities in the wake of projectiles

4.2.1 Dimensional analysis

In order to determine the key parameters of the problem, we first carry out its dimensional analysis. The $p = 9$ physical variables of the problem are the following: the diameter of the body l_0 , the length of the bubble l , the flow velocity U , the air injection volumetric rate Q , the fluid density ρ , its dynamic viscosity η , the drag of the system D , the gravitational constant g and the variation of pressure across the interface of the bubble Δp . These 9 variables relies on $k = 3$ dimensions, namely length, time and mass. According to the Buckingham π -theorem, we can construct $p = n - k = 6$ dimensionless numbers for this problem. Denoting $S = \pi l_0^2/4$ the frontal area of the sphere, we obtain the following six dimensionless number:

$$\left\{ \begin{array}{l} \pi_1 = \frac{l}{l_0} \\ \pi_2 = \frac{Q}{SU} \\ \pi_3 = \frac{D}{1/2\rho SU^2} = C_D \\ \pi_4 = \frac{l_0 U \rho}{\eta} = Re \\ \pi_5 = \frac{U}{\sqrt{gl}} = Fr \\ \pi_6 = \frac{\Delta p}{1/2\rho U^2} = \sigma_c \end{array} \right. \quad (4.1)$$

π_1 is the dimensionless size of the bubble. π_2 is the the dimensionless volumetric injection rate. It can also be seen as the comparison between the flow velocity U and the characteristic velocity of the air in the bubble Q/S . π_3 is the drag coefficient C_D of the ventilated object. π_4 is the Reynolds number which compares the inertial effects to the viscous effects in the outer flow. π_5 is the Froude number based on the size of the bubble and is the ratio between the inertial effects to the gravitational effects in the flow. π_6 is the relative underpressure of the cavity σ_c and is the ventilated cavities equivalent of the cavitation number σ .

We now discuss how these different parameters have been investigated in the literature.

4.2.2 Length of the cavity and shedding process

The length of the cavity depends on the relative underpressure σ_c as plotted for two-dimensional wedge (prism with an isosceles triangle as base) in figure 4.2(a) taken from [7]. This plot shows that, similarly as for cavitating object, for all flow velocities, decreasing the relative underpressure σ_c of the cavity, creates longer bubbles (*i.e.* l/l_0 increases). It also suggests that the dimensionless size of the bubble follows a law of the form $\frac{l}{l_0} \sim \sigma_c^{-\alpha}$. To rationalize this dependency one has to recall that the length of the cavity l is set by an equilibrium between the air injected at a flow rate Q and the air shed at the trailing edge of the bubble at a rate Q_{out} . In the steady state, we have:

$$Q = Q_{out}(l/l_0, Q/SU, Fr, Re, \sigma_c, C_D) \quad (4.2)$$

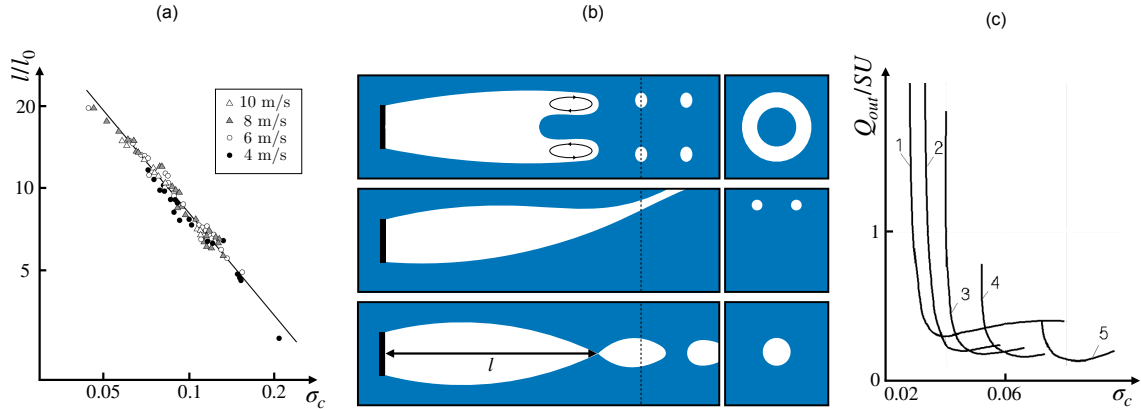


Figure 4.2: (a) Dimensionless size of the bubble l/l_0 as a function of the relative underpressure σ_c for a two-dimensional wedge (prism with an isosceles triangle as base). Velocity is varied from 4 to 10 m/s. Figure taken from [7]. (b) Sketches of the three different shedding processes for an axisymmetric cavity of length l . Left: Sectional drawing along the streamwise direction. Right: Sectional drawing in the cross-stream direction (along the dashed line). From top to bottom: shedding by toroidal vortices, shedding by hollow vortex tubes and shedding by pulsating cavities. (c) Dependency of the steady state shedding rate Q_{out}/SU on the relative underpressure σ_c in the hollow vortex tube regime. Froude number based on the length of the cavity is varied "1" $Fr = 19.3$, "2" $Fr = 16.5$, "3" $Fr = 14.6$, "4" $Fr = 12.7$, "5" $Fr = 11$. Figure taken from [82].

As a consequence, many studies have focused on the understanding of the shedding mechanism. Three major shedding processes have emerged and we briefly describe them. For a thorough review, the reader is referred to [7].

- For small cavities, gravity can be neglected. This is typically the case for $\sigma_c^{3/2} Fr^2 > 10$ [83]. In this regime, the cavity is axisymmetric and shed toroidal vortices as shown in the top sectional drawings of figure 4.2(b), the shedding rate can be evaluated semi-empirically and only depends on U and σ_c [84].
- For large cavities, the back of the bubble is deformed by gravity and the shedding happens via two vortex tubes as presented in the middle sectional drawings of figure 4.2(b). This regime is observed for $\sigma_c^{3/2} Fr^2 > 1.5$ [83]. In this case, the Froude number based on the cavity length is an additional parameter to consider for evaluating the shedding rate. As the regime of large cavities is relevant for the study of supercavitation, it was thoroughly studied in the literature [85, 86]. However, as supercavitating projectiles travels at higher Froude numbers, the gravity effects restrict the similarity of the two systems.
- For large injection rate Q , the cavity is axisymmetric and is observed to be pulsating: it periodically shed bubbles at its trailing edge. This regime is sketched at the bottom of figure 4.2(b). In this regime, the shedding rate is found to depend on the ratio σ_c/σ , where $\sigma = \frac{p - P_{vap}}{1/2\rho U^2}$ is the natural cavitation number [87].

From such mechanisms, the air entrainment rate Q_{out} can be obtained. In the hollow vortex tube regime, this dependency is shown for several Froude number in figure 4.2(c) taken from [82]. For all Froude numbers, entrainment rate is mainly decreasing with the relative

underpressure: large cavities tends to shed greater amount of air. Increasing the Froude number shifts the curves towards lower underpressure σ_c .

4.2.3 Influence of the blockage ratio

Unlike in the unbounded flow configuration, increasing the size of the ventilated cavity in the cross-stream direction in a wall-bounded flow changes the pressure distribution in the surrounding water. As a consequence, the dimensions of the created cavity are expected to depend on the geometry of the test-section. The blockage ratio $\mathcal{B} = W/l_0$, defined as the ratio of the width of the tunnel W to the diameter of the object l_0 , has been identified as the parameter [88] which drives the influence of the wall on the bubble.

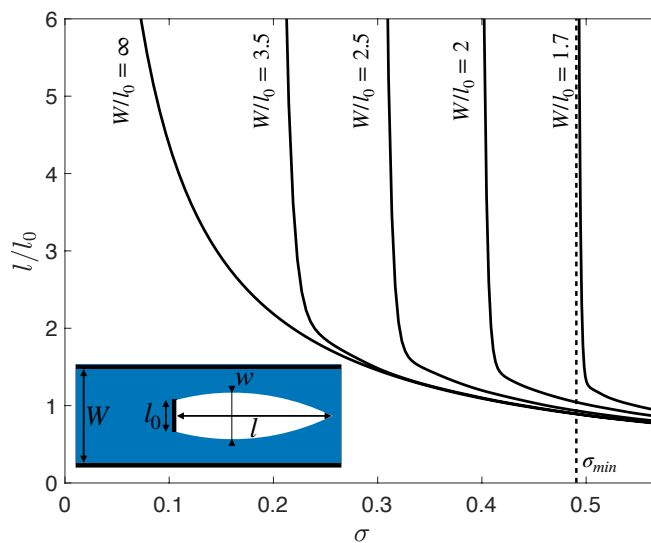


Figure 4.3: Numerical simulations of the dimensionless length of the cavity l/l_0 as a function of the cavitation number σ for different blockage ratio $\mathcal{B} = W/l_0$ (see inset). Figure adapted from [6].

For natural cavitation experiments, figure 4.3, adapted from [6], presents results of numerical simulations of the length of the bubble as a function of the cavitation number σ for different blockage ratio. We first recover the tendency previously observed: for all blockage ratios, decreasing the cavitation number σ results in the elongation of the cavities (l/l_0 increases). Similarly, it was also shown [88] that the maximal width w of the cavity also increases when σ is reduced. However, the flow is choked when the cavity is too large, resulting in a minimal accessible cavitation number σ_{min} in a bounded tunnel. The value of σ_{min} is decreasing with the blockage ratio \mathcal{B} (it increases from ~ 0.18 for $W/l_0 = 3.5$ to ~ 0.48 for $W/l_0 = 1.7$). As a consequence, the cavities are always longer in bounded tunnels. Even though this effect is limited for short cavities (l/l_0 smaller than ~ 1), it becomes very important when σ approaches σ_{min} : for instance at $\sigma = 0.5$ the cavity in a tunnel with $\mathcal{B} = 1.7$ is six times longer than in an unbounded flow.

4.2.4 Drag reduction: application to spheres

For axisymmetric body, most of the previous studies use wedges as bodies. Firstly because they are good model for bullet, torpedoes or missiles heads. The second reason is that wedges are experimentally easier to manipulate as they create more stable cavities. Finally

and most importantly, using wedges fixes the pinning point of the ventilated cavity and its detachment angle: this constrains two free parameters and makes modelling and numerical simulation possible.

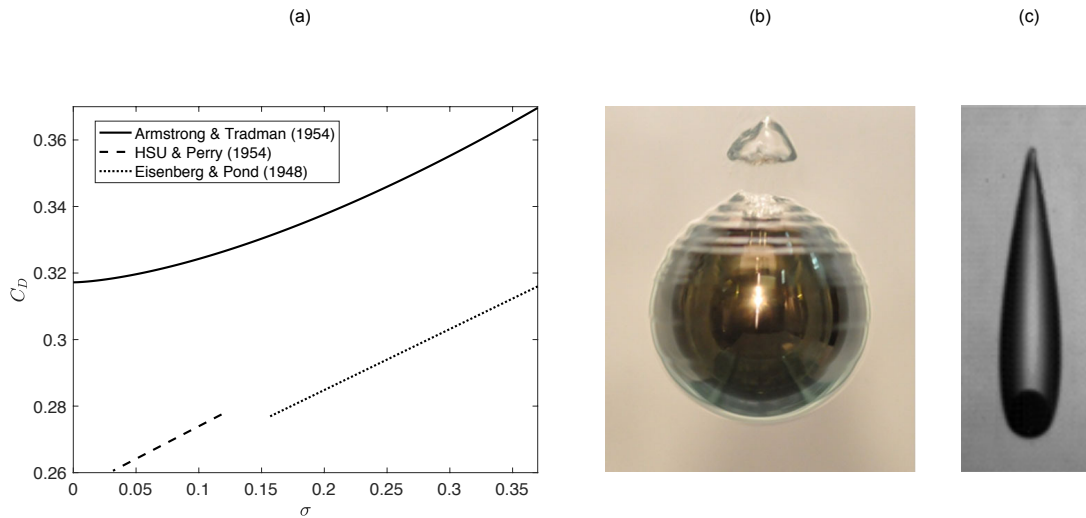


Figure 4.4: (a) Drag coefficient C_D of a sphere as a function of the cavitation number σ . Figure reproduced from [6]. Theoretical work of [89] is plotted in solid line. Mean line for experimental results are drawn in dashed [90] (ventilated cavity) and dotted lines [91] (natural cavitation). (b) Picture of a heated 15 mm steel sphere held stationary in fluorinated liquid with sphere temperature above the Leidenfrost temperature taken from [92]. (c) Picture of a tungsten carbide sphere of diameter 1 cm following the impact at 3.43 m/s on the surface of perfluoro-2-methylpentane (boiling temperature 57°C). Picture taken 90 cm below the surface. Sphere is heated at $\sim 200^\circ\text{C}$. Picture extracted from [93].

To that end, most of the work on ventilated cavities behind spheres or supercavitating spheres focus on the detachment point of the cavity [88, 94, 95]. As a result, even though the hydrodynamic properties of a sphere without air injection are well known and could consist of a firm ground to start the study of ventilated cavities, only few studies report the drag modification induced in that way.

Figure 4.4(a), adapted from [6], gathers some of the experimental and theoretical results on drag coefficients C_D [91, 90, 89] obtained on spheres with a cavity. Solid line is a theoretical result taken from [89]. Dashed line is the mean trend of the experimental results on ventilated cavities behind a sphere taken from [90]. Dotted line is the mean trend for a cavitation sphere [91]. For both theory and experiments, decreasing the cavitation number σ , *i.e.* increasing the size of the cavity, results in a reduction of the drag. However, experimental results are lower than the theoretical predictions, which is assumed to be caused by discrepancies between the theoretical detachment angle and its experimental value. In any cases, when $\sigma \rightarrow 0$, C_D tends to a fix value which ranges from ~ 0.2 (for experimental data) to ~ 0.35 (for theoretical studies). For a Reynolds number between 10^3 to 10^5 , this corresponds to a drag reduction by a factor ~ 2 .

Recent studies have also pointed out another way of creating the vapor: using heated projectile [92, 93, 96]. In such experiments, the spheres are heated up to 400°C , and when in contact with water, they generate an envelop of vapor, similar to the Leidenfrost effect. The envelop can be a thin film (figure 4.4(b)) or even a stable streamlined cavity (figure 4.4(c)) when formed after the impact at the water surface. For the case of a thin film, the minimum drag coefficient measured is 0.1 (corresponding to a reduction by a factor 5 at

$Re \sim 10^5$) [92] while the drag coefficient can be as low as 0.05 (corresponding to a reduction by a factor 10 at $Re \sim 10^5$) in the regime of a stable streamlined cavity [93].

4.3 Statement of the problem

It appears that one of the dimensionless parameters introduced in the dimensional analysis, namely the Reynolds number Re deserves to be thoroughly studied.

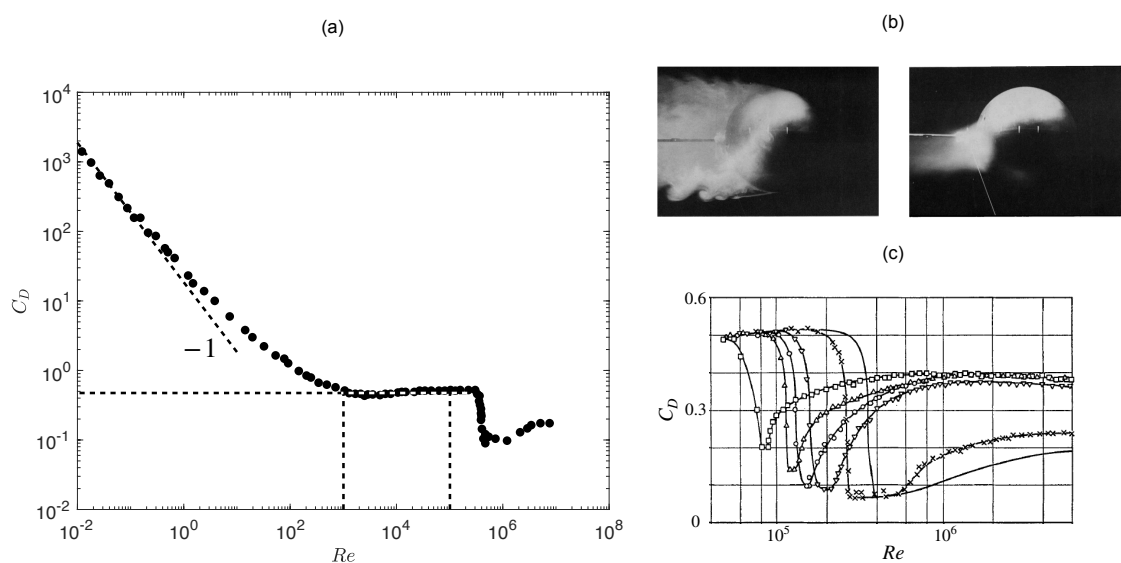


Figure 4.5: (a) Experimental measurements of the drag coefficient C_D of a non-cavitating sphere as a function of the Reynolds number Re . Figure reproduced from [1]. The drag crisis corresponds to the sudden diminution of drag observed between $Re = 10^5$ and $Re = 10^6$. (b) Picture of smoke visualizations of the near wake of a sphere taken from [97]. Air flow is coming from the right. Left panel: sub-critical regime for $Re = 2.3 \times 10^4$. Right panel: super-critical regime for $Re = 5.8 \times 10^5$. (c) Drag coefficient C_D in the drag crisis as a function of the Reynolds number Re for different roughness of spheres. Figure taken from [98]. Solid line is a smooth sphere. Roughness is defined as the ratio of the size of surface defects to the diameter of the sphere and is varied from 2.5×10^{-4} (crosses) to 1.2×10^{-1} (squares).

Indeed, the Reynolds number controls the morphology of the flow around the body and in its wake. For the extensive literature on the subject, sphere appears as the natural body to study the influence of the Reynolds number. Indeed, its influence on the drag coefficient of a sphere is well-known and is presented in figure 4.5(a). This curve has been thoroughly described in the introduction. However, let us recall that between $Re \approx 10^3$ and $Re \approx 10^5$, the drag is dominated by inertial effects, C_D is constant and has a value around 0.5. Around $Re \approx 3 \times 10^5$, the drag coefficient drops to 0.1: this is called the drag crisis. The drag crisis corresponds to important changes in the flow in the boundary layer and in the wake of the projectile. Figure 4.5(b) displays smoke pictures of the wake before (left) and after the crisis (right). In the sub-critical regime, the boundary layer detaches near the equatorial plane of the sphere, the wake is large and presents characteristic vortices structures. In the super-critical regime, the boundary layer detaches near the trailing edge of the projectile and the wake is thin and tilted with the flow. The drag crisis can appear at lower Reynolds numbers with rough spheres as shown in figure 4.5(c). Additionally, the drag reduction

previously reported for Leidenfrost spheres enveloped with a thin layer of vapor [92, 96] has been attributed to an early trigger of the drag crisis.

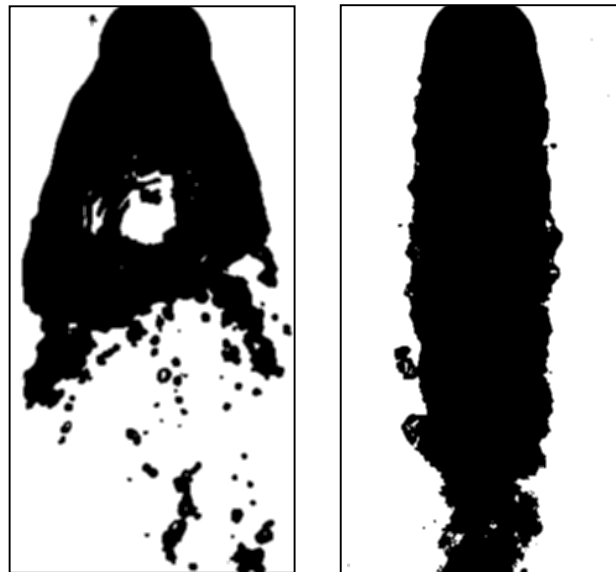
Most applications of ventilated cavities are underwater fast moving object (typically torpedoes). They are in a regime for which gravity is negligible and the flow super-critical. However, ventilated cavities have only been studied for Reynolds numbers between 10^3 and 10^5 . Given the differences in the flow and in the origin of the drag depending the Reynolds number, it appears crucial to investigate ventilated cavity flow in a broader range of Reynolds number.

As a consequence, the rest of the study will concentrate on ventilated cavities behind spheres in the range of Reynolds number of the drag crisis. The study will be carried out in a regime for which the gravity is negligible. The ventilation will be controlled via the dimensionless volumetric injection rate Q/SU .

5

EXPERIMENTAL SET-UP

The set-up presented in this chapter is used to study ventilated cavities behind spheres. It is the result of almost two year of preparation. Thierry Pichon, Caroline Frot and Romain Labbé greatly contributed to the improvement of the initial design. Magali Tutou and Delphine L'Huillier spent hours negotiating with a company under liquidation to have our orders delivered. Finally, it took us almost a month, along with Juliette Amauger to erect the complete structure. Needless to precise that the whole process was carefully (or maybe anxiously) followed by Christophe Clanet and Caroline Cohen.



Two illustrations of the ventilated cavities behind a sphere that can be obtained with the experimental set-up presented in this chapter.

Contents

5.1	Hydraulic tunnel construction	56
5.2	Flow in the empty test-section	56
5.3	Drag measurements	57

5.1 Hydraulic tunnel construction

The experimental set-up used to study ventilated cavities is an hydraulic tunnel with a vertical test section sketched in figure 5.1. The flow of water is driven by a pump (Grundfos, (1)) with tunable flow rate from 50 to 270 cubic meters per hour. Pumped water passes through a valve (2) and is poured via a vertical outlet pipe (3) into a three-meters long tranquilization tank (4). At the other end of the tank, the water passes through a honeycomb (with centrimetric holes) and a vertical converging nozzle (5), which reduction ratio is 4 to 1, before entering the test-section (6). The test-section is vertical and has inner dimensions of 11 by 11 by 70 cm. It is made of three centimeters thick transparent acrylic and is equipped with two side windows to change the object tested. An air-injection system (7) allows us to inject, at a control flow rate, air in the test section. Finally, water is fed back into the pump through a return pipe (8). In this study, objects tested are spheres of diameter l_0 varying from 2 to 3 cm. To obtain smooth spheres, half spheres are 3D-printed in Acrylonitrile Butadiene Styrene (ABS), attached together and then smoothed above an acetone bath at 70°C during two minutes. $W = 11$ cm being the width of the tunnel test-section, we define the blockage ratio $\mathcal{B} = W/l_0$ which ranges from 3.5 to 5.5. As presented in figure 4.3, these values should be sufficient to reach equivalent cavitation numbers as low as 0.15.

To measure the drag of tested projectiles (i), they are attached onto two submersible force sensors (iii) with a 3D-printed streamlined holder (ii) as shown in figure 5.1(b). Air is injected at the trailing edge of the projectile (i) through the holder (ii) as drawn in figure 5.1(c). The flow rate is measured using mechanical flow meter (Key Instruments, (7) in figure 5.1) with an accuracy below 5% and can be varied from 0.4 to 20 liters per minute (lpm).

5.2 Flow in the empty test-section

The resulting flow in the test-section can be visualized via Particle Image Velocimetry (PIV). We use the sub-millimetric bubbles entrained in the tunnel as PIV particles. The instantaneous velocity field can be decomposed in a streamwise (vertical) component $-u(t) \mathbf{e}_y$ and an horizontal component $v(t) \mathbf{e}_x$. The typical streamwise velocity u all across the tunnel is plotted in figure 5.2(a) for the pump running at 75 Hz. We note that, apart from the 0.5 cm close to the tunnel walls, the streamwise velocity is fairly homogeneous. Indeed, in the ten central centimeters of the test-section, the velocity only varies between 4.4 and 4.6 m/s, which corresponds to a variation below 5 %. From such measurements, we compute the average velocity in the streamwise direction U in the central part of test section. Figure 5.2(b) displays the typical instantaneous non-dimensional cross-stream velocity v/U . In most of the tunnel, its value is below 1.5 % and it never exceeds 4%. The maximum value is only reached in the right part of the tunnel, which create an asymmetric in the test-section. Although this is satisfactory for our applications, this effect was further reduced by ensuring that the swirling motion induced by the suction in the tranquilization tank is axisymmetric.

With such measurements, we can average the velocity u over the streamwise direction (y -axis) to obtain the mean profile across the tunnel. Doing so for different running frequencies of the pump, we obtain the profiles plotted in figure 5.3(a). All the profiles share the same shape: the velocity u is fairly constant in the central part of the tunnel and rapidly decays in the centimeter near the walls. The maximum velocity of the profile increase with the running frequency of the pump. From this profile, we compute U , the average of u in the

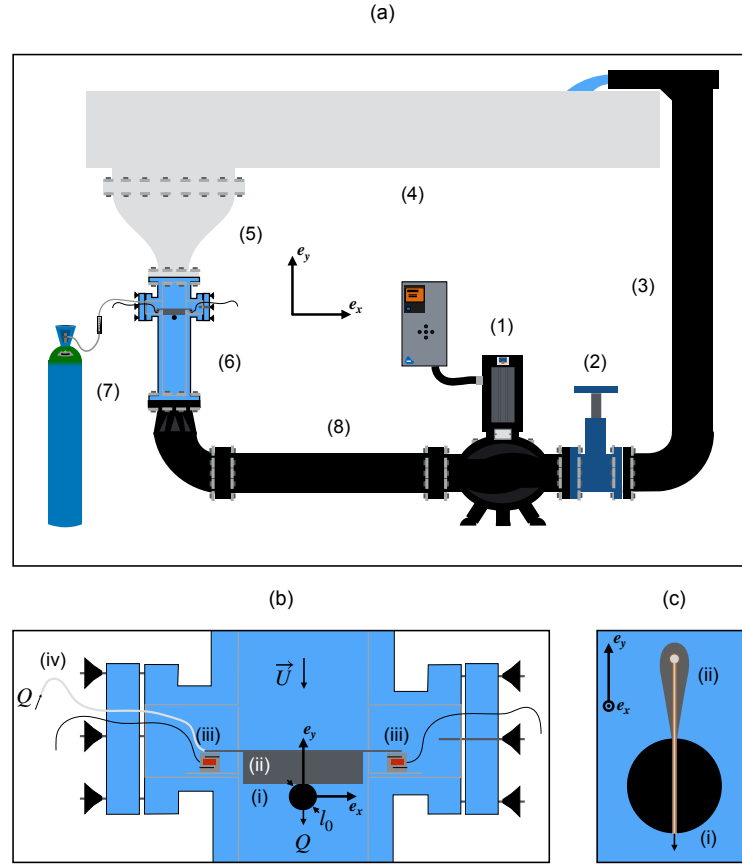


Figure 5.1: (a) Drawing of the hydraulic tunnel used to study ventilated cavities. It is composed of a pump of variable speed (1), a valve (2), a vertical outlet pipe (3), a three-meters long tranquilization tank (4), a converging nozzle (5), a vertical test-section (6), an air injection device (7) and a return pipe (8). (b) Close-up on the test-section of the tunnel. The tested object (i) is attached onto a streamlined holder (ii) which rests on two submersible force sensors (iii). Air is injected at the trailing edge of the projectile through a flexible tubing (iv). (c) Sectional drawing of the projectile (i) and the holder (ii) along the axis Oy . Air is injected at a volumetric rate Q at the back of the projectile.

central part of the tunnel. Figure 5.3(b) shows the evolution U with the running frequency of the pump. In range of accessible frequencies (25 to 100 Hz), U is affine with the pump frequency. We deduce that streamwise velocity in our test-section ranges from 1 to 6 m/s, which leads to a Reynolds Number $Re = \frac{U l_0}{\nu}$ between 10^4 and 2×10^5 .

5.3 Drag measurements

5.3.1 Validation of the measurement set-up

Drag measurements are done with two submersible miniature force sensors (Futek) loaded in compression ((iii) in figure 5.1(b)). The two sensors with their acquisition system were separately calibrated with precision scale. To avoid any perturbation, all drag measurements are averaged over at least 30 seconds. The calibration of the whole drag measurement set-up is checked with a simple cylinder running across the tunnel for Reynolds Number between

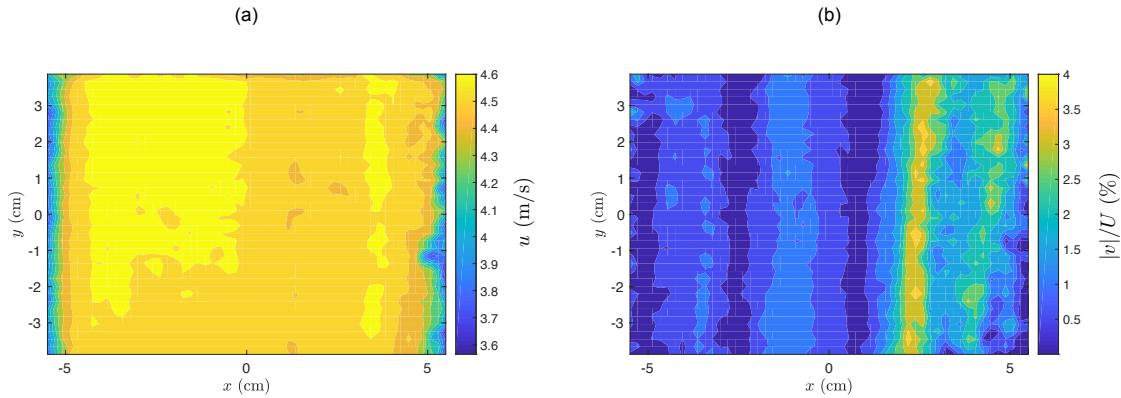


Figure 5.2: Particle Image Velocimetry (PIV) measurements all across the test-section. The origin of the axis is placed at the center of the test section (*i.e.* where the test-object is located). Walls of the tunnel are in $x = \pm 5.5$ cm. Velocity field is decomposed in a streamwise (vertical) component $-u(t) \mathbf{e}_y$ and an horizontal component $v(t) \mathbf{e}_x$. (a) Streamwise component of the flow velocity u all across the tunnel. (b) Non-dimensional cross-stream velocity v/U all across the tunnel where U is the average of u over time in the ten central centimeters of the test-section.

3×10^3 and 4×10^4 . The drag force D is plotted against the velocity of the flow U in figure 5.4(a). As expected in this range of Reynolds numbers, the drag is proportional to U^2 [1]. As a consequence, the drag coefficient based on the frontal area S of the cylinder $C_D = \frac{D}{1/2\rho S U^2}$, is constant equal to ± 1.1 . This value is coherent with what can be found in the literature [1]. Hence, we can effectively measure the drag on a body placed in the test-section of the hydraulic tunnel.

5.3.2 Drag coefficient of a sphere

Taking into account the error in the force measurements, the range of Reynolds numbers accessible in our experimental set-up is 4×10^4 to 2×10^5 . These numbers are below the critical Reynolds number (3×10^5) for which the crisis happens for smooth spheres as previously shown in figure 4.5(a). However, as we wish to study the influence of ventilated cavities in the drag crisis, we use the trick previously presented to trigger the transition earlier: rough sphere are used to carry out the experiments.

Sphere we use for the experiments are 3D printed with a thickness layer of $t \approx 0.1$ mm. After smoothing, the resulting roughness t/l_0 is on the order of $\sim 5 \times 10^{-3}$ for a sphere of diameter 2 cm and on the order of $\sim 3.3 \times 10^{-3}$ for a sphere of diameter 3 cm. As previously stated, we expect that this will induce an early drag crisis (figure 4.5(c) from [98])

Using this experimental set-up, we measure the drag D on a single sphere in the range of accessible Reynolds numbers. The drag can be expressed as follow:

$$D = \frac{1}{2} \rho S C_D U^2 \quad (5.1)$$

where the drag coefficient of the sphere C_D is based on its frontal area ($\pi l_0^2/4$). For the spheres we use, C_D is plotted in figure 5.4(b). For a sphere of diameter 3 cm (black dots), the drag coefficient C_D is ~ 0.5 for a Reynolds number around 6×10^4 , after that, C_D decreases monotonously to reach ~ 0.1 at $Re \sim 2 \times 10^5$. This phenomenon corresponds fairly well to the drag crisis that we described in the previous chapter for an equivalent roughness of 5×10^{-3} (plotted in dashed black line, data taken from [98]). For a sphere of

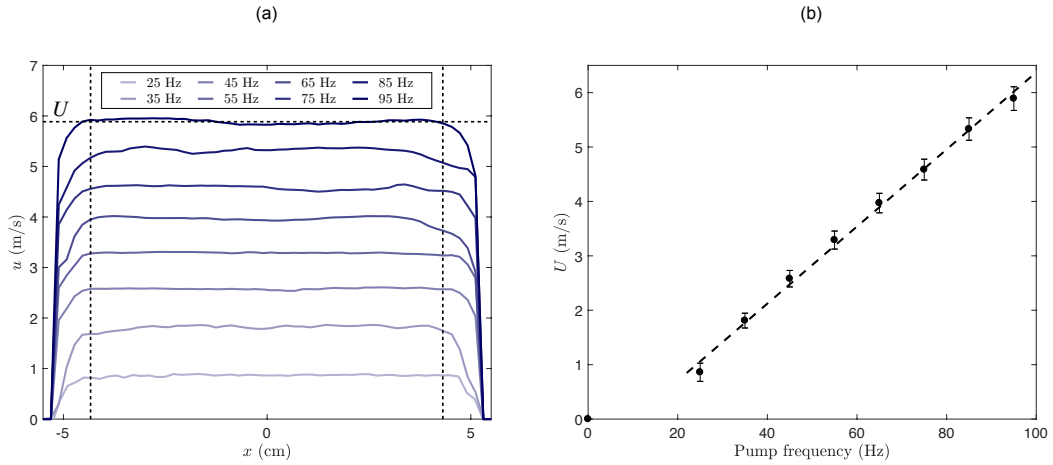


Figure 5.3: (a) Cross-stream profiles of the streamwise velocity u for running frequencies of the pump ranging from 25 Hz to 95 Hz. Walls of the tunnel are located in $x = \pm 5.5$ cm. (b) Average streamwise velocity U in the center part of the the tunnel as a function of the pump frequency. Dotted line is an affine fit in the range of accessible running frequencies (25 to 100 Hz).

diameter 2 cm (red squares), the measurements can be exploited after $Re \sim 6 \times 10^5$. At that point, the drag coefficient is $C_D \sim 0.42$ and then decreases to reach $C_D \sim 0.27$ at $Re \approx 10^5$. After that, the drag increases with the Reynolds number. The equivalent roughness for this crisis, taken from [98], is 1.25×10^{-2} , which is greater than the actual one ($\sim 5 \times 10^{-3}$).

The discrepancies in the predicted roughness and the equivalent one found using [98] are attributed to the fact that the spheres studied are placed downstream the holder. As a consequence, the spheres are in the wake of the streamlined holder resulting in slightly modified drag crisis (mostly shifted towards lower Reynolds numbers) [99]. This effect is more important as the size of the sphere is close to the size of the holder (*i.e.* as the size of the sphere is reduced).

As a consequence, our experimental set-up allows us to reproduce the drag crisis at lower Reynolds number and to measure the drag on the sphere. In the following chapter, we will investigate the influence of the growth of a ventilated cavity in the wake of the sphere on the drag coefficient.

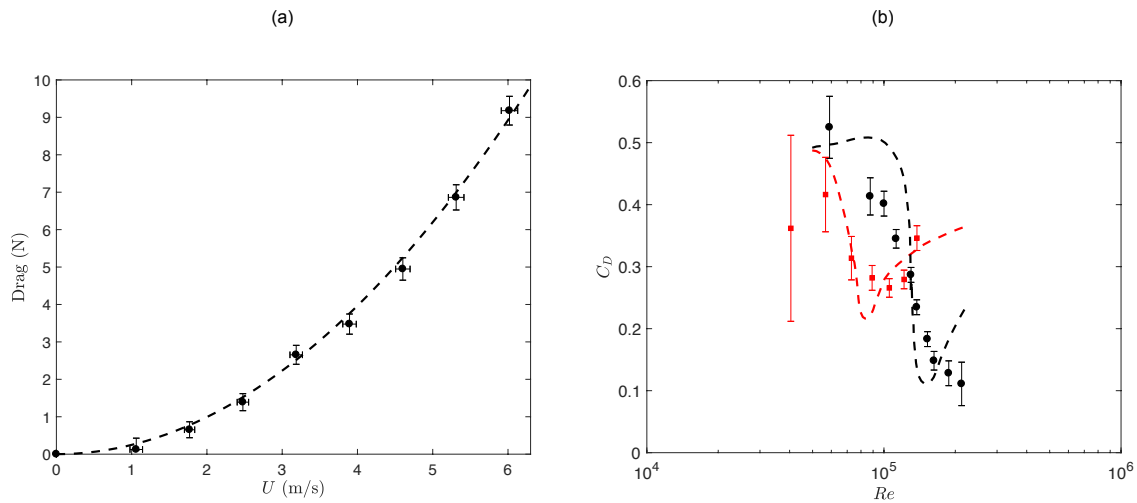
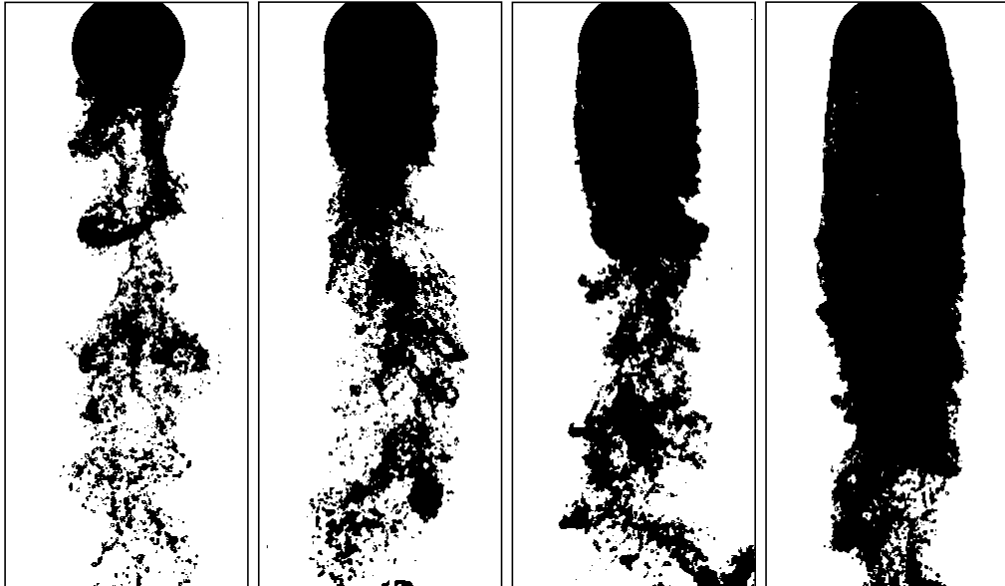


Figure 5.4: (a) Experimental drag of a cylinder of diameter 4 mm and 11 cm long as a function of the mean streamwise velocity U . The dotted line is a fit with a power 2 law. The resulting drag coefficient based on the frontal area S of the cylinder $C_D = \frac{Drag}{1/2\rho S U^2}$ is $C_D = 1.1$. (b) Experimental drag coefficient C_D of a sphere as a function of the Reynolds number Re . Black dot are for a sphere of diameter $l_0 = 3$ cm while red squares are for a sphere of diameter $l_0 = 2$ cm. Dashed line, taken from [98], are the drag crisis measured for roughness ratio of 5×10^{-3} (red) and 1.25×10^{-2} (black).

6

IN-CRISIS DRAG MODIFICATION



Pictures of a sphere with air injected at its back at an increasing rate from the left to the right picture.

Contents

6.1	Morphology of the bubbles	62
6.2	Bubble length	63
6.3	In-crisis force measurements	67

6.1 Morphology of the bubbles

We display in figure 6.1 the different types of bubbles developing in the wake of a projectile, placed in a flow of water at a velocity U , when air is injected at its trailing edge at a constant volumetric rate Q . In all three pictures, the projectile used is a sphere of diameter $l_0 = 3$ cm and the overall structure (object and bubbles) can be decomposed in a stationary part and a dynamic shedding part.

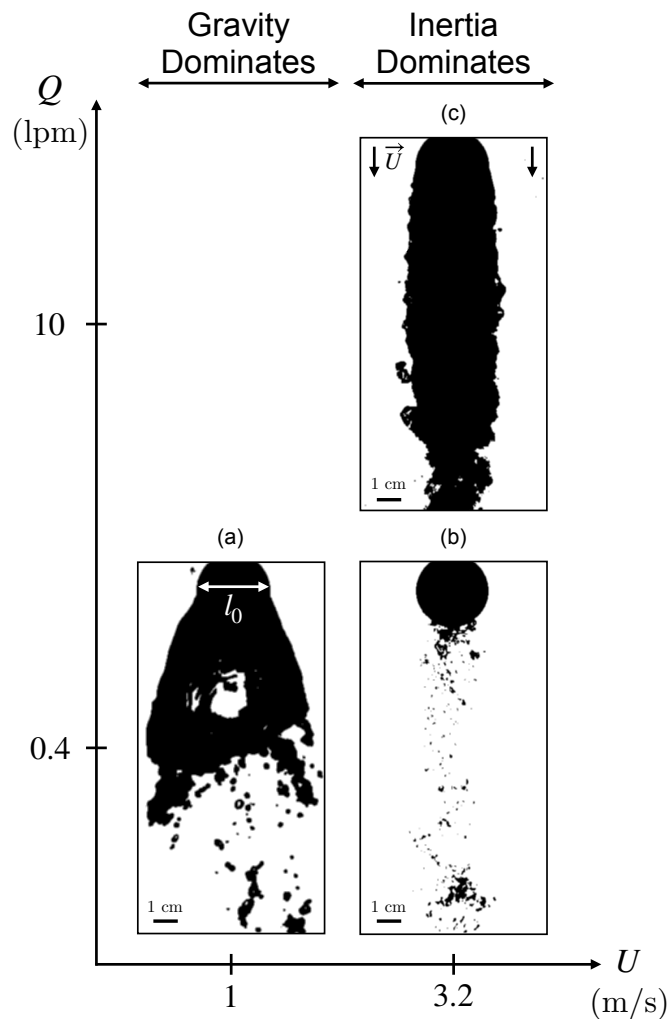


Figure 6.1: Pictures of the structures obtained when injecting air at the back of a sphere, depending on the air injection rate Q and the flow velocity U . Flow is running downward and the sphere of diameter 3 cm is always at the top of the picture. For a flow velocity of 1 m/s and $Q > 2$ lpm, the tunnel is blocked due to the large width of the bubble and stops running.

For flow velocities below 2.5 m/s (figure 6.1(a)), a steady single large bubble attaches to the sphere with injection rates as low as 0.4 lpm. This bubble has an increasing width with the downstream distance from the sphere, up to a diameter of $\sim 2.5 l_0$. At this point, roughly two diameters behind the sphere, the bubble loses its stationary behaviour and millimetric bubbles are shed at the rim of the main structure. For such low flow velocities, bubbles become too large when compared to the tunnel for injection rate greater than ~ 2 lpm: the tunnel is blocked and flow stops.

For high velocity flows $U > 2.5$ m/s (figure 6.1(b)), no steady bubble is observed in the wake

of the sphere. Sub-millimetric bubbles are created at the back of the projectile. Although a few of them remain trapped in the near wake of the sphere (typically a centimeter behind the sphere), most of the bubbles are shed. When the injection rate is increased above ~ 4 lpm (figure 6.1(c)), a stationary bubble attaches to the sphere. The bubble created has a width which hardly varies with the downstream distance: the stationary bubble is close to a cylinder of diameter l_0 . At $Q = 10$ lpm, the shedding occurs approximately $4l_0$ downstream the sphere.

The large bubble observed for low velocities is attributed to the effect of gravity. Indeed, for such velocities, the Froude number Fr , based on the size of the projectile $Fr = \frac{U}{\sqrt{gl_0}}$ is below 5. However, in the high velocity regime where $Fr > 5$, gravity does not affect the shape of the bubbles, even for the largest ones. This confirms that the relevant Froude number, in our experimental set-up, is based on the size of the projectile and not the length of the bubble. The fact that we can neglect gravity for long bubble is a major improvement compared to previous studies, as gravity was setting the limit of the largest bubbles, and this was made possible by the use of a vertical test-section.

For the rest of the study, we will remain in the regime for which gravity is negligible, that is to say, for $Fr > 5$.

6.2 Bubble length

6.2.1 Bubble length measurements

Pictures of the evolution of the bubbles behind the sphere for increasing values of the injection rate Q are gathered in figure 6.2 (a) for a flow velocity U of 3.2 m/s. As previously noticed, for $Q < 4$ lpm, no bubble attaches to the sphere and only sub-millimetric bubbles are created. Thanks to those bubbles, we observe that the characteristic patterns of vortex shedding behind a sphere are still present when air injection is weak. We also notice that the amount of bubbles trapped in the near wake of the sphere increases with Q : bubbles travel further upstream along the surface of the sphere. At $Q \approx 4$ lpm, the trapped bubbles reach the equatorial plane of the sphere. From that point, a large steady bubble pins at the equatorial plane of the sphere and grows when increasing Q . As a consequence, the characteristic vortex shedding also fades away. The resulting stationary bubble has a shape close to a cylinder of diameter l_0 and of characteristic streamwise length l growing with Q .

This length l is precisely defined as shown in figure 6.2(b). In the fully developed bubble regime, we detect the instantaneous bubble boundary as shown in the left panel of figure 6.2(b). We average 1000 images taken over a second to obtain the mean shape of the bubble drawn in black in the right panel of figure 6.2(b). The mean boundary of the bubble is pinned very close to the equatorial plane of the sphere: its initial diameter is close to $l_0 = 3$ cm. As we follow the boundary in the streamwise direction y , the bubble gets larger and reaches a maximal diameter of $w \sim 4$ cm at $y \sim 7$ cm downstream from the equatorial plane. Beyond that point, the bubble becomes thinner until pinches $y \sim 14$ cm. After that, the width becomes roughly constant and independent of y . This part is identified in the pictures 6.2(a) as the wake of the projectile. The length l of the projectile and its bubble is evaluated from its leading edge to its wake. Using this definition of the length of the bubble, we measure it for this set of experiments and we plot its evolution as a function of the air injection rate Q in figure 6.2(c). This confirms the initial observation that the characteristic length of the bubble increases monotonously with Q . Moreover, for $Q > 4$ lpm, l/l_0 follows a close-to-affine trend. Similarly, we measure the maximal width w of the cavity and plot

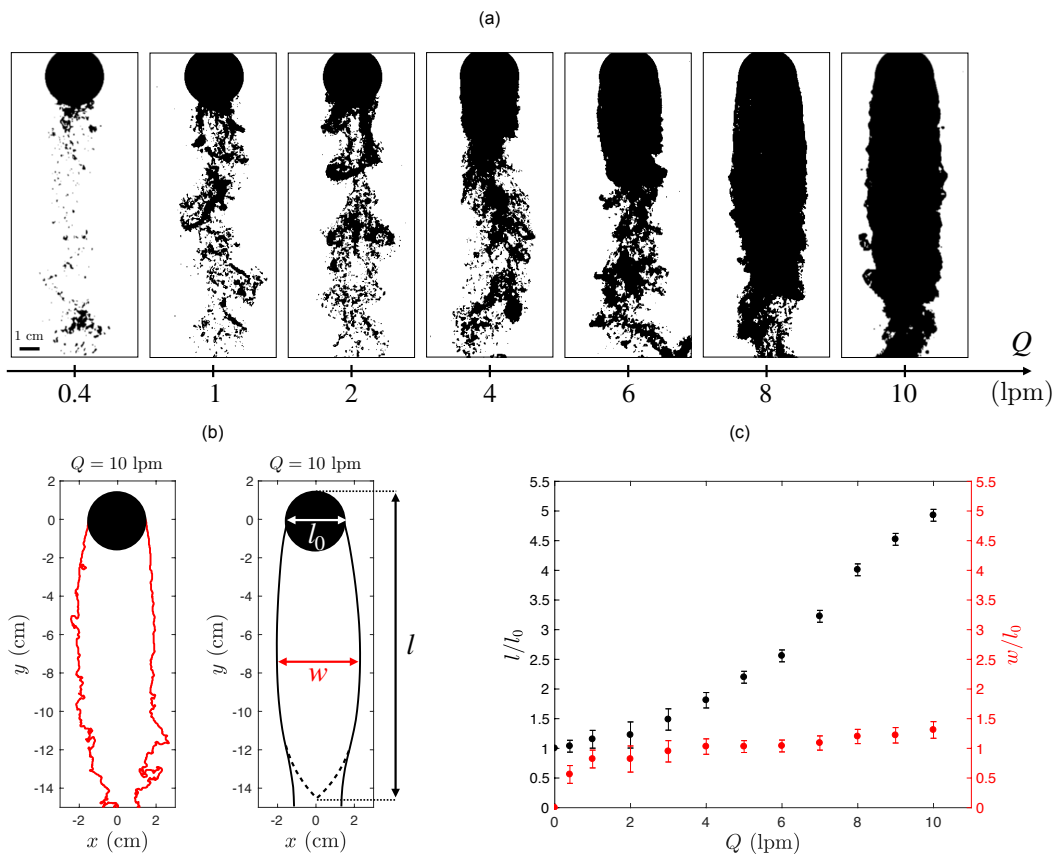


Figure 6.2: (a) Pictures of a sphere with an air injection at the back of the sphere when the air injection Q is varied from 0.4 to 10 lpm. The water flow is going downward at a velocity kept constant at $U = 3.2$ m/s. The sphere has a diameter of $l_0 = 3$ cm and is always located at the top the image. (b) Determination of the characteristic size l of the bubble for a flow velocity of 3.2 m/s. When the cavity is fully developed, its boundary can be detected. The typical instantaneous bubble boundary is plotted in red in the left panel. Origin of the axis is set at the center of the sphere. This boundary is then averaged over 1000 frames taken over 1 second to obtain the mean boundary. This resulting profile is drawn in black in the right panel. The width w and the length l are determined using this profile. (c) Dimensionless length of the bubble l/l_0 (black) and width w/l_0 as a function of the volumetric air flow rate Q for $U = 3.2$ m/s.

it in red in figure 6.2(c): when a bubble is pinned at the equatorial plane of the sphere, the width is roughly constant and equals ~ 1 . The overall cavity is close to a cylinder of diameter l_0 and length l .

After varying the flow velocity and the size of the sphere, we measure the ratio l/l_0 and plot the results in figure 6.3(a). Although the sets of data are spread apart, similar trends are observed in all data sets: the length of the bubble increases with Q . In the range of parameters accessible in our experimental set-up, the longest bubbles reach $l/l_0 \sim 9.5$. Furthermore, we observe that at a constant air injection rate Q , either increasing the flow velocity U or using a larger sphere (increasing l_0) decreases the length of the bubble.

A first approach to rationalize these observations is obtained by using the results of the dimensional analysis previously carried out. Among the 6 dimensionless parameters, the dimensionless size of the bubble l/l_0 and the dimensionless injection rate Q/SU , where $S = \pi l_0^2/4$ denotes the frontal area of the sphere, are the more relevant for this part of the study. We thus plot in figure 6.3(b), the reduced length l/l_0 as a function of the dimensionless

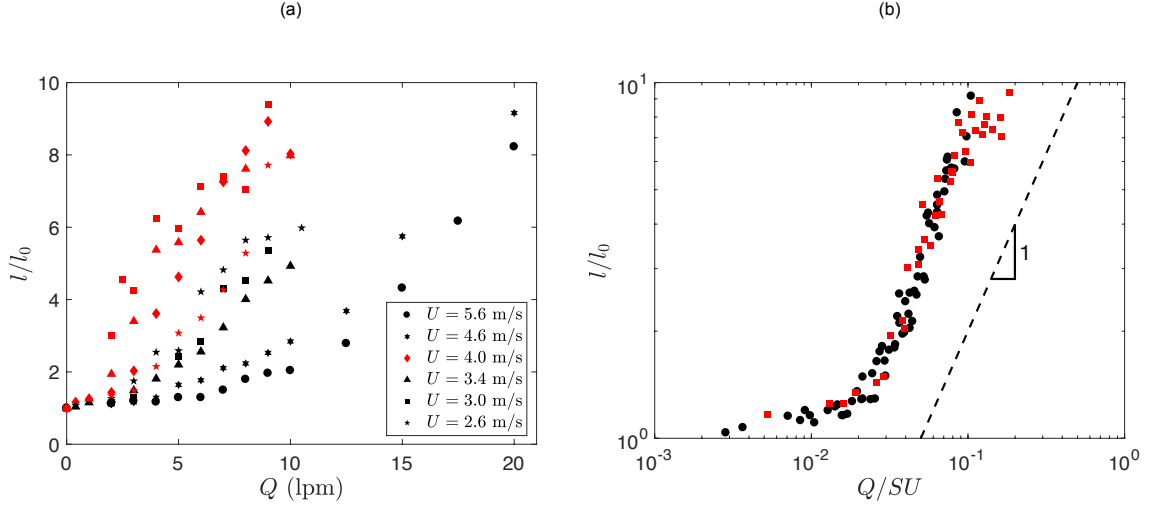


Figure 6.3: (a) Dimensionless length of the bubble l/l_0 as a function of the volumetric air injection rate Q . Black markers are for a sphere of diameter $l_0 = 3$ cm while $l_0 = 2$ cm for the red markers. Velocity of the incoming flow is varied from 2.6 to 5.6 m/s and is represented by the marker shape. (b) Dimensionless length of the bubble l/l_0 as a function of the dimensionless injection rate Q/SU . Black dots are for $l_0 = 3$ cm and red squares for $l_0 = 2$ cm. The dashed line has a slope 1 and is plotted as a visual guide.

air injection rate Q/SU . All the sets of data align in a master-curve composed of two regimes. For Q/SU greater than ~ 0.02 we measure $l/l_0 \propto Q/SU$ which corresponds to the fully developed cavity regime. Below that, the bubble wake is small ($l/l_0 \sim 1$) and weakly increasing with Q/SU .

6.2.2 Surface instability properties

In the steady state, let us recall that incompressibility of the cavity implies:

$$Q = Q_{out} \quad (6.1)$$

where Q_{out} denotes the volumetric rate at which air is shed at the trailing edge of the bubble. In order to determine the dependency of Q_{out} on the parameters of the problem, we first visualize the typical shedding process shown in the post-treatment chronophotography in figure 6.4(a). We observe that the instantaneous bubble boundary (drawn in red) deviates from the mean boundary (drawn in black) near the pinning point at $t = 0$ ms. While this initial perturbation, on the order of ~ 2 mm large, travels along the interface in the streamwise direction, it grows in the cross-stream direction, until it reaches the end of the stationary bubble at $t \approx 18$ ms. At this point, the perturbation is roughly ~ 1 cm large, and it is then shed in the wake of the projectile. The consequence of this shedding process through the growth of instabilities at the interface is that, if we write Ω_i the characteristic volume of air advected by the instability and f_i its shedding frequency, we have:

$$Q_{out} = \Omega_i f_i \quad (6.2)$$

As drawn in figure 6.4(b), the mean profile of the bubble is close to a cylinder of diameter l_0 . Hence, the volume of the unstable perturbation at the shedding point can be approximated as:

$$\Omega_i \approx \pi l_0 \lambda_i \delta x(l) \quad (6.3)$$

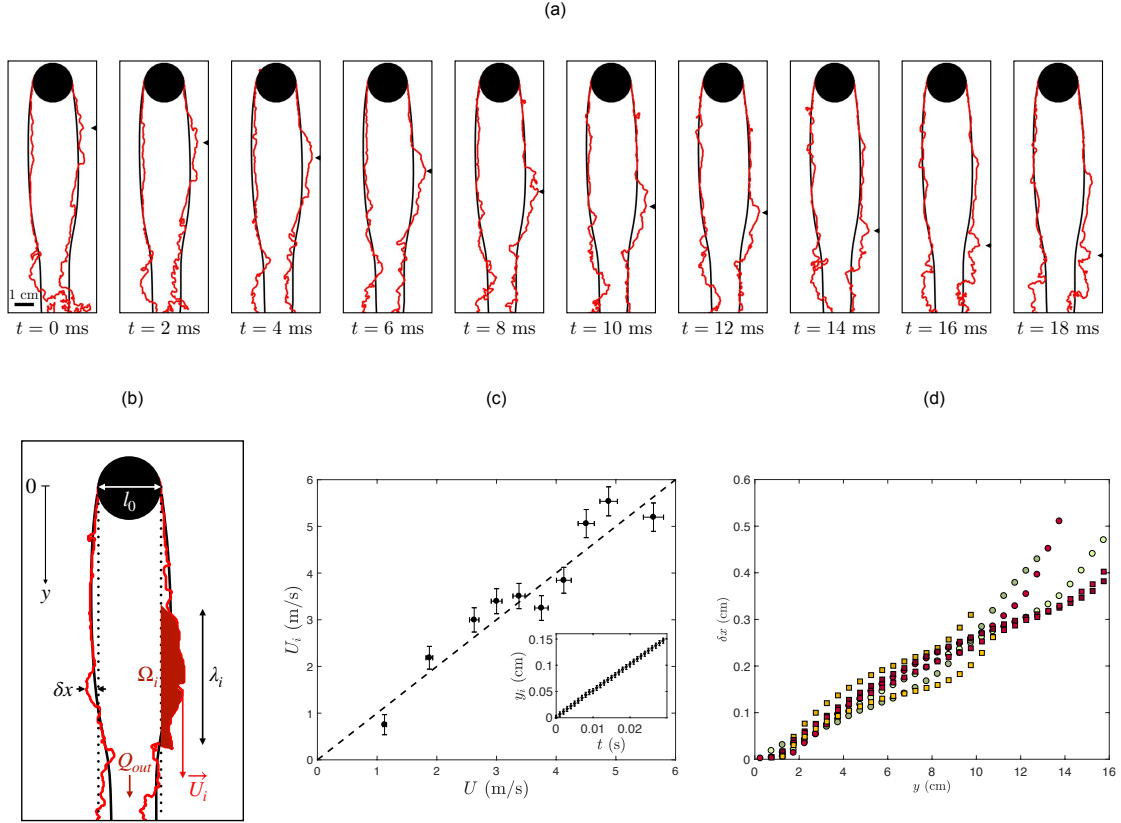


Figure 6.4: (a) Post-treatment chronophotography of a sphere in a downward water flow with air injected at its back. Picture are separated by two milliseconds. The sphere has a diameter $l_0 = 3$ cm, the flow velocity is $U = 3.2$ m/s and the air injection rate is $Q = 10$ lpm. The instantaneous bubble interface is plotted in red while the mean bubble profile is drawn in black. A perturbation is tracked down the interface profile and indicated with a triangular black marker. (b) Sketch of a sphere of diameter l_0 in a water flow with an air bubble pinned at its equatorial plan. Typical instantaneous bubble interface is drawn in red and the mean profile in black. The flow is aligned with the y -axis, which origin is set at the equatorial plane of the sphere. Air is shed at the trailing edge of the bubble at a rate Q_{out} . δx is the standard deviation of the instantaneous profile. The instability growing at the interface has a typical wavelength λ_i and embraces a volume Ω_i of air. (c) Streamwise velocity U_i of an instability on the interface of the bubble as a function of the flow velocity U . Dotted line is the line $U_i = U$. Velocity U_i is extracted from the typical time evolution of the vertical location y_i of the perturbation plotted in the inset. (d) Standard deviation δx of the width of the instantaneous bubble as a function of the distance from the equatorial plane y . Dots are for a sphere of diameter 3 cm. Squares are for a sphere of diameter 2 cm. Yellow is for an air injection rate $Q = 5$ lpm, red is for $Q = 10$ lpm and green for $Q = 15$ lpm. Velocity is varied from 3.2 (light colors) to 5.6 m/s (dark colors).

where λ_i is the typical wavelength of the instability and $\delta x(l)$ its amplitude at the shedding point ($y = l$). Introducing U_i , the instability velocity of the perturbation in the streamwise direction, we can write:

$$f_i \approx \frac{U_i}{\lambda_i} \quad (6.4)$$

Finally, substituting relations (6.3) and (6.4) in equation (6.2) yields:

$$Q_{out} \approx \pi l_0 \delta x(l) U_i \quad (6.5)$$

where U_i and δx_i remain to be determined.

A characteristic feature on the instability can easily be tracked over its motion on the interface of the bubble. A typical time evolution of the streamwise position y_i of the perturbation is plotted in the inset of figure 6.4(c). This evolution is linear and we can extract from it the velocity of the perturbation U_i . Doing so for various flow velocities, we plot U_i as a function of U in figure 6.4(c). We observe a linear trend for U_i , very close to the line $U_i = U$ (dashed line). As a consequence, the instabilities are advected with flow and we deduce:

$$U_i \approx U \quad (6.6)$$

δx can be approximated as the standard deviation of the width of the instantaneous bubble interface. Using this definition, we average $\delta x(y)$ of the two sides of the bubble and plot it in figure 6.4(d) as a function of the distance y from the equatorial plane of the sphere. After varying the size of the sphere, the flow velocity and the injection rate, we note that, for each data set, a linear trend for δx . Additionally, the slope of δx is independent of all the parameters. From these observations, we can write:

$$\delta x(l) \sim l \quad (6.7)$$

Hence, equation (6.5) can be rewritten using the two heuristic relations (6.6) and (6.7):

$$Q_{out} \sim l l_0 U \quad (6.8)$$

Finally, introducing $S = \pi l_0^2/4$ the frontal area of the sphere and using the steady state condition (equation (6.1)), we can express the dimensionless length of the bubble to find:

$$\frac{l}{l_0} \sim \frac{Q}{S U} \quad (6.9)$$

which captures in a satisfactory way the behaviour observed in figure 6.3(b).

6.3 In-crisis force measurements

Ultimately, the goal of the injecting air is to reduce the drag on the sphere. To see the influence of the air injection on the drag, we now concentrate on the measurements of forces.

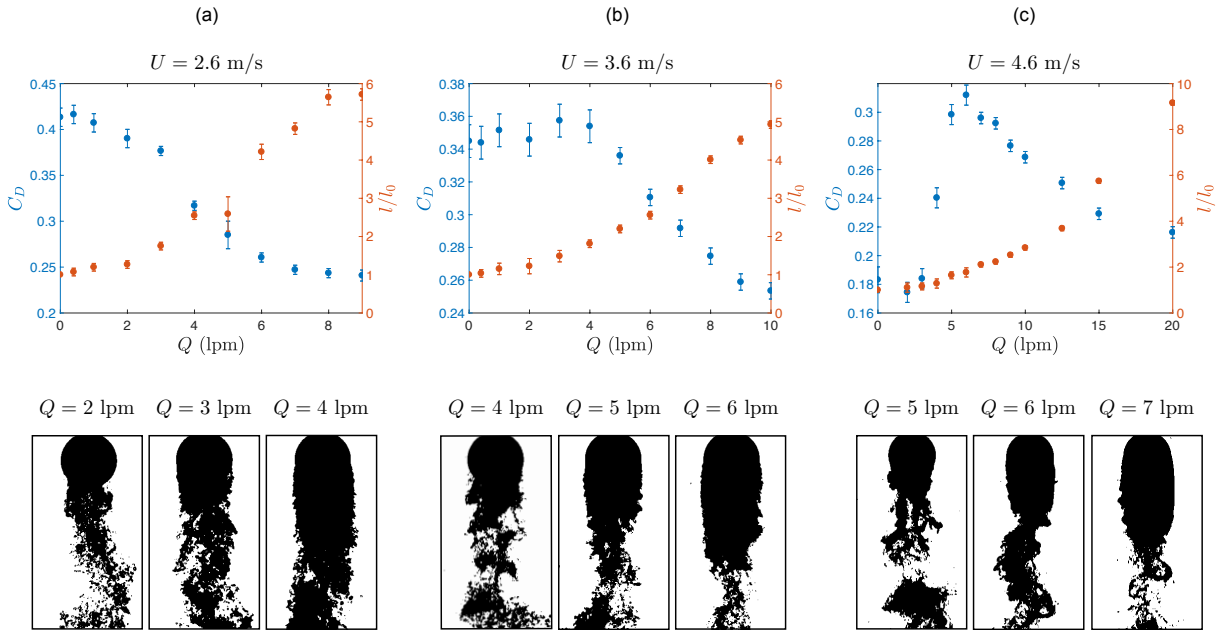


Figure 6.5: Top panel: simultaneous measurements of the drag coefficient C_D (blue) of the sphere with air injection at a volumetric rate Q at its back and of the dimensionless size of the bubble l/l_0 (red). Bottom panel: typical picture of the global structure composed of the sphere and its bubbles wake for selected air injection rates between 2 and 7 lpm. (a) For a flow velocity of 2.6 m/s, *i.e.* $Re \approx 8 \times 10^4$. (b) For a flow velocity of 3.6 m/s, *i.e.* $Re \approx 10^5$. (c) For a flow velocity of 4.6 m/s, *i.e.* $Re \approx 1.5 \times 10^5$.

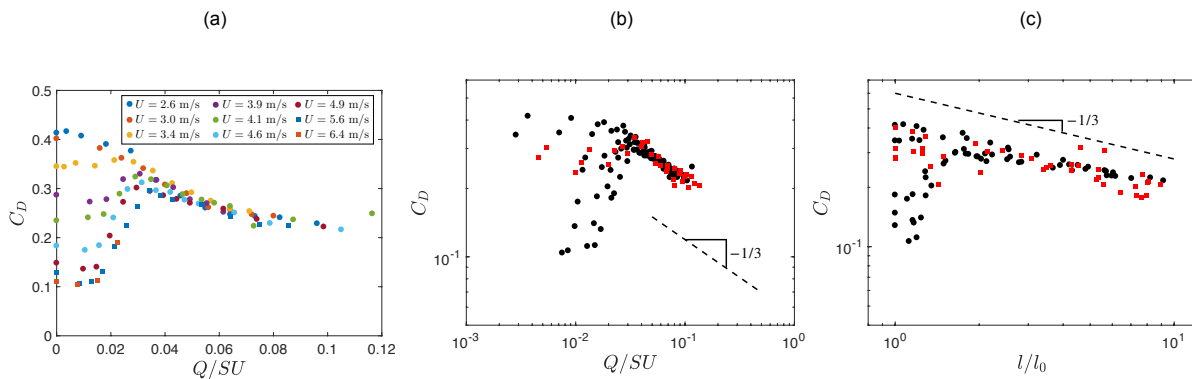


Figure 6.6: (a) Drag coefficient C_D of a sphere of diameter 3 cm as a function of the dimensionless air injection rate Q/SU . Measurements are presented for 9 different flow velocities ranging from 2.6 to 6.4 m/s. (b) Drag coefficient C_D as a function of the dimensionless injection rate. Red squares are for a sphere of diameter 2 cm and black dots for a diameter of 3 cm. Dashed line is a line of slope $-1/3$ and is plotted as a visual guide. (c) Drag coefficient C_D as a function of the dimensionless length of the bubble l/l_0 . Red squares are for a sphere of diameter 2 cm and black dots for a diameter of 3 cm. Dashed line is a line of slope $-1/3$ and is plotted as a visual guide.

6.3.1 Drag of a sphere with air injection at its back

6.3.2 Drag modification

Once again, based on the dimensional analysis previously carried out, the dimensionless injection rate Q/SU should be introduced as a relevant parameter in this problem. For a sphere of diameter 3 cm, C_D is plotted for all accessible velocities, as a function of Q/SU in figure 6.6(a). We can note that for Q/SU above 0.03, all the sets of data align on a master curve, decreasing with the dimensionless air injection rate. The drag coefficient passes from ~ 0.3 for $Q/SU = 0.03$ to ~ 0.22 for $Q/SU = 0.1$. When Q/SU is decreased below 0.03, the sets spread apart to reach the in-crisis drag coefficient limit value without air injection.

This observation can be further checked for a different size of sphere. C_D is shown for two different sizes of sphere in a log-log plot in figure 6.6(b). We first notice that the data for the smaller sphere align with the one previously drawn. Additionally, in the fully developed cavity regime $Q/SU > 0.03$, C_D remarkably follows a power law of exponent $-1/3$ on nearly one decade. The transition between the two regimes happens around $Q/SU \sim 0.03$ which is consistent with our previous observation. The value 0.03 can itself be rationalized: C_D reaches its maximum when the bubble pins at the equatorial plane, which roughly corresponds to a dimensionless length of the bubble l/l_0 of 2 and according to the previous section (figure 6.3) $l/l_0 \sim 2$ for $Q/SU \sim 0.03 - 0.04$.

This observation suggests that the dimensionless size of the bubble should also be a relevant parameter in the study of the drag of the sphere. The drag coefficient is plotted as a function of l/l_0 in figure 6.6(c). The same characteristic feature can be observed: data align in a master curve above 2 on a power law of exponent $-1/3$.

All these observations support the following scenario for the drag modification. When the dimensionless injection rate is greater than 0.03, a large bubble pins at the equatorial plane of the sphere. From that point, increasing Q/SU elongates the bubble ($l/l_0 \sim Q/SU$) which increases the thickness ratio of the global structure. On solid projectile, such as ellipsoids, this is known for reducing the pressure drag while increasing the skin drag [1]. Overall, the variation of the drag on such projectile is found to be well described by the semi-empirical law:

$$C_D = C_F \left(3 \frac{l}{l_0} + 4.5 \left(\frac{l}{l_0} \right)^{-\frac{1}{2}} + 21 \left(\frac{l}{l_0} \right)^{-2} \right) \quad (6.10)$$

where C_F is the skin friction coefficient.

However, as the non-slip condition is released on an air-water interface, in our set-up, we expect the term proportional to l/l_0 to vanish. Thus, increasing the thickness ratio of the whole structure will mainly result in a pressure drag reduction. As a consequence, in the fully developed regime, increasing Q/SU results in a reduction of the drag. Which accurately captures the trend of our experimental observation ($C_D \sim (Q/SU)^{-1/3}$). Nonetheless, we would need to enlarge the range of parameters to discriminate between only a pressure drag reduction (typically a sum of several power terms as in equation (6.10)) or a more complex scenario ($C_D \sim (Q/SU)^{-1/3}$ on a broader range of value of Q/SU).

In the low injection rate regime ($Q/SU < 0.03$) the influence of air injection depends on the value of the Reynolds number: in the sub-critical regime air injection reduces the drag while it increases in the super-critical regime. This is due to the fact that air injection creates a small recirculation zone (identified by the presence of trapped bubbles) in the near wake of the sphere. The size of this zone is non-negligible when compared to the width of the thin super-critical wake. As a consequence, in the super-critical regime, the wake is enlarged by the air injection. In other words, injecting air is equivalent to riding up the drag crisis

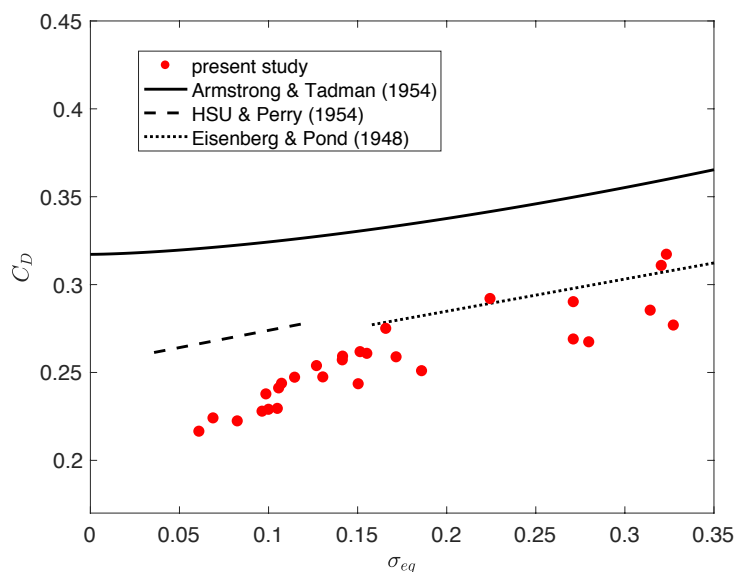


Figure 6.7: Drag coefficient C_D of a sphere as a function of the equivalent cavitation number σ_{eq} . σ_{eq} is evaluated using our measured cavity length and [88]. Theoretical work of [89] is plotted in solid line. Mean line for experimental results [90, 91] are drawn in dashed and dotted lines.

(decreasing Re). This drag increase effect ceases when the size of this recirculation zone is on the order of the size of the projectile (*i.e.* $l/l_0 \sim 2$), after that, a large bubble pins on the sphere.

Finally, our results can be compared to the literature introduced in figure 4.5(b). We first compute an equivalent cavitation number σ_{eq} from the length of the cavity measured in our experiments using figure 4.5(a). For the sphere of diameter 3 cm we used, this predicts a minimum equivalent cavitation number of ~ 0.18 . We then plot C_D as a function of σ_{eq} in figure 6.7. Although the tendency of the measurement is identical to the one observed in [90] and [91], our values are $\sim 0.02 - 0.04$ lower. As before, this could be attributed to a change in the detachment point of the cavity from the sphere due to the air injection method: even though we did not focus on that point, we can easily note in figure 6.2(a) that it is just downstream of the equatorial plane.

6.3.3 Application to supercavitation

Let us reconsider the problem stated in the introduction: can a submarine go up to 100 m/s?

We first compute the cavitation number σ of the flow around the submarine and find $\sigma \sim 0.02$. At this cavitation number, extrapolating our data, we predict that the drag coefficient of the sphere is $C_D \sim 0.2$, *i.e.* a drag reduction of a factor 2.5 in the sub-critical regime or a drag increase of a factor 2 in the super-critical regime. As the width of the submarine is typically metric, we have $Re \approx 10^8$, and in the case of a sphere, the flow would be super-critical.

In any cases, this suggests that supercavitation would not be sufficient to reach the drag reductions necessary to have (spherical) submarines going at 100 m/s. However, the influence of the geometry of the object and the shape of the bubble is important and could change the conclusion stated here. In particular, as shown in [92], the stability of the bubble is crucial: ensuring that perturbations are damped at the interface of the bubble and that the

bubble pinches off in a stationary point as presented in figure 4.4(c), the drag coefficient can be reduced as low as 0.05. This value of the drag coefficient is still too high to make a submarine going at 100 m/s technically feasible. However, it shows that an important drag reduction (by a factor 10) can be achieved using supercavitation, as low as the one that are measured when streamlining a projectile using fairing and presented in the introduction.

Take home message of Part 6

1. **Three types of bubble wakes can be observed:** for small flow velocities, gravity matters and the resulting bubble is large. For higher flow velocities, when the injection rate is small, typically sub-millimetric bubbles are created and part of them are trapped in the near wake of the sphere. For high injection rate and high flow velocity, a nearly cylindrical large bubble pins on the sphere.
2. **There are three relevant dimensionless numbers:** the dimensionless size of the bubble l/l_0 , the dimensionless volumetric air injection rate Q/SU and the drag coefficient C_D .
3. **Characteristic size l of the bubble increases with the injection rate Q .** We have $l/l_0 \sim Q/SU$. This scaling is the result of the air shedding at the trailing edge of the bubble via instabilities growing at the interface. These instabilities are advected by the flow and have an amplitude growing linearly in the streamwise direction.
4. **Drag is modified by air injection.** When a bubble is pinned to the sphere, pressure drag is reduced by the increase of the thickness ratio and we have $C_D \sim (Q/SU)^{-1/3}$. Otherwise, if the sphere is in the sub-critical regime, drag is reduced by air injection. If it is super-critical, injecting air perturbs the wake inducing a large drag increase.

PART III

STABILITY OF THE TRAJECTORY OF THE STREAMLINED PROJECTILE



We have seen in part I that a projectile going fast enough underwater generates a gas bubble around it. We then showed that such a bubble reduces its drag, making the whole system analogous to an inhomogeneous streamlined projectile. In the present part, we characterise the trajectory of a streamlined projectile following its impact on water. In particular, we determine whether the projectile will have a straight trajectory and will reach its target. In chapter 7, we review the literature and present our experimental set-up. We then present our main results in chapter 8: the conditions under which a streamlined projectile follows a straight trajectory.

7

SHORT REVIEW ON WATER ENTRY AND PATH INSTABILITIES



Picture of a gannet about to enter water. Photo credits: Steve Ward Nature Photography (www.stevewardnature.co.uk).

Contents

7.1	Water entry	76
7.2	Path instabilities	78
7.3	Statement of the problem	79
7.4	Experimental details	79

7.1 Water entry

7.1.1 Cavity formation

Modern studies on the impact of projectiles in water started with the experimental work of Worthington and Cole [100]. The reason why it has drawn the attention of so many researchers [101, 102] lies in the diversity of applications. It is obviously of great interest for military purposes such as the optimisation of the shape of missiles [103, 104, 105] or the design of floats for floatplanes [106]. It can also be used to describe the underlying physics of animals wading on water such as basilisk lizards [107, 108, 109], or to understand the dive of birds like gannets [110, 111, 112, 113].

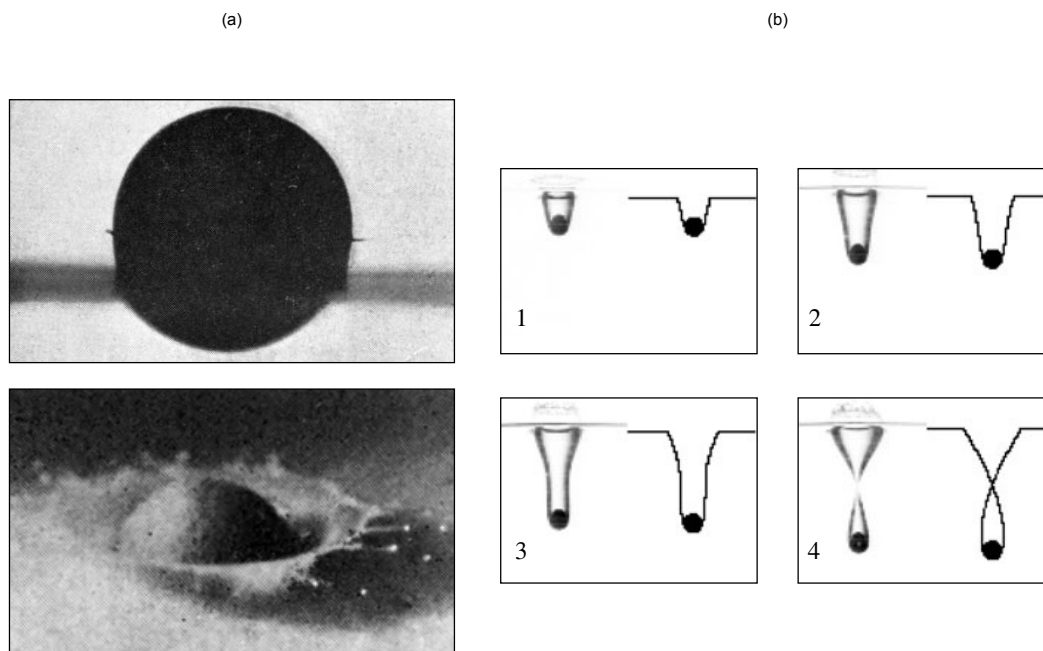


Figure 7.1: (a) Pictures taken 6 ms after the impact of a sphere on water, adapted from [114]. Top panel: side view of a polished serpentine spherical stone of diameter 2.57 cm impacting water after a 14 centimeters fall (*i.e.* an impact velocity of 1.66 m/s). Bottom panel: three-quarter view of a rough sphere of diameter 1.5 cm impacting milky water after a 15 centimeters fall (*i.e.* an impact velocity of 1.72 m/s). (b) Side view of the water entry of a sphere of radius 1.2 cm impacting at a velocity of 2.4 m/s. Comparison between the cavity observed experimentally (left-hand image) and the numerical integration of Bernoulli equation assuming potential flow (right-hand image). Figure adapted from [115].

The early works have focused on characterising the splash emitted at the surface of the fluid when it is impacted by a projectile, for instance a sphere. Splash appears only for an impact velocity U_0 greater than a threshold value which was found to depend on two main parameters: the fluid properties and the surface characteristics of the projectile [114]. This is illustrated in the two pictures of figure 7.1(a), adapted from [114]. The top picture is taken 6 ms after the impact of a smooth sphere on water. On this side view of the impact, following a 14 centimeters fall ($U_0 = 1.66$ m/s), no splash is observed: only a thin film of water covers part of the smooth sphere. Conversely, when a rough sphere, initially released from an equivalent height ($U_0 = 1.72$ m/s), impacts on water, it produces a large splash (bottom picture).

When a splash is observed, a large quantity of air is entrained by the projectile at the passage

of the air-water interface, which forms a cavity. Many of the following studies focused on describing and modelling the dynamic of the cavity [103, 104, 116, 115], underlying the influence of the ambient air [117] and of the surface properties of the projectile [118, 119]. The main features of the cavity dynamic are gathered in the chronophotography (left) and numerical simulation (right) presented in figure 7.1(b), adapted from [115]. In a first part of the entry, air is entrained behind the projectile and the cavity grows both vertically and horizontally (1 and 2). In a second part, the cavity keeps growing vertically but shrinks horizontally (3) until it completely closes at pinch-off (4) [120]. After that, both parts of the cavity resorbs. The numerical simulation is obtained assuming potential flow and captures all the previously described features. It also quantitatively matches fairly well the observations.

7.1.2 Slender bodies

So far, we have presented results on spherical bodies, however, the bodies we are interested in are elongated axisymmetric bodies. Impact of such bodies have recently drawn the attention of many researchers [121, 122, 123], which can be explained by the complex dynamic of the cavity. Indeed, even though the projectile is axisymmetric and impacts water almost perpendicularly, the resulting cavity can be very asymmetric.

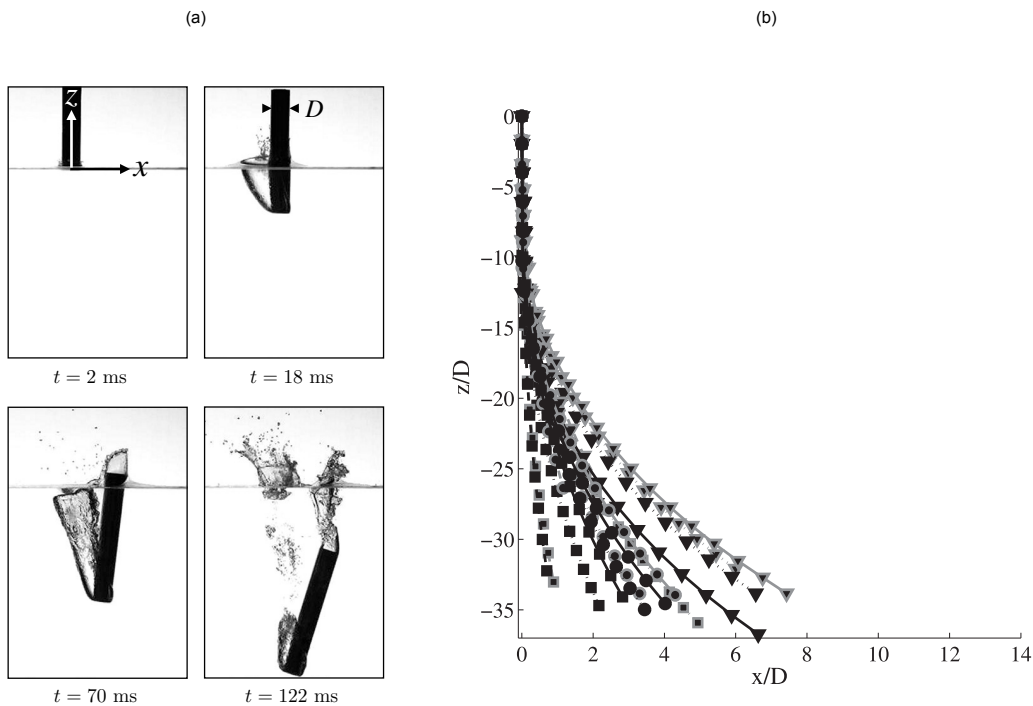


Figure 7.2: (a) Chronophotography of a cylinder impacting water taken from [122]. At the impact, the cylinder has a vertical velocity of 2.45 m/s and an horizontal velocity of 0.98 m/s. The cylinder has a diameter of $D = 29$ mm. (b) Trajectories of the center of mass of a cylinder after its impact on water. The angle of the projectile at the impact is 2° . Gray data are for an initial vertical velocity of 2.7 m/s while black data are for a vertical velocity of 3.13 m/s. Material, surface properties and shape of the end of the cylinder are varied.

This situation is represented in the chronophotography of figure 7.2(a), taken from [122] where a cylinder impacts water at an angle $\sim 0.4^\circ$ with the vertical. At impact, the projectile has a vertical velocity of 2.45 m/s and an horizontal velocity of 0.98 m/s. Up to 18 ms

after impact, the projectile remains close to vertical. However, the air cavity entrained is asymmetric and is only on one side of the projectile. When the cavity grows the projectile rotates ($t = 70$ ms) resulting in a projectile at an angle $\sim 15^\circ$ at the pinch-off of the cavity ($t = 122$ ms). This rotation of the projectile will induce an horizontal motion for the centre of mass of the projectile.

Such lateral deviation of the center of mass of a slender projectile after the passage through an air-water interface was also reported in [121], and so, without initial horizontal velocity. Noticeably, this deviation is recorded no matter the shape of the end of the cylinder and its surface properties as shown on figure 7.2(c) taken from [121]. The main parameter influencing the magnitude of the deviation appears to be the initial angle: as one could guess, the lateral deviation grows with the initial angle.

7.2 Path instabilities

However, the previous studies only focused on the early times after the passage of the interface: one could wonder what is the trajectory of the projectile long after the crossing of the interface? This question is particularly relevant for applications requiring to reach a specific position underwater (diving bird or military applications).

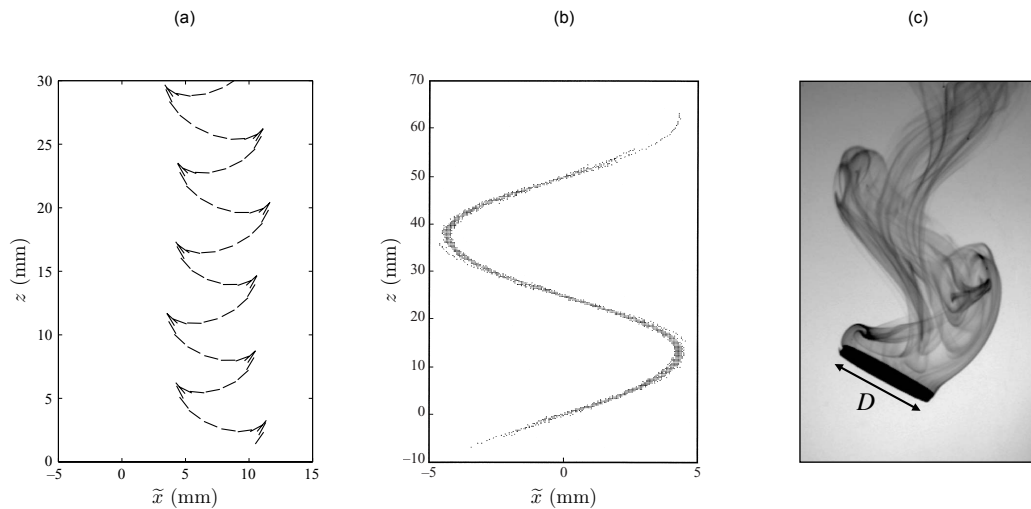


Figure 7.3: (a) Experimental fluttering of a plate of thickness 0.089 cm and of aspect ratio $1/14$ at a Reynolds number $Re = 1147$. The time step is 0.04 s. Figure taken from [124]. (b) Trajectories, in the mean oscillation plane (z, \tilde{x}) , of 71 rising bubbles of radius 2.5 mm. Figure taken from [125]. (c) Smoke visualization of the wake behind a disk of aspect ratio $1/10$ at $Re \approx 240$. Picture adapted from [126].

The trajectory of a falling or rising object in a fluid can show complex behaviour even in an infinite bath [127]. For instance, a light thin plate, initially released horizontally will follow a characteristic oscillatory motion, called fluttering and often referred as "the metro ticket instability". Such motion is presented in figure 7.3(a) taken from [124]. A thin square plate, of aspect ratio $\chi = \frac{\text{thickness}}{\text{width}} = 1/14$, initially released horizontal follows an oscillatory motion of amplitude ~ 3 time its side when falling. This behaviour is one example of the whole family of trajectories, that ranges from nearly sinusoidal oscillations to chaotic motion [124], which can be observed with a falling plate. The main parameters

that determine the trajectory of a falling square plate of thickness t and side D at a velocity U are: the aspect ratio of the object $\chi = e/D$, its density ratio $\bar{\rho} = \frac{\rho_{object}}{\rho_{fluid}}$ and its Reynolds number $Re = UD/\nu$, where ν is the cinematic viscosity of the fluid. A thorough review of their influence is made in [127].

However, it is interesting to note that oscillatory trajectories are also recorded for objects as simple as spheres. Indeed, a rising bubble in a fluid will follow a nearly sinusoidal trajectory as shown in figure 7.3(b) taken from [125]. This plot presents the trajectories, in the mean plane of oscillation (z, \tilde{x}) , of 71 bubbles rising in water. Their trajectory is consistently sinusoidal of amplitude ~ 2 bubble diameter. The fact that such oscillatory paths are observed for fully spherically symmetric objects like bubbles led to discover that they arise from the fluctuating wake. This is illustrated by the smoke visualization picture of the wake of a flat cylinder presented in figure 7.3(c), taken from [126]. We observe the periodical vortices emitted from the rim of the cylinder.

7.3 Statement of the problem

Here we wish to extend the studies on impact of elongated bodies ($\chi > 1$) to their late time behaviour. Additionally, considering some of the biological and military applications, we consider floating projectiles ($\bar{\rho} < 1$), which corresponds to a complement to the literature on floating object so far focused on rising bubbles ($\bar{\rho} \ll 1$). Finally, to better model supercavitating projectile, we will consider the mass distribution of the projectile inhomogeneous. In this part, we wish to determine both experimentally and theoretically, the trajectory after impact of floating axisymmetric streamlined bodies. We focus on two main questions, which are crucial for both military applications and understanding the way birds, like gannets, dive:

- What is the maximum depth that can be reached?
- Is the trajectory of such projectile straight? In other words, can a passive projectile reach its target?

7.4 Experimental details

7.4.1 Trajectory reconstruction

To that end, as shown in figure 7.4(a), we release our projectiles without initial velocity from a height H above a square-based tank of dimensions 60 cm by 60 cm by 100 cm. When a projectile reaches the water surface, its impact velocity is U_0 and its impact angle with the vertical is θ_0 . Its trajectory is followed using two perpendicular, synchronized cameras recording the motion underwater, as sketched in figure 7.4(a). We use two high-speed cameras Photron mini UX-100, equipped with 20mm f/1.8 Nikon lenses, recording at frame rates ranging from 250 to 1500 frames per second. Taking into account magnification due to the passage through the air-water interface as well as the divergence of the field of view of the camera, we determine the three-dimensional position of the center of gravity of the projectile for each pair of frames recorded by the two cameras with a precision on the order of a few millimeters. U_0 is determined using the first 20 frames following the impact.

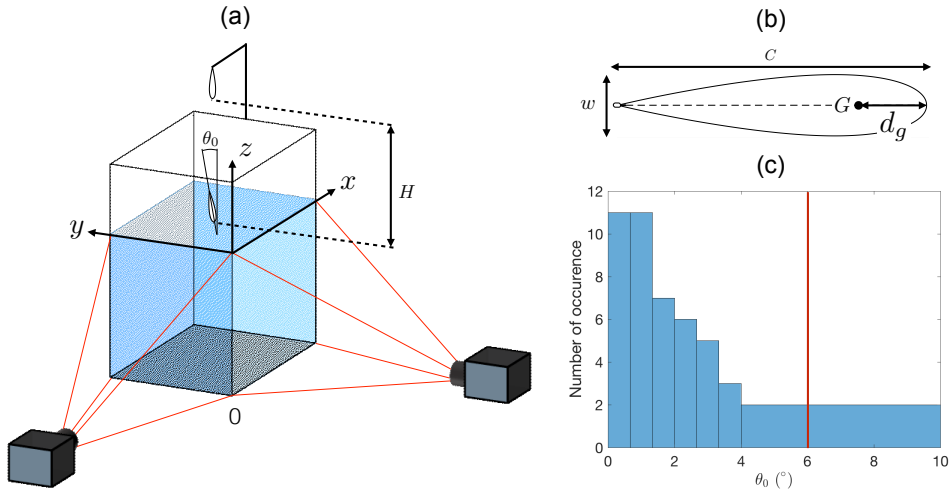


Figure 7.4: (a) Sketch of the set-up used to follow the underwater trajectory of the projectiles. θ_0 is the angle between the axis of symmetry of the projectile and the vertical at the impact. The projectile is released at a height H above the water surface. (b) Sectional drawing of the projectiles used for our experiments. The dashed line represents the chord and is used as the rotation axis to create the 3D axisymmetric projectile where the center of gravity G is located at a distance d_g from the leading edge. The projectile has a length C and a maximum width w and its aspect ratio $\chi = C/w$ is 5 for all our experiments. The eye of a needle is attached to the trailing edge of the projectile. (c) Distribution of the impact angle θ_0 for various impact velocity. As marked with the red line, the impacting angle is lower than 6° for 95% of the experiments.

7.4.2 Projectiles

The projectiles used in our experiments are axisymmetric bodies generated by the rotation of a wing profile around its chord, as shown in figure 7.4(b). The profile is such that its maximum width w is one fifth of the length C of its chord, as defined by the National Advisory Committee for Aeronautics as the profile NACA 0020. The projectiles are 3D printed in Acrylonitrile Butadiene Styrene (ABS) and smoothed above an acetone bath at 70°C during two minutes. The resulting objects are then coated with Rain-X to increase their hydrophilicity and thus reduce the generation of air cavities when crossing the air-water interface [118]. Projectiles are hollowed out and a moving brass cylinder ballasts the body and allows us to tune the position of their center of gravity. The eye of a needle is attached to their trailing edge for their release.

The projectiles are 75 mm long and 15 mm thick, with an aspect ratio $\chi = C/w$ of 5. Their mass is between 6.2 g and 6.9 g. As they are slender, their added mass is neglected in the rest of the study. Their relative density $\bar{\rho} = \frac{\rho_{\text{projectile}}}{\rho_{\text{water}}}$ ranges from 0.85 to 0.95. The distance d_g from the leading edge to the center of mass of the projectile is varied from 18% to 45% of the cord.

7.4.3 Releasing method

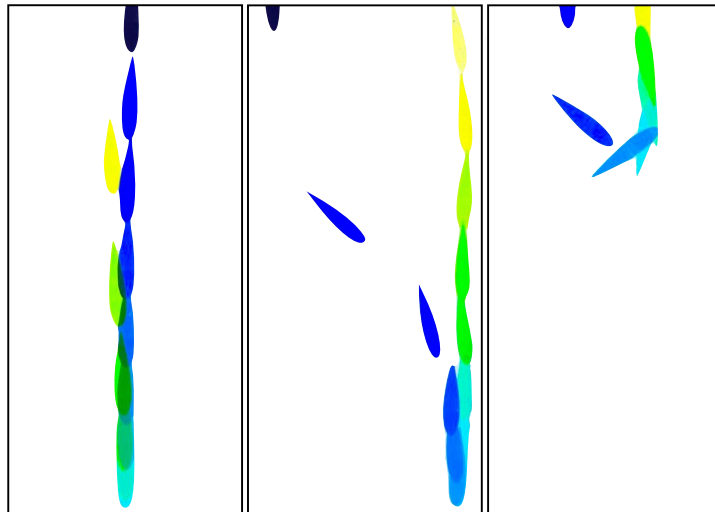
In order to release the projectile without initial velocity nor initial angle, we hold it by the eye of a needle placed at its trailing edge with a $105 \mu\text{m}$ -thick nylon fiber onto a 0.5 mm-thick copper wire. Upon current running through the wire, nylon melts and the projectile is released vertically. The impacting velocity U_0 ranges from 0.1 to 2.1 m/s. The impact angle θ_0 is measured using two cameras set just above the water surface. The histogram in figure

7.4(c) shows that our method ensures an impact angle below 6° in 95% of the experiments.

8

PATH INSTABILITIES OF STREAMLINED BODIES

This work has been done in collaboration with Martin Coux, at the time when he was second year PhD student in the group. It was started by Zhixin Pan during his internship. All this study would not have been possible without the help of Romain Labbé and Caroline Frot.



Chronophotography of three different underwater trajectories of floating streamlined projectile.

Contents

8.1	Experimental Results	84
8.2	Equations of motion and closing parameters	87
8.3	Results and discussion	91
8.4	Controlling the instability	96

8.1 Experimental Results

8.1.1 Nature of the trajectory

We display in figure 8.1 the different possible trajectories of the projectiles, depending on their impact velocity U_0 and location d_g of the mass center. In the six presented experiments, projectiles are floating and the global motion is the same: the projectile impacts water almost vertically, slows down until it reaches its maximum depth before moving back toward the water surface.

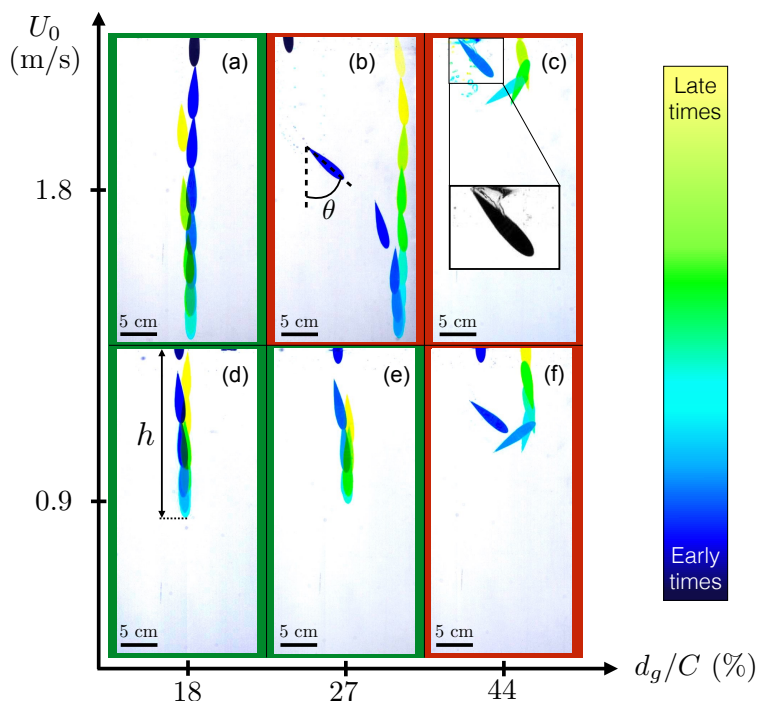


Figure 8.1: Chronophotographies of the projectile trajectories for various impacting velocities U_0 , and for various distances d_g between the center of gravity of the projectile and its leading edge. The center of buoyancy is located at 37.5 % of the total chord from the leading edge. For all chronophotographies, frames are separated by 0.15 seconds. The stable trajectories are boxed in green whereas the unstable ones are boxed in red.

The two chronophotographies on the left-hand side of figure 8.1 (2a, 2d) correspond to the trajectories of projectiles whose center of mass is located close to the leading edge ($d_g/C = 18\%$). For such projectiles, both at low impact velocity ($U_0 \approx 0.9$ m/s for 2d) and high impact velocity ($U_0 \approx 1.8$ m/s for 2a), the path followed in the descending phase is a vertical straight line. At the maximum depth of the dive, the projectile has no velocity. Later, it follows the same straight path as in its ascending phase until the trailing edge reaches the water surface close to the impacting point. The depth h increases with the impact velocity.

The two chronophotographies centered in figure 8.1 (2b, 2e) correspond to the impacts of a projectile with a center of mass located at $d_g/C = 27\%$. At low impact velocity ($U_0 \approx 0.9$ m/s for 2e), the trajectory followed by the projectile is a vertical straight line in both descending and ascending phases, as observed earlier. However, the trajectory changes at higher impact velocity ($U_0 \approx 1.8$ m/s for 2b). In the first half of the descending phase, the projectile rotates such that the angle θ between its chord and the vertical increases

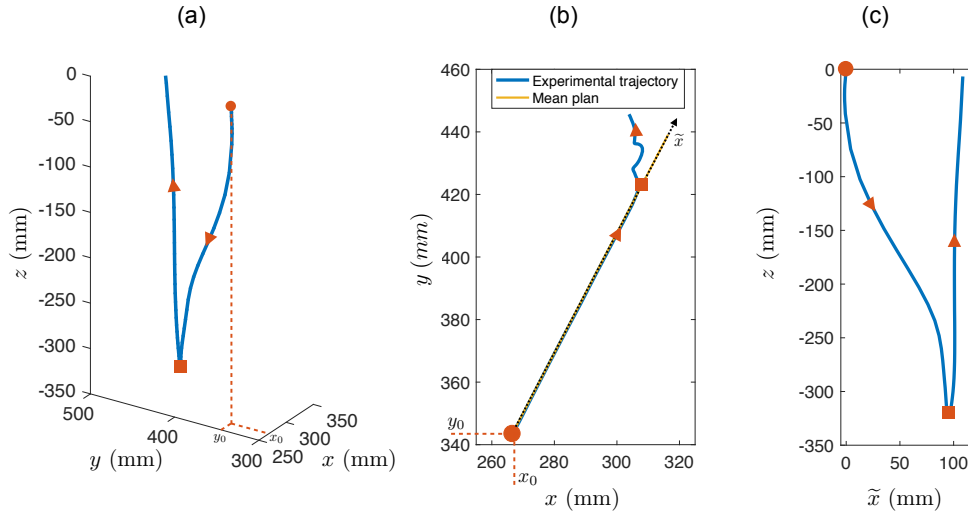


Figure 8.2: (a) Underwater 3D trajectory of the center of mass of the projectile after its impact at the red spot of coordinates $(x_0, y_0, 0)$. The maximum depth of the dive is reached at the red square. The trajectory is obtained from the images of the two high-speed cameras. (b) The blue curve is the actual projected trajectory of the projectile onto the (Oxy) plane. Projectile impacts water at the red spot and reaches its maximum depth at the red square. The yellow straight line is the projection of the mean plane of the trajectory in the descending phase onto the (Oxy) plane. The direction of the axis \tilde{x} is contained in the mean plane of the trajectory. (c) Projected trajectory on the mean plane defined in (b). The coordinate $\tilde{x} = |x - x_0|$ is defined such that the origin coincides with the impact point marked by the red spot.

and its path deviates from a straight line. In the second half of the descending phase, the projectile slowly realigns with the vertical (θ decreases) until it reaches its maximum depth. At this point, the projectile has no velocity and is fully aligned with the vertical with its leading edge pointing down ($\theta = 0$). Then, in the ascending phase, the projectile follows a vertical straight line up to the water surface, which it reaches at a point different from that at impact. We call "y-shaped" such a trajectory. Increasing the impact velocity increases the horizontal distance between the entry and exit points.

The two chronophotographies on the right-hand side of figure 8.1(2c, 2f) finally correspond to impacts of a projectile whose center of mass is located far from the leading edge ($d_g/C = 44\%$). At low impact velocity ($U_0 \approx 0.9$ m/s for 2f), the projectile rotates (θ continually increases) and the trajectory deviates from the vertical during the descending phase. The projectile reaches its maximum depth horizontally ($\theta = 90^\circ$) with a non-zero horizontal velocity. In the ascending phase, the projectile keeps on rotating until its leading edge reaches the water surface ($\theta \approx 180^\circ$) at a different location from the impacting point. Such a trajectory has a "U-shape". Compared with the straight trajectories observed at the same impact velocity for projectiles with center of mass closer to the leading edge, the projectile travels further horizontally but the dive is shallower. Even though the shape of the trajectory is not modified at higher impact velocity ($U_0 \approx 1.8$ m/s), the depth of the dive is reduced - due to the existence of a large cavity of air entrained at water entry, as shown in the inset of figure 8.1(c).

To summarize our observations, three different types of trajectory can be observed : straight, y-shaped and U-shaped. Straight trajectories appear for a center of mass located close to the leading edge and at low impact velocity. When velocity is increased, the motion follows a y-shape. Finally, when the center of mass is far from the leading edge, the trajectory has

a U-shape at all velocities .

8.1.2 Quasi-planar trajectories

For a y-shaped path, a typical 3D-trajectory of the center of mass of the projectile is presented in figure 8.2(a). The projectile impacts water at the coordinates $(x_0, y_0, 0)$. When plotted in the (Oxy) plane, orthogonal to gravity, the trajectory is close to be planar, apart from the ascending phase, where the projectile slowly drifts and oscillates, as shown in figure 8.2(b). Hence, we can define the mean vertical plane of the descending phase of the trajectory drawn in yellow in figure 8.2(b). Finally, we define a new coordinate system (\tilde{x}, z) centered at the impact point ($\tilde{x} = |x - x_0|$) and the 3D trajectory is projected along the mean plane to obtain the typical 2D Y-shaped trajectory plotted in figure 8.2(c). This protocol is followed for the three types of trajectory observed (straight, U-shaped, y-shaped).

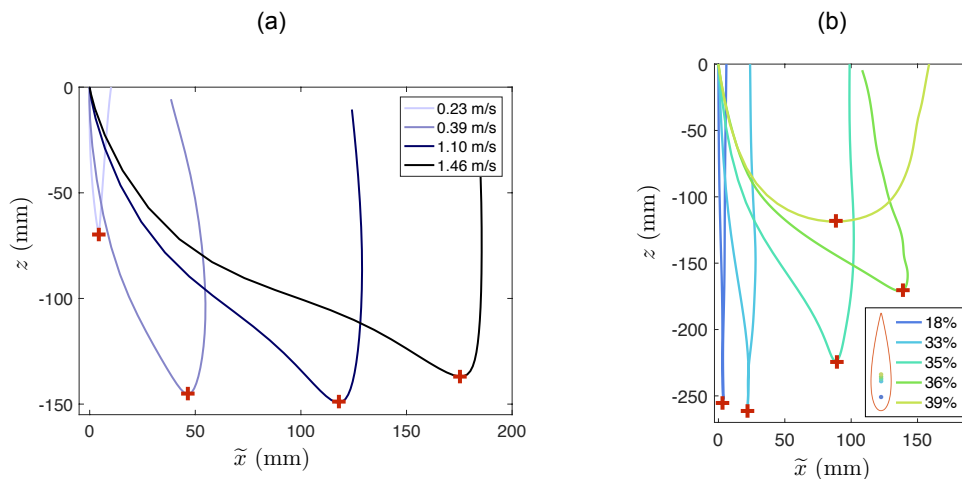


Figure 8.3: (a) Experimental trajectories for a projectile with a fixed position of the center of gravity ($d_g/C = 35\%$) and a mass of $m = 6.4$ g. The impact velocity U_0 is varied from 0.23 to 1.46 m/s. Red crosses represent the maximum depth of the dive h for each dive. (b) Experimental trajectories for an impact velocity of 0.91 m/s. The relative position of the center of gravity (d_g/C) of the projectile is moved from 18% to 39%. The mass of the projectile is kept constant at $m = 6.7$ g. The center of buoyancy is located at 37.5% of the total chord from the leading edge. The standard deviation of the impacting velocity is 0.04 m/s over the set of trajectories. Red crosses represent the point of maximum depth h .

Figure 8.3 shows experimental trajectories obtained varying independently the impact velocity U_0 and the position d_g of the center of gravity of the projectile. In figure 8.3(a), the center of mass of the projectile is fixed ($d_g/C = 35\%$) and the impact velocity is varied. The transition between straight and Y-shaped trajectory is observed between 0.23 and 0.39 m/s. Above the latter speed, the horizontal travelled distance increases with the impact speed while the maximum depth h hardly depends on U_0 .

As shown in figure 8.3(b), an increase of the distance d_g modifies the shape of the trajectory: at $U_0 = 0.91$ m/s when $d_g/C < 33\%$, the trajectory is straight, when $33\% \leq d_g/C < 38\%$, the trajectory has a y-shape and above 38%, the trajectory is U-shaped. Overall, when d_g is increased at fixed impact velocity, the depth of the dive is reduced and the horizontal distance travelled is increased. Hence, there is an optimal impact velocity and position of the center of mass such that the dive depth h is maximum.

8.2 Equations of motion and closing parameters

8.2.1 Presentation of the model

In the plane of the trajectory, the position of the projectile at every moment is fully described by the two coordinates of the center of mass of the projectile (\tilde{x}_g, z_g) and the angle θ , as presented in figure 8.4(a).

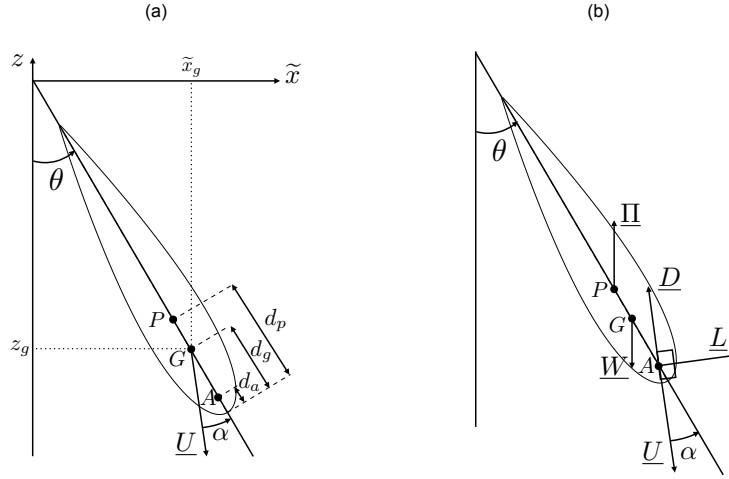


Figure 8.4: (a) Schematic representation of the projectile during its underwater motion, θ is the angle between the vertical and the chord of the projectile, α the angle of attack of the projectile (angle between the velocity \underline{U} and the chord of the projectile). P is the point of application of the Archimedes' force, G the center of gravity of the projectile of coordinates (\tilde{x}_g, z_g) in the laboratory frame of reference and A the point of application of the hydrodynamic forces. d_a , d_g and d_p are the distances between the leading edge and respectively A, G and P . (b) Forces applied to the projectile during a dive. $\underline{\Pi}$ is the Archimedes' force, \underline{W} the weight, \underline{D} the drag and \underline{L} the lift.

For a projectile moving underwater at a velocity \underline{U} , with an angle of attack α , the sketch of figure 8.4(b) shows the forces coming into play. The projectile is subjected to the Archimedes' force $\underline{\Pi}$, applied at the point P ; the lift \underline{L} and the drag \underline{D} , that is, the hydrodynamic forces, both applied at the hydrodynamic center A and respectively orthogonal and aligned with the velocity \underline{U} ; the weight \underline{W} applied at the center of mass G . The points A , G and P are respectively located at a distance d_a , d_g and d_p from the leading edge of the projectile, as defined in figure 8.4(a). The evolution of the position and angle of a projectile of mass m and moment of inertia J are given by Newton's second law and the conservation of the angular momentum:

$$\begin{cases} m \frac{d\underline{U}}{dt} = \underline{W} + \underline{\Pi} + \underline{L} + \underline{D} \\ J \frac{d^2\theta}{dt^2} = -\Pi(d_p - d_g) \sin \theta + (d_g - d_a)(L \cos \alpha + D \sin \alpha) - \mathcal{D}_t \end{cases} \quad (8.1)$$

where $-\Pi(d_p - d_g) \sin \theta$ is the moment of the Archimedes' force, $(d_g - d_a)(L \cos \alpha + D \sin \alpha)$ the moment of the hydrodynamic forces and \mathcal{D}_t a fluid friction force resisting rotational motion.

The mass of the projectile m is determined using a scale Mettler H51AR with a precision of 10 mg. The moment of inertia J of the projectile depends on the shape and the mass

distribution in the object and it is computed numerically or with a CAD software. The distance d_p corresponds to the position of the center of mass of an homogeneous projectile and thus only depends on the shape of the projectile. For our projectile, it is found to be 37.5% of the total chord. The distance d_g is predicted theoretically during the design and experimentally verified with a precision of 1% of the total chord. The way to measure drag and lift force, the distance d_a and the angular dissipation torque \mathcal{D}_t are discussed in the following sections.

8.2.2 Lift and Drag

In the range of Reynolds numbers $10^3 < Re < 10^5$ corresponding to our experiments, where we define Re as the ratio of $U_0 w$ to the kinematic viscosity of water ν , the amplitudes of lift and drag are expressed as follows [1, 128]:

$$\begin{cases} D = \frac{1}{2}\rho S C_D(\alpha) U^2 \\ L = \frac{1}{2}\rho S C_L(\alpha) U^2 \end{cases} \quad (8.2)$$

where ρ is the density of water, S the total surface area of the projectile, U its velocity, C_D and C_L the drag and lift coefficients.

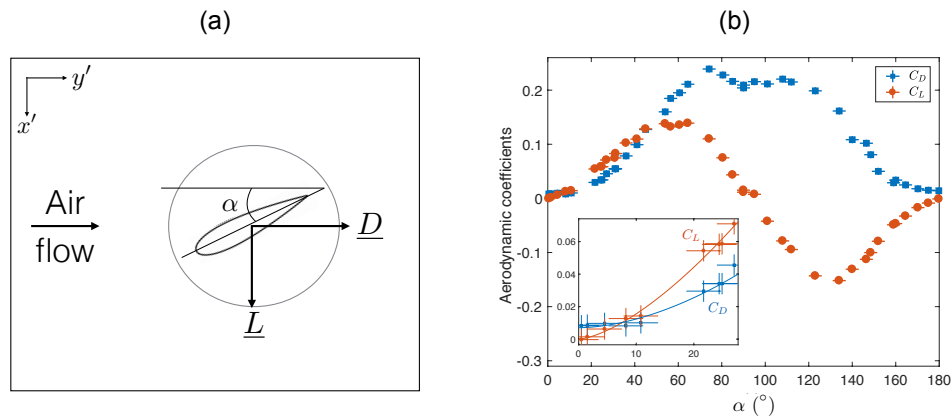


Figure 8.5: (a) Sketch of the experiment used to measure the lift \underline{L} and the drag \underline{D} forces onto the projectile when placed in an air flow in the y' direction with an angle of attack α . Forces are measured simultaneously with a Sixaxes scale -a strain gauge scale capable of measuring forces and moments along three axis-. (b) Drag and lift force coefficients C_D (red squares) and C_L (blue dots) as a function of the angle of attack α . Lift and drag coefficients are defined such that $L = \frac{1}{2}\rho S C_L(\alpha) U^2$ and $D = \frac{1}{2}\rho S C_D(\alpha) U^2$, where ρ is the density of the fluid and S the total surface area of the projectile. The experiments were carried out at a Reynolds number ranging from 9×10^3 to 5×10^4 . The inset is a close-up on the low angle of attack regime ($\alpha < 30^\circ$). In this regime, C_L is fitted by $0.00048 \times \alpha^{1.5}$ (red solid line) and C_D by $0.0070 + 0.000088 \times \alpha^{1.8}$ (blue solid line)

C_D and C_L are experimentally determined in a wind tunnel. Projectiles of different sizes are held with an angle of attack α onto a Sixaxes scale measuring forces in the air flow of velocity U , as shown in figure 8.5(a). After averaging forces over one minute, the dependence of C_L and C_D on the angle α is plotted in figure 8.5(b). At $\alpha = 0^\circ$, the profile is symmetric and the lift coefficient C_L is 0. C_L increases up to 0.14 for α between 40° to 60° before decreasing back to zero around 90° . C_L changes its sign for $\alpha > 90^\circ$ and it reaches -0.15 around $\alpha = 135^\circ$. As the projectile is streamlined, the drag coefficient is close to 0 (0.009)

at $\alpha = 0^\circ$. C_D increases to reach a plateau value around 0.22 between $\alpha = 80^\circ$ and 120° . It then decreases back to a low value (0.012) at 180° . As a consequence, this axisymmetric projectile has a high stall angle (around 50°) when compared to cylindrical wings (10° to 30°) [128].

8.2.3 Position of the aerodynamic center

The aerodynamic center is defined as the point of application of lift and drag. At this point, no torque is exerted by the resulting pressure forces. As a consequence, its position may vary with the angle of attack. As the projectile considered in this study is thin and axisymmetric, it is assumed that the aerodynamic center is located on the chord of the projectile.

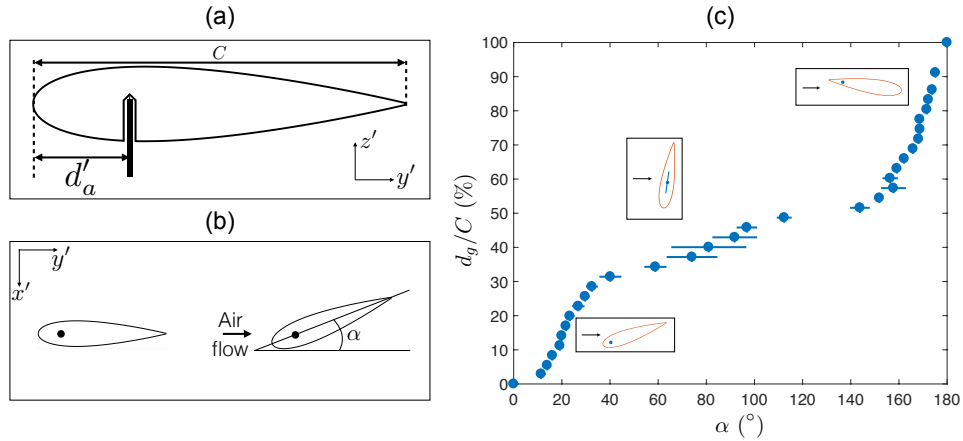


Figure 8.6: (a) Sectional drawing of the experimental set-up used to determine the position of the aerodynamic center. The projectile is placed onto a vertical rod at a distance d'_a from the leading edge. The projectile is free to rotate around the vertical z' -axis. (b) The set-up is placed in a wind tunnel with an airflow aligned with the y' -axis. The projectile equilibrates at a position such that the aerodynamic center of the projectile is located on the holding point. The angle of attack α is averaged over ten pictures. (c) Dependence of d_a/C on the angle of attack α . The experiments were carried out at a Reynolds number of 5×10^4 .

To experimentally determine the position of the aerodynamic center, a projectile is held horizontally by a vertical brass rod located at a distance d'_a from the leading edge, allowing a free rotation around the vertical axis as shown in figure 8.6(a). When this set-up is placed into the test section of a wind tunnel with the air flow aligned with the y' -axis, as sketched in figure 8.6(b), the projectile equilibrates at an angle of attack α . This stable position indicates that the torques of both lift and drag vanish at the holding point of the projectile. Hence, the angle of attack α of equilibrium is such that the position of the aerodynamic center, located at a distance d_a from the leading edge, coincides with the holding point: $d_a = d'_a$. Varying the holding point d'_a using different 3D printed projectiles gives access to the position of the aerodynamic center d_a for different angles of attack α . In figure 8.6(c), we present the position of the aerodynamic center d_a/C (%) as a function of the angle of attack α .

The position of the aerodynamic center d_a is increasing with the angle of attack α . For $\alpha = 0^\circ$, the aerodynamic center is located at the leading edge ($d_a/C = 0\%$). d_a/C increases rapidly between $\alpha = 0^\circ$ and 40° from 0% to 30%, as well as between $\alpha = 160^\circ$ and 180° from 60% to 100%. At $\alpha = 180^\circ$, the aerodynamic center is located at the trailing edge ($d_a/C = 100\%$).

8.2.4 Dissipative torque

The dissipative torque \mathcal{D}_t models the fluid friction resisting a purely rotational motion of the projectile. In the range of Reynolds numbers corresponding to the experiments, the torque takes the following form:

$$\mathcal{D}_t = \frac{1}{2} \rho S C^3 C_a(d_g) \frac{d\theta}{dt} \left| \frac{d\theta}{dt} \right| \quad (8.3)$$

where $C_A(d_g)$ is the non-dimensional angular dissipation coefficient. To determine C_A , we use the set-up presented in figure 8.7(a): a 10 cm long stainless steel projectile is free to rotate around a vertical rod fixed onto the projectile at a distance d_r from its leading edge. A stable position, drawn in dashed line, is set with a torsional spring. The projectile is released at an initial angle from the stable position with no initial angular velocity and the time evolution is recorded at 250 fps. A chronophotography is shown in figure 8.7(a) and the angle $\beta(t)$ between the equilibrium position and the current position is tracked in figure 8.7(b). $\beta(t)$ is fitted with a solution of:

$$J_m(d_r) \frac{d^2\beta}{dt^2} = -K_{ts}\beta - F_s \frac{d\beta}{dt} - \frac{1}{2} \rho S C^3 C_A(d_r) \frac{d\beta}{dt} \left| \frac{d\beta}{dt} \right| \quad (8.4)$$

where $J_m(d_r)$ is the moment of inertia of the projectile and is determined numerically, K_{ts} is the torsional spring constant measured independently, F_s is the solid friction torque determined by carrying out the experiment in air and C_A is the coefficient of angular dissipation and the fitting parameter. A typical fit is shown in figure 8.7(b), which nicely captures the data provided, yields an order of magnitude for $C_A \approx 10^{-2}$.

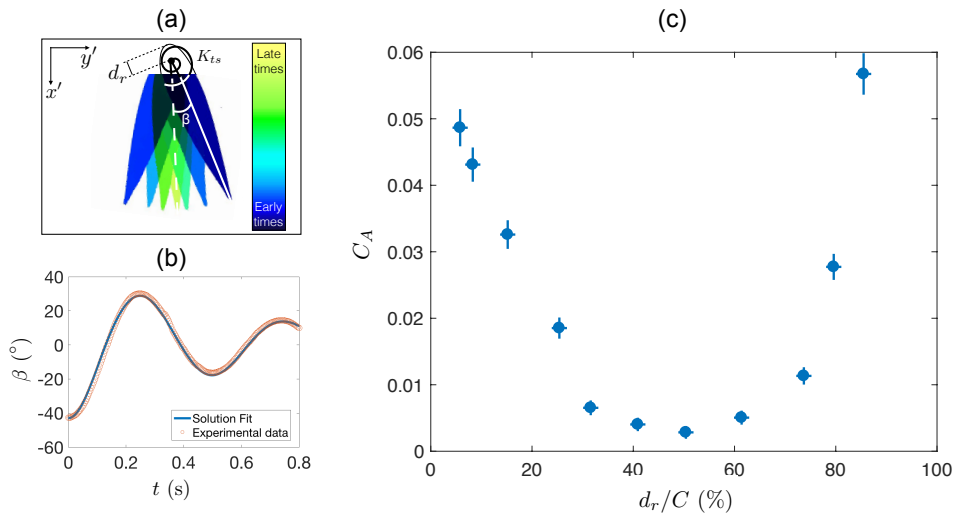


Figure 8.7: (a) Chronophotography and sketch of the experiment used to determine the dissipative torque. The time delay between two frames is 0.24 second. d_r defines the position of the axis of rotation, aligned with the z' -axis. A torsional spring of constant K_{ts} sets an equilibrium position. The angle β is the angle between the projectile at equilibrium and its current position. (b) Time evolution of the angle β fitted with a solution of the equation of motion (8.4) to determine the coefficient C_A such that $\mathcal{D}_t = \frac{1}{2} \rho S C^3 C_A(d_r) \frac{d\beta}{dt} \left| \frac{d\beta}{dt} \right|$. (c) Dependence of C_A with the position d_r/C of the axis of rotation of the projectile, where C is the length of the chord of the projectile.

By moving the position of the axis of rotation d_r , the function $C_A(d_r)$ is determined and plotted in figure 8.7(c). C_A is maximum (0.06) for extreme values of d_r/C (5 % and 85 %)

and it reaches its minimum for d_r/C around 50%.

In the impacting projectile experiment, the projectile rotates around its center of gravity. Hence, for a projectile with a gravity center located at a distance d_g from the leading edge \mathcal{D}_t is computed with a coefficient $C_A(d_g) = C_A(d_r = d_g)$.

8.3 Results and discussion

8.3.1 Solution of the equation of motion

The equations of motion (8.1) can be solved using the parameters determined in the previous section and the initial conditions. Figure 8.8 presents a set of trajectories obtained after integrating numerically the equations for different impact velocities U_0 and various relative positions d_g/C of the center of mass. The overall shapes of the trajectories are similar to those observed experimentally and reported in figure 8.1. Indeed, for a gravity center located close to the leading edge ($d_g/C = 18\%$), the trajectories at both low and high impact velocity are straight -left-hand side of figure 8.8(9a, 9d)-. When the center of mass is further from the leading edge ($d_g/C = 27\%$), the trajectory remains straight at low velocity (9e) but it adopts a Y-shape at high velocity (9b). Finally, for a center of gravity far from the leading edge ($d_g/C = 44\%$), the trajectory is U-shaped at all impact velocities (9c, 9f).

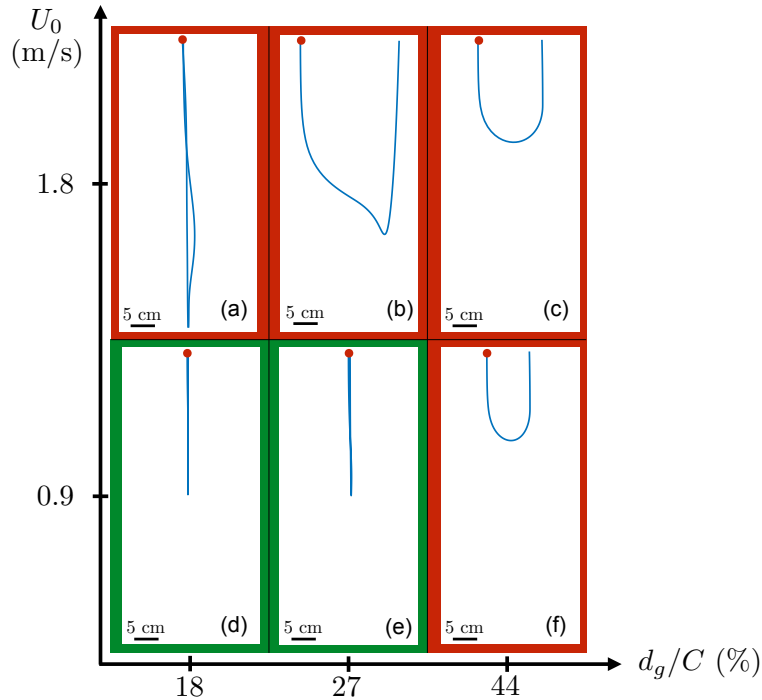


Figure 8.8: Trajectories of the center of mass of the projectile calculated from the numerical resolution of the equations of motion at different values of the impacting velocity (U_0), and for different positions of center of gravity of the projectile (d_g/C). A trajectory is considered unstable if we have $\frac{d\theta}{dt}(t = 0^+) > 0$. Stable trajectories are boxed in green, unstable ones in red.

However, two discrepancies can be noted when comparing the observations in figure 8.1 to the numerical solutions in figure 8.8. First, for $d_g/C = 44\%$, there is no reduction of the

dive depth for $U_0 = 1.8$ m/s, which is due to the fact that the equations of motion do not take into account the formation of air cavities. Second, in the numerical resolution, the motion is considered unstable if $\frac{d\theta}{dt}(t = 0^+) > 0$, that is, if the projectile deviates from its initial position θ_0 away from the vertical ($\theta = 0$) just after impacting water. Although the trajectory obtained for $U_0 = 1.8$ m/s and $d_g/C = 18\%$ appears straight, it is found to be numerically unstable. This can be explained by taking into account the growth rate of the instability, which is addressed in the next subsection.

8.3.2 Critical velocity and growth time

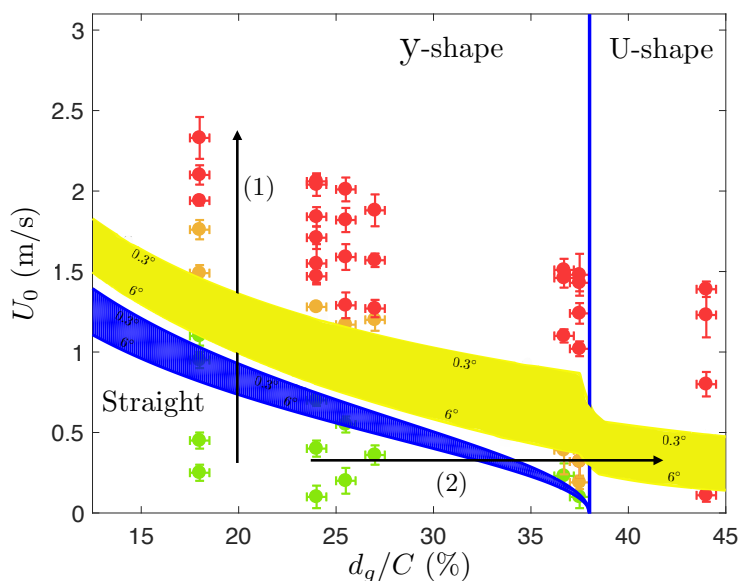


Figure 8.9: Stability diagram of a projectile impacting water at a velocity U_0 with its center of mass located at a distance d_g from the leading edge. The critical velocity U^* theoretically predicted is plotted in blue for impact angle θ_0 between 0.3° and 6° . The area delimited by the curves for which the characteristic growth time of the instability τ_i equates the characteristic time of the fall τ_f (*i.e.* $\tau_i/\tau_f = 1$ with $\Delta\theta = \pi/2$) for $\theta_0 = 0.3^\circ$ and 6° , is shaded in yellow. Experimental points are the green dots (stable), orange dots (transition) and red dots (unstable).

As observed in figure 8.4(b), if the center of mass of the projectile is located closer to the leading edge than the point of application of the Archimedes' force ($d_p > d_g$), Archimedes' torque is stabilizing (it tends to align the projectile with the vertical) whereas the lift and drag torques are destabilizing. Hence, we can define a critical velocity U^* at which the destabilizing and the stabilizing torques balance. Since the drag and lift forces apply at the leading edge for small α (figure 8.6(c)), the angular momentum equation (8.1) can be rewritten and solved for U^* . This yields:

$$U^* = \sqrt{\frac{2gV(d_p - d_g) \sin \theta_0}{d_g S (C_L \cos \theta_0 + C_D \sin \theta_0)}} \quad (8.5)$$

where V is the volume of the projectile.

For $U_0 < U^*$, the drag and lift torques are smaller than the stabilizing Archimedes' torque so that the initial small angle between the vertical and the projectile chord decreases: projectiles align with the vertical and we have quasi-straight trajectories. For $U_0 > U^*$, conversely,

they deviate from the vertical (its initial angle θ_0 increases). As the motion proceeds, the velocity of the projectile decreases and Archimedes' torque eventually takes over: the projectile aligns back with the vertical at the maximum depth of the dive and the motion is y-shaped.

If the center of mass of the projectile is located further from the leading edge than the point of application of the Archimedes' force ($d_g > d_p$), all torques are destabilizing. The projectile keeps deviating from the vertical: the trajectory is U-shaped.

Overall, as d_g is moved away from the leading edge, the critical velocity U^* decreases until it vanishes for $d_g = d_p$. Additionally, when the impact angle θ_0 is small, as $C_L \propto \alpha^{1.507}$ (figure 8.5(b)), it is interesting to note that the critical velocity diverges.

The equation (8.5) is plotted in blue for two different initial angles θ_0 (0.3° and 6°) in figure 8.9: as one can expect, increasing the initial angle θ_0 decreases the velocity necessary to deviate the trajectory (U^* decreased). When compared with data, one can note that although all the experimental points laying below the theoretical prediction for U^* are observed to be stable (green points), motions can be observed to be stable even for $U_0 > U^*$ (orange points).

For a fixed center of mass located close to the leading edge ($d_g < d_p$), an increase of impact velocity U_0 leads to a transition from straight to y-shaped trajectories (path (1) in figure 8.9), as observed in figure 8.3(a). Similarly, when the center of mass of the projectile is further from the leading edge (increasing (d_g/C) at fixed impact velocity, we observe a first transition from straight to y-shaped trajectories and a second transition to U-shapes (path (2) on figure 8.9), as also reported in figure 8.3(b).

In order to evaluate if the instability can develop, its characteristic growth time τ_i (time necessary for a deviation of $\Delta\theta$ from the vertical of the projectile) can be derived from a scaling analysis of the angular momentum conservation equation (8.1). Assuming $d\theta^2/dt^2 \approx \Delta\theta/\tau_i^2$, we find:

$$\tau_i = \sqrt{\frac{J\Delta\theta}{\frac{1}{2}d_g\rho S U_0^2(\cos\theta_0 C_L + \sin\theta_0 C_D) - \rho g V \sin\theta_0(d_p - d_g)}} \quad (8.6)$$

To evaluate the characteristic time of the fall τ_f , we suppose that the motion is straight and that the projectile is only subjected to drag [129]. Integrating the force balance, we get:

$$U(t) = \tilde{U} \sqrt{\frac{1-\bar{\rho}}{\bar{\rho}}} \tan\left(\arctan\left(\frac{U_0}{\tilde{U}} \sqrt{\frac{\bar{\rho}}{1-\bar{\rho}}}\right) - \frac{1-\bar{\rho}}{\bar{\rho}} \frac{g}{\tilde{U}} t\right) \quad (8.7)$$

where $\tilde{U} = \sqrt{\frac{2gm}{\rho S C_D}}$ is the characteristic velocity of the fall and $\bar{\rho}$ the relative density of the projectile. As $U(\tau_f) = 0$, using 8.7, we find τ_f to be:

$$\tau_f = \frac{\tilde{U}}{g} \frac{\bar{\rho}}{1-\bar{\rho}} \arctan\left(\frac{U_0}{\tilde{U}} \sqrt{\frac{\bar{\rho}}{1-\bar{\rho}}}\right) \quad (8.8)$$

Using equations (8.6) and (8.8), the ratio τ_i/τ_f is computed and plotted when equal to 1 for $\Delta\theta = \pi/2$ in figure 8.9 for different values of the impact angle θ_0 . Below this curve, we have $\tau_f < \tau_i$ and the instability has no time to develop: the motion, when unstable, can however follow a straight trajectory - a regime that corresponds well with the orange data. This is the case for $d_g/C = 18\%$ and $U_0 = 1.8 \text{ m/s}$, where the trajectory is experimentally found stable (figure 8.1(a)) but numerically unstable (figure 8.8(a)).

8.3.3 Quantitative comparison and dive depth

Quantitatively, one experimental trajectory of each type is fitted with the corresponding numerical solution of the equations of motion in figure 8.10. For straight (figure 8.10(a)), Y-shaped (figure 8.10(b)) and U-shaped (figure 8.10(c)) trajectories, the overall shape of the numerical solution, as well as the maximum depth and the maximum horizontal distance travelled, are in good agreement with the observed trajectories. The small discrepancies observed for the Y-shape and the U-shape can be attributed to the fact that the only fitting parameter is the initial angle θ_0 .

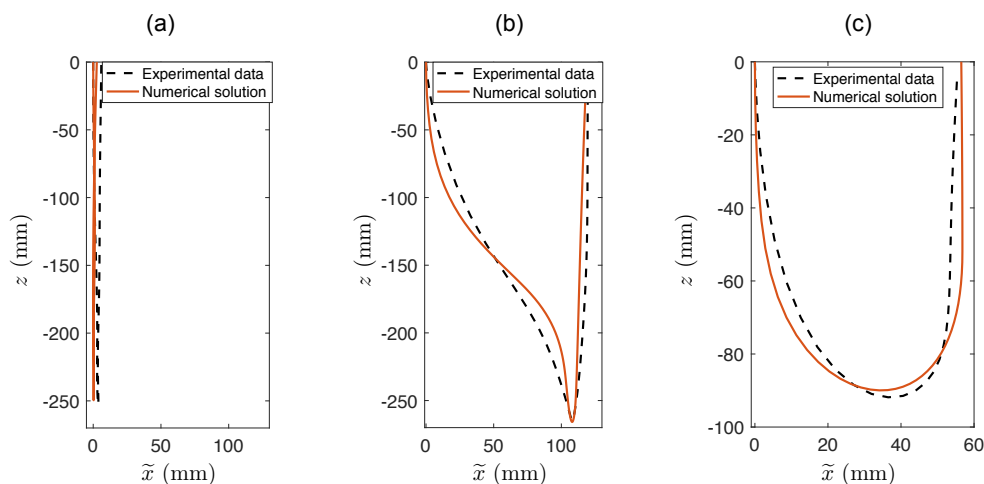


Figure 8.10: Trajectories of the center of mass of different projectiles. Solid line is the numerical solution of the equation of motion and the dashed line is the experimental trajectory. The fitting parameter for the numerical solution is the angle θ_0 between the vertical and the chord of the projectile at impact. (a) Straight trajectory for $d_g/C = 18\%$ and $U_0 = 0.94$ m/s. $\theta_0 = 2^\circ$. (b) Y-shaped trajectory for $d_g/C = 27\%$ and $U_0 = 1.25$ m/s. $\theta_0 = 9^\circ$. (c) U-shaped trajectory for $d_g/C = 44\%$ and $U_0 = 0.95$ m/s. $\theta_0 = 5.5^\circ$.

The depth h of the dive, can be determined numerically when the impacting velocity U_0 is varied for a range of impacting angle θ_0 and it is plotted in colored area in figure 8.11. The predicted depth is compared with data for different positions of the center of mass d_g . The agreement is good, except when an air cavity is entrained, an ingredient not present in the model -the dive depth in this case being naturally found to be significantly smaller than predicted.

To further understand the saturation in depth reached by the streamlined projectile, we can obtain the theoretical variation of depth of a projectile z_g with time t by integrating equation 8.7:

$$\frac{z_g(t)}{\mathcal{L}} = \log \left\{ \cos \left[\arctan \left(\frac{U_0}{\tilde{U}} \right) - \frac{1 - \bar{\rho} g t}{\bar{\rho}} \frac{g t}{\tilde{U}} \right] \right\} \quad (8.9)$$

where $\mathcal{L} = \frac{2m}{\rho S C_D}$ is the characteristic length of the dive. This relation can be evaluated in $t = \tau_f$ to get the maximal depth of a straight dive, which is plotted in dotted line in figure 8.12. Furthermore, once the instability is established, the maximum depth of the dive will rather be set by τ_i , so that we expect $h \sim z_g(\tau_i)$. This distance is plotted in dashed line in figure 8.12. Finally, we can notice that the curve $z_g(\min(\tau_i, \tau_f))$ matches well both the numerical and experimental data.

Therefore, we can conclude that: First, when $\tau_f < \tau_i$, the motion is stable, the trajectory is quasi-straight and the maximum depth is $z_g(\tau_f)$. Second, when $\tau_f > \tau_i$, the instability has

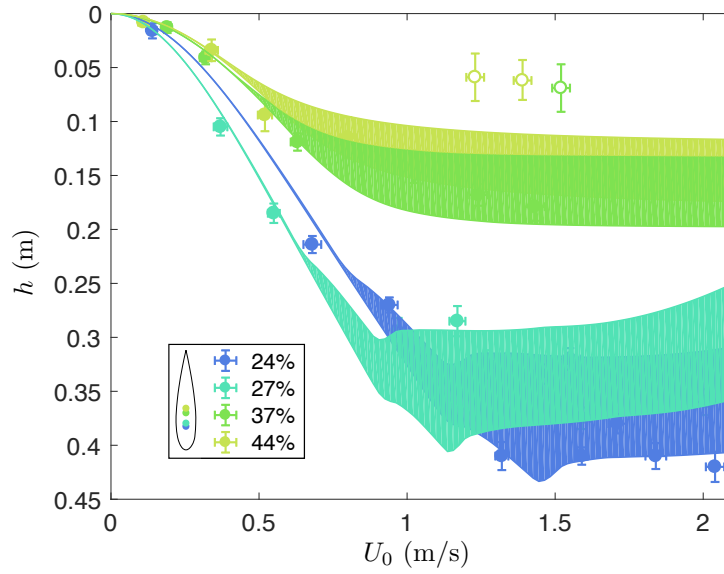


Figure 8.11: Comparison between the numerically predicted depth h of the dive and experimental data. Shaded areas are the numerically determined depths for impacting angle θ_0 ranging from 0.3 and 6 degrees. Filled dots are experimental data for different positions of the center of gravity and mass of the projectile when no cavity is formed at the water entry: $d_g/C = 24\%$, $m = 6.7$ g, $d_g/C = 27\%$, $m = 6.85$ g, $d_g/C = 37\%$, $m = 6.32$ g, $d_g/C = 44\%$, $m = 6.4$ g. Empty dots are experimental data for projectile entraining an air cavity at water entry.

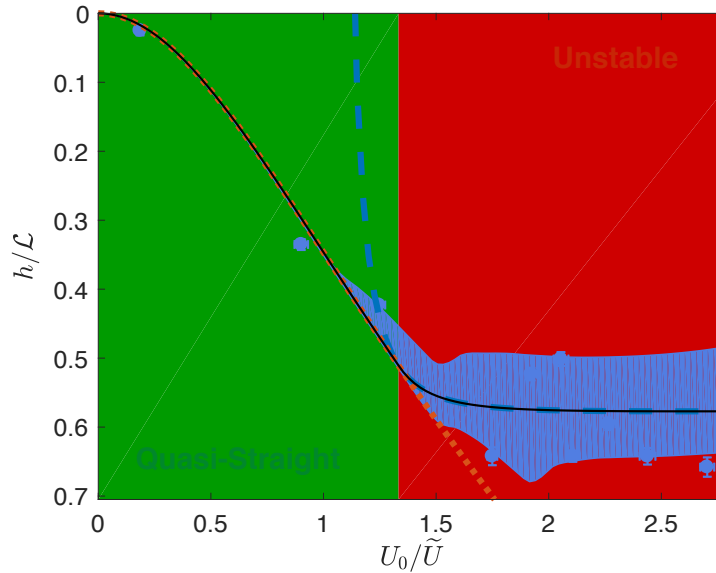


Figure 8.12: Comparison between the theoretical prediction for the dive depth and both numerical and experimental data. Shaded areas are the numerically determined depths for impacting angle θ_0 ranging from 0.3 and 6 degrees. Filled dots are data for a center of mass located at $d_g/C = 24\%$ and a mass $m = 6.7$ g. Dotted line is the theoretical maximum depth of the dive for a straight trajectory, *i.e.* $z_g(\tau_f)$ using equation 8.9. Dashed line is the theoretical depth $z_g(\tau_i)$ of a straight dive reached at the time τ_i at which the instability has developed. Solid line is $z_g(\min(\tau_i, \tau_f))$

time to grow, the projectile has y-shaped or U-shaped trajectory and the maximum depth of the dive is $z_g(\tau_i)$.

8.4 Controlling the instability

Controlling the instability to obtain a straight trajectory is crucial in most applications and it should technically be achieved by adding fins near the trailing edge of the projectile. To test this hypothesis, we evenly place four fins around the projectile at a distance d_f from its leading edge. Each fin has a fixed chord $C_f = 1$ cm and its span l is varied from 0 to 25 mm as show in figure 8.13(a).

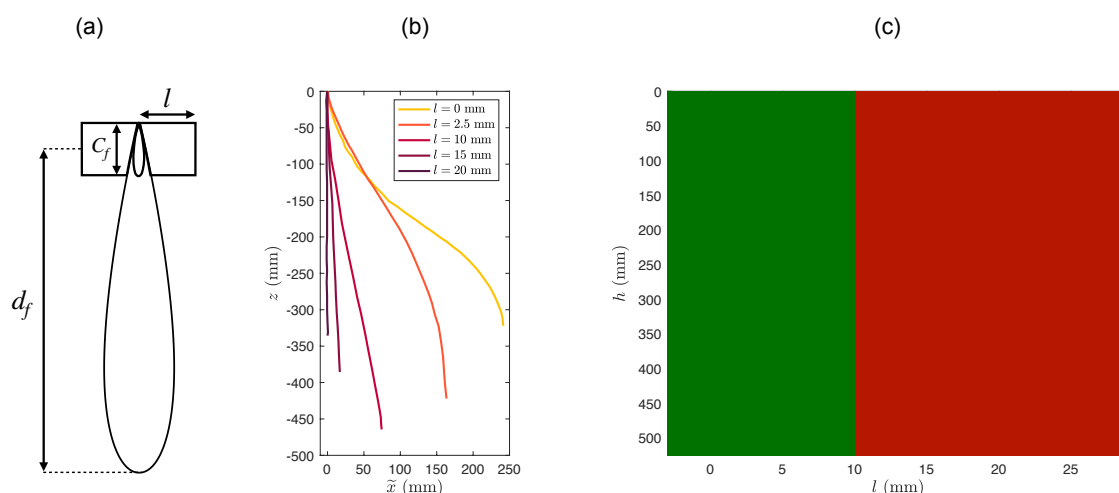


Figure 8.13: (a) Sectional drawing of the projectile with four fins. Fins are evenly placed around the projectile at a distance d_f from the leading edge. Each fin has a span l ranging from 0 to 25 mm and a chord $C_f = 1$ cm. (b) Experimental trajectories for a projectile with fins of span ranging from 0 to 20 mm. The position of the center of mass of the projectile is fixed at 27% of the total chord and its mass is $m = 6.6$ g. The impact velocity is $U_0 = 1.2$ m/s. (c) Depth of the dive h as a function of the span of the fins l . The position of the center of mass of the projectile is fixed at 27% of the total chord and its mass is $m = 6.6$ g. The impact velocity is $U_0 = 1.2$ m/s.

Figure 8.13(b) displays five trajectories up to their maximum depth of a projectile with fins of increasing span. With no fins ($l = 0$ mm), we recover the y-shape trajectory previously described. When increasing the span of the fins the trajectory becomes closer to the straight line, indicating that we effectively controlled the instability by adding fins. However, when increasing l , the maximum depth h increases from ~ 320 mm to a maximum value of ~ 500 mm for $l = 10$ mm before decreasing to ~ 300 mm for $l = 25$ mm as shown in figure 8.13(c).

Similarly as for equation 8.5, we can derive an expression for the critical impact velocity U_l^* above which the projectile trajectory is unstable. Writing the aerodynamics coefficients of the fins C_{D_f} and C_{L_f} , we define a characteristic length of the fins

$$l^* = \frac{d_g S (C_L \cos \theta_0 + C_D \sin \theta_0)}{4(d_f - d_g) C_f (C_{L_f} \cos \theta_0 + C_{D_f} \sin \theta_0)} \quad (8.10)$$

such that U_l^* simply writes:

$$\frac{U_l^*}{U^*} = \sqrt{\frac{1}{1 - \frac{l}{l^*}}} \quad (8.11)$$

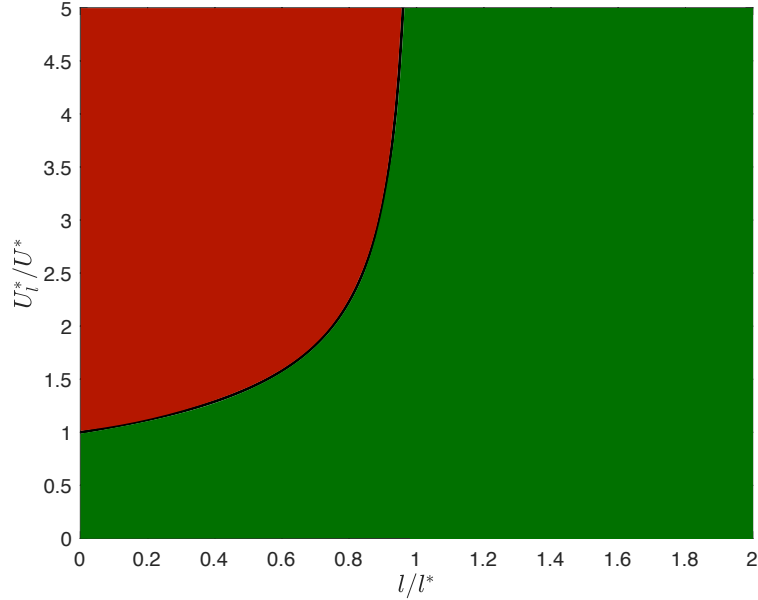


Figure 8.14: Critical impact velocity U_l^* above which a projectile with four fins of span l have a non-straight trajectory. U^* is the critical velocity without fins and l^* the span of the fins above which the trajectory will always be stable.

For $d_f < d_g$, $U_l^*/U^* < 1$ meaning that the fins destabilize the trajectory of the projectile. For $d_f > d_g$, the fins are stabilizing and as $l^* \propto 1/\sqrt{d_f - d_g}$, their stabilizing effect will grow as the fins are placed closer to the trailing edge of the projectile. For $d_f > d_g$, the relation 8.11 is plotted in figure 8.14. The first interesting feature of this curve is that for fin bigger than l^* , independently of the impact velocity U_0 , the trajectory will always be straight. The second noticeable feature is that for a fixed impact velocity $U_0 > U^*$ correspond a minimal span l_{opt} , smaller than l^* , for which the trajectory is stable (*e.g.* $l_{opt} \approx 0.8l^*$ for $U_0 \approx 2U^*$). If a span greater than l_{opt} is chosen, the trajectory will still be straight but the drag of the projectile will increase and hence the depth of the dive h will be reduced as observed in figure 8.13(c).

Take home message of Part 8

- 1. Three trajectories can be observed:** straight trajectory (stable), Y-shape trajectory (unstable) and U-shape trajectory (unstable). The depth of the dive is reduced when the trajectory is unstable.
- 2. The instability is driven by the torque of the lift force** whereas Archimedes's torques stabilizes the trajectory.
- 3. The morphology of the trajectory is determined by the impact velocity U_0 and the position of the center of mass d_g of the projectile.** For center of mass located close to the leading edge ($d_g < d_p$), a critical velocity U^* exists, above which the projectile follows a Y-shape trajectory. For center of mass located far from to the leading edge ($d_g > d_p$), the projectile follow a U-shape trajectory no matter what the impact velocity is.
- 4. Instability can be controlled adding fins near the trailing edge of the projectile.** Above a characteristic span l^* of the fins, the trajectory will always be stable. However, for a fixed impact velocity U_0 , there is an optimal span $l_{opt} < l^*$ such that the trajectory is straight and the drag coefficient of the resulting projectile is the smallest.



CONCLUSION

In this thesis we address the question of how cavitation can turn a bluff body into a stable streamlined projectile. In particular, we wish to determine if cavitation alone could make a submarine travelling at 100 m/s possible. A body moving underwater is surrounded by a region of low pressure in its wake. If the projectile is travelling fast enough, the pressure drop can trigger cavitation, that is, the phase change of the liquid to gas. A further increase of the projectile velocity eventually leads to the formation of a large gas bubble: the so-called supercavitation regime. This bubble induces a modification of the drag of the projectile which, under certain circumstances, makes it analogous to a streamlined projectile. To investigate this phenomenon, we first report, in Part I, the study of the initial growth of a cavitation bubble. We then concentrate, in Part II, on measuring the drag reduction that can be achieved with supercavitation and we finally derive, in Part III, the conditions for a streamlined projectile to have a straight trajectory.

Cavitation bubble dynamics is an experimentally difficult problem to address if the pressure drop is only generated by a steady velocity: this is due to the fact that velocities needed for cavitation bubbles nucleation are typically larger than 20 m/s at atmospheric pressure. However, cavitation of a fluid can easily be observed when the fluid is accelerated. Simply impacting a container filled with water with a hammer can trigger pressure drop of several bars. In Part I, we used this phenomenon to study the growth of a cavitation bubble in a transient pressure field. A short review of previous work on this topic is made in Chapter 1. To address this question, we built a drop-tower, described in Chapter 2, which allowed us to have reproducible impacts of high acceleration on a water container. We showed theoretically and experimentally that a pressure drop is indeed generated in the area opposite to the point of impact and that its magnitude is proportional to both the size of the container and the acceleration of the tank. This pressure drop eventually triggers the phase transition of the liquid water into gas. In Chapter 3, we showed that the radius of the cavitation bubble created has a dynamical evolution which follows the classical Rayleigh-Plesset equation. As the pressure drop is transient, the bubble rapidly collapses: we observed bubbles which typically had a life expectancy of a few tens of milliseconds and reached centimetric maximum radius. The collapse of the bubbles is a fast process which has been shown to be responsible for damages on nearby surfaces: for instance, it is known to be the main mechanism involved in boat propellers aging. The energy released through this process can be directly linked to the maximum radius of the bubble. We analytically derived an expression for the value of the maximum radius of a bubble in a transient pressure drop. The whole study can be used to improve the understanding of material aging induced by cavitation but also to investigate the causes of traumatic brain injuries, also known as brain concussion in sports. Indeed, the container filled of water is analogous of a cranial vault and the shock we imposed is similar to the impact that could be received during boxing. We showed in Chapter 3 that we can predict the damaging potential of a cavitation bubble in the head and that it is in a good agreement with the heuristic medical observations. These results prove that cavitation is a relevant mechanism to consider for brain concussion and they are encouraging as they could lead to an improved detection and prevention of the brain concussion. However, a lot of questions are still open and need to be tackled to prove the implication of cavitation in the damaging process of the brain. Experimentally, it would be interesting to evaluate the damaging potential of a bubble on a material similar to the brain. For instance, this material could be a cell layer, a brain slice or a polymer of the same mechanical properties. Theoretically, the influence of the confinement of the bubble on its dynamic is yet to be determined: as an incompressible flow in a planar geometry does not vanish at infinity, the time evolution of the bubble radius cannot be derived from Rayleigh-Plesset equation. Finally, in-situ recording of cavitation bubbles would definitely prove that the phenomenon should be taken into account in the brain damage process. To do so, one could identify the noise generated by the collapse

of a cavitation bubble following a shock on the head of a boxer or rugby player. The same process was recently used to identify cavitation as the mechanism of knuckle cracking [69]. Finally, this work on cavitation under acceleration in confined environments opens the perspective of a new way to generate the phase transition, which could facilitate the entry in the supercavitation regime. This work could directly be applied to model the launch of fast travelling objects underwater, for instance torpedoes, which begin their trajectories accelerating in a confined environment.

Drag modification in the supercavitation regime can be evaluated in a standard hydrodynamic tunnel replacing the vapor production due to cavitation by an artificial air injection. The cavity created is referred as a ventilated cavity. In Part II, we investigate the modification of the drag induced by a ventilated cavity behind a sphere near its drag crisis. In chapter 4, we briefly reviewed the literature on this subject. To tackle this problem, we developed a hydrodynamic tunnel, presented in Chapter 5, that allows us to measure the drag on a sphere while injecting air at a constant rate in its wake. Additionally, we used spheres of different roughness to study the influence of the ventilated cavity on the drag crisis. We showed in Chapter 6 that the dimensions of the bubble created are uniquely determined by the dimensionless air injection rate. This number compare the volumetric air injection rate to the volumetric water flow rate based on the frontal area of the projectile. In particular, for high dimensionless air injection rate (> 0.04), a unique bubble was found to pin at the equatorial plane of the sphere. This bubble is nearly cylindrical and its length was measured to be proportional to the dimensionless air injection rate. This behaviour was shown to be caused by the growth of perturbation at the interface of the bubble. We also measured the drag of the resulting system: in the high dimensionless air injection rate regime (> 0.04), we found that the drag was proportional to the dimensionless injection rate to the power $(-1/3)$. As a consequence, we could measure drag reductions up to a factor 50% in our experimental configuration for the largest bubbles. This result also suggests that we could reach even higher drag reductions by increasing the air injection. However, we also showed that the air injection in the vicinity of the projectile does not always lead to a drag reduction. In particular, when the water flow around the sphere is supercritical (at Reynolds number above 10^6 for a smooth sphere), the wake of the sphere is thin and the boundary layer detaches near the back of the sphere. Injecting air at the back of the sphere in this regime results in a perturbation of the supercritical wake leading to a drag increase (up to a factor 5). While the results presented in Chapter 6 suggest that a submarine, even in the supercavitation regime, could not reach 100 m/s, several open questions should be addressed before ruling out this possibility. Theoretically, most previous work to predict the drag of supercavitating bodies are based on the potential flow theory and cannot account for the complexity of the drag crisis. The complexity of the interactions of the injected air with the wake could be approached using numerical models. Experimentally, it was shown, in a different system, that drag coefficient of a sphere with a gas bubble in its wake could be as low as 0.05 [92]. To achieve this ground breaking value, our experimental set-up should be improved to limit the growth of perturbations at the interface of the bubble. The resulting bubble pinch off at a stable point. Among all the possible improvements, we identified the most important as: the reduction of the turbulence of the water flow, the limitation of the influence of the holder on the flow around the sphere and the use of smooth spheres to avoid constraining the pinning point of the bubble.

Stability of the trajectory of a streamlined body is crucial to predict the final destination of the projectile. We showed, using air injection, that a supercavitating projectile can reach drag coefficients as low as the one measured for streamlined bodies. To study the trajectories of such projectiles, we simplified this system, in Part III to a floating streamlined projectile with an inhomogeneous mass distribution. We focused on the trajectory of such projectiles following an impact on water. To do so, in chapter 7, we briefly reviewed the

available literature and presented the experimental set-up we developed to impact projectiles at variable and nearly vertical velocity on water. We demonstrated both theoretically and experimentally in Chapter 8 that three families of underwater trajectories could be observed: straight, U-shaped, y-shaped. Although only the first type of trajectory was considered stable, all families share the same overall behaviour: the projectile slows down after its impact, reaches a maximum depth and then moves back to the surface. The instability which results in the U-shaped and y-shaped trajectory is driven by the torque of the lift force on the projectile while Archimedes's torque stabilizes the trajectory. As a consequence, for a given shape of the projectile, the transition between the stable and the unstable regime depends on the position of the center of mass of the projectile and its impact velocity. Hence, for a center of mass located near the leading edge, the projectile is stable for an impact velocity below a critical velocity. Above this velocity, the trajectory was observed to be y-shaped. For a center of mass located far from the leading edge, the trajectory will always be unstable and U-shaped. After measuring in separated experimental set-up the different aerodynamic properties of the projectile (aerodynamic coefficients, position of the aerodynamic center), we were able to analytically predict the shape of the trajectory and the maximum depth of the dive, which was found to be reduced when the trajectory is unstable. Further taking into account the growth time of the instability, we were able to capture the experimental observations of the transition between the different families of trajectories. Finally, we showed that the stability of the trajectory can be ensured by adding fins near the trailing edge of the projectile. Such fins can be design to unsure stability either up to a certain velocity or for all impact velocity. In the latter case, large fins are used which results in a increase of the drag and a reduction of the depth of the dive. Even though we propose, in Part III, several techniques to unsure stability, it does not provide any explanation on how gannets, or other diving birds, control this instability and can reach their target. Our hypothesis, is that gannets dive with a horizontal component of the velocity. In this manner, they impose the plane of instability and they can prevent the instability from growing only with their feet, which act as unidirectional fins. This hypothesis should be tested with projectile impacting water with an initial horizontal velocity equipped with unidirectional fins. Finally, we could get back to the initial system of a bubble pinned to a projectile, which raise two questions: What is the dynamic of the bubble when it is not aligned with the flow? Can the bubble exert a torque on the projectile? These questions remain open and would necessitate rethinking both experimental set-up presented in Part II and III to be tackled.



Арх

APPENDICES

A

LIST OF PUBLICATION

The Path Instabilities of Streamlined Bodies, T. Guillet, M. Coux, D. Quéré and C. Clanet, *Journal of Fluid Mechanics* 864 (2019): 286-302.

Analytical criterion for traumatic brain injuries, T. Guillet, J. Amauger, P. Decq, D. Quéré, C. Cohen and C. Clanet (submitted).

Drag modification induced by a ventilated cavity near the drag crisis of a sphere, T. Guillet, D. Quéré, C. Cohen and C. Clanet (in preparation).

Critical density for the stability of a 2D magnet array, C. Reiss, F. Bastit, D. Sulem, A. Bacot, L. Cousin, P. Goux and T. Guillet, *Emergent Scientist* 2 (2018).

From the microstructure of steels to the explosion of sparks, A. Guillen, F. Goh, J. André, A. Barral, C. Brochet, Q. Louis and T. Guillet, *Emergent Scientist* 3 (2019).

Motion of rain drops on a car side window, J. André, C. Brochet, Q. Louis, A. Barral, A. Guillen, F. Goh, A. Prieto and T. Guillet, *Emergent Scientist* 3 (2019).

Sound of a nut rolling inside an elastic rubber balloon, A. Barral, Q. Louis, C. Brochet, J. André, A. Guillen, F. Goh, A. Prieto and T. Guillet, *Emergent Scientist* 3 (2019).

B

INTERNATIONAL PHYSICISTS' TOURNAMENT

I had the chance to be Team Leader for the team representing École polytechnique at the International Physicists' Tournament. To prepare for the tournament, a team of 6 students have to work on 13 to 17 physics research problems for 8 months. The problems cover a wide range of different topics from fluid mechanics to electromagnetism and always have an experimental component. During the tournament, the students have to present their solution and debate on how it could be improved with other teams. I followed three groups over my PhD and they ended up at the third position in 2017, the second position in 2018 and first in 2019: one could say that it is moment to retire!

After the tournament, we also encouraged students to have their first experience on peer-reviewed publishing: some of their work has been published in *Emergent Scientist*. This appendix present an example of such article entitled "Sound of a nut rolling inside an elastic rubber balloon".

Sound of a nut rolling inside an elastic rubber balloon

Amaury Barral^{1,*}, Quentin Louis^{1,**}, Clément Brochet¹, Julie André¹, Anthony Guillen¹, Fang Goh¹, Angel Prieto¹, and Thibault Guillet²

¹ Ecole Polytechnique, 91128 Palaiseau Cedex, France

² LadHyX, UMR 7646 du CNRS, Ecole Polytechnique, 91128 Palaiseau Cedex, France

Received: 4 July 2018 / Accepted: 14 June 2019

Abstract. This article studies the sound produced by nuts of different shapes swirling in an elastic rubber balloon. First, the sound is studied experimentally, both in terms of frequency and amplitude. Regarding the frequency components of the sound, we show that they can be divided into two main contributions – one due to the oscillations of the elastic membrane, the other due to the hits of the nut against the balloon – and present models to describe the frequency's dependence on the main parameters of the system. We analysed the influence of several parameters such as the balloon's geometry, the nut's geometry and its mass.

1 Introduction

The study of spherical elastic shells probably started at the end of the 19th century with the theoretical studies of Lamb [1,2]. Several refined theoretical studies have focused on determining the eigenfrequencies (and the amplitude) of such systems [3,4]. Works on spherical shells have also tackled the problem numerically [5,6] and more complex work has appeared such as the study of instabilities of expanding and contracting shells [7].

Using large elastic balloons and the reflection of a laser on the surface of its membrane, Kuo et al. [8] observed these frequencies experimentally. Using an improved model from the previous literature, they were able to show good agreement between theory and experiments.

Nonetheless these previous studies are in majority theoretical and the experimental studies only focus on the frequency response of the vibrations of the membrane generated by a precisely controlled excitation. Hence, the study of more complex phenomenon is left open.

In this article, using different types of nuts (and coins) made to rotate inside an elastic rubber balloon, we investigate both the frequency content and the amplitude of the sound produced by the internal periodical excitation (produced by the rolling of a nut).

First, we present the different experimental methods and the theoretical models for the frequency components. Then, we report our experimental results and finally discuss the agreement between those experiments and our predictions.

* e-mail: amaury.barral@polytechnique.edu

** e-mail: quentin.louis@polytechnique.edu

2 Experimental method

2.1 Experimental setup for sound capture and analysis

In most of the experiments, hex nuts were used. However, we also investigated nuts with several other shapes and report results for coins as well.

A nut of side length l (with a total of N sides), width e and mass m (see Fig. 1a) is inserted in a new (non-inflated before) transparent commercial rubber balloon (Nuolux 12 inches white latex balloons). The balloon is inflated by a human operator and tightly closed by pinching the nozzle, allowing it to be reopened and inflated further. Once inflated, the new dimensions of the balloon are measured on ruler-calibrated pictures. As in Figure 1b the human operator then gives the balloon a circular translation movement, inducing the swirling of the nut inside the balloon.

The sound is recorded using a calibrated-response microphone (Shure SM57) at a fixed distance from the center of the balloon, facing the side of the balloon, the motion of the nut is captured by a high-speed camera (Photron FASTCAM SA at 3000 fps) and a regular reflex camera (Canon EOS 700D) is used for pictures and 30 fps videos. A schematic view of the experimental setup appears in Figure 1c.

The sound is analysed via its Fourier transform from Audacity 2.2.1 with size 65536 using a Hanning window, on samples of a few seconds. Temporal Fourier Transform and Amplitude calculations are also performed using Python. A typical Fourier transform and its integrated PSD (Power Spectral Density) are shown in Figure 2. Sound occurs through all the spectrum but

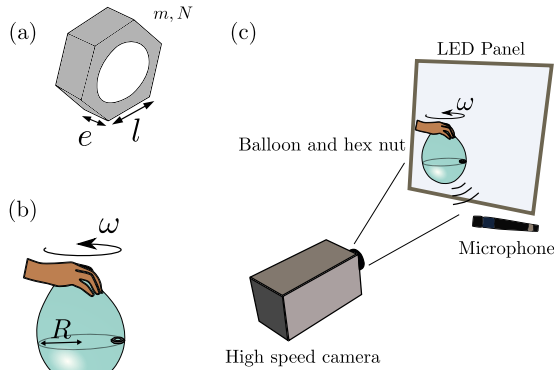


Fig. 1. Experimental setup and nomenclature. (a) Sketch of the hex nuts used in experiments. A nut is characterised by its number of sides N , its side length l , its width e and its mass m . (b) Close sketch of the balloon, characterised by its radius R and its rotating speed ω . (c) Sketch of the experimental setup.

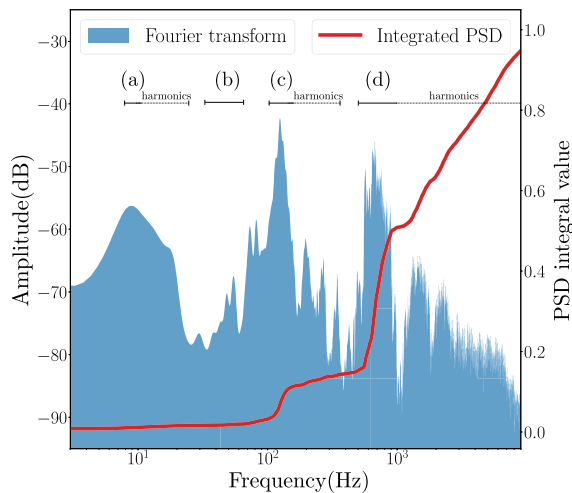


Fig. 2. Typical Fourier transform. In this case, the experimental conditions were: $N = 6$, $m = 0.3$ g, $l = 2.7$ mm, $e = 2.4$ mm, $f_{rot} = 3.7$ Hz and $R = 9.8$ cm. Four identifiable zones (a), (b), (c), (d). Only (c) and (d) are audible as showed by the PSD (Power Spectral Density) integral. (a) Is the macroscopic sound produced by the balloon pushing air during its movement. (b) Is the sound components ranging from 30 to 80 Hz. (c) Is the first eigenfrequency of the membrane. (d) Is the frequency produced by the nut rolling and hitting the membrane. Harmonics are also produced.

the higher frequencies are the only ones audible (in most cases), which the PSD integral confirms as its slope changes abruptly. The sound can be divided into four parts: two low frequency parts (3–6 Hz and 40–80 Hz), a medium frequency part (100–200 Hz) and a higher

frequency part that is much more variable depending on the characteristics of the nut (200–2000 Hz).

2.2 Assumptions of our model

2.2.1 Influence of gravity

Changes in the nut's height during its trajectory lead to changes in its velocity and thus in the sound we hear. Assuming this change to be 10% (from the horizontal plane) of the balloon's radius and with an initial speed of $1\text{--}3$ ms^{-1} , taking the condition $\Delta v/v < 0.1$ where v is the speed of the nut at the center height of the balloon and Δv is the difference between the speed of the nut at the highest point of the trajectory and at the middle of the balloon, we get $gR/v^2 < 1$ where R is the radius of the balloon and g is the acceleration of gravity, which yields $R < 20$ cm (experimentally R varies between 3 cm and 15 cm).

We can therefore safely neglect the influence of gravity in our experiments.

It is useful to note that even if gravity had a non negligible influence, it would just broaden the spectrum of frequencies around the gravity-less value, which only increases error bars.

2.2.2 Influence of inertial forces

Balloons are not perfectly spherical, they are rather pear shaped. This change in their radius induces a change in the inertial energy of the nut $E = \frac{1}{2}m\omega^2R^2$. Taking the condition $\Delta v/v < 0.05$ gives $\Delta R < 0.05v^2/R\omega^2$ where R is the radius of the balloon at the center of the balloon, ΔR the change in radius during the trajectory, v the speed of the nut, $\omega = 2\pi f_{rot}$ the rotation pulsation of the nut, which for our typical setups gives $\Delta R < 6$ cm across the trajectory of the nut (experimentally ΔR is of the order of a few cm at most).

We can therefore safely neglect the influence of uncontrolled changes in the inertial force in our experiments.

Even if changes in the inertial force had a non negligible influence, it would be equivalent to greater uncertainties in the measure of the balloon's radius.

2.2.3 Influence of the Doppler effect

The relative frequency shift induced by the Doppler effect is $\Delta f/f = v/c$ where v is the speed of the nut and c is the speed of sound in air. We consider it negligible for $\Delta f/f < 0.01$ which gives us $v < 3$ ms^{-1} . Typical speed ranges in our experiments are $1\text{--}3$ ms^{-1} .

We can therefore safely neglect the influence of the Doppler effect in our experiments.

2.2.4 Influence of friction

Experiments show that the nut does not slide on the membrane of the balloon, and that changing the friction coefficient by adding oil (which dramatically reduces friction) has no significant influence on the sound emitted, which leads us to affirm that friction is not an important parameter in this problem. This allows us to use a no-slip model to predict the primary frequency.

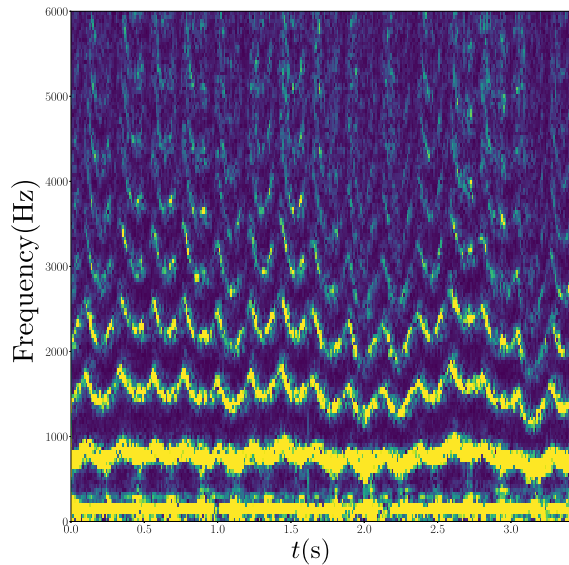


Fig. 3. Spectrogram of a typical audio record of 3 seconds. Experimental conditions are identical to Figure 2. Frequency components are plotted as a function of time. The ladder of intensity goes from dark blue (no frequency component) to yellow (important frequency component). The amplitude modulation is represented by the alternation of bright (yellow) and dark zones. Oscillations of the harmonics of the main frequency (~ 800 Hz) with the same periodicity as the amplitude modulation are also visible.

2.3 Rotational frequency of the nut

Within our range of speeds and dimensions, the frequency at which the nut rotates is equal to the frequency at which the amplitude is modulated.

Since the amplitude of the sound received depends on the distance between the nut and the microphone (which varies significantly during the experiments as the nut goes from one side of the balloon to the other) we observe a modulation frequency on the spectrograms. The periodicity of the spectrogram in Figure 3. is theoretically equal to the rotation frequency of the nut. This is experimentally checked using a camera.

2.4 Measurement of elastic properties

The elastic properties (the Young's Modulus and Poisson's ratio) of commercial rubber balloons are not specified and need to be determined experimentally. To do so, we cut bands of known dimensions from new balloons and stretch them while measuring the force required to do so. We also measure the thickness/width of the band during the stretching experiment. The Young's modulus of a band of length l is defined by $E = \sigma/\epsilon$ where σ is the stress (force/surface) applied and $\epsilon = \Delta l/l$ is the relative elongation of the band. Poisson's ratio ν is defined by the amount of transverse expansion divided by the amount of axial contraction.

In our experimental conditions, we are not in the elastic regime on the whole strain curve. However, once the balloon is inflated, the slope of the strain curve around the inflation deformation is locally constant, and we can define a local Young's modulus for a given deformation. The additional deformations of the inflated balloon during the experiments, either due to the hex nut pushing on the membrane or to waves travelling in the membrane, are small enough to justify that this approximation holds.

2.5 Measurement of the main sound frequency – nut hits on the membrane

The primary sound's frequency produced is measured by taking the frequency corresponding to the main component in the spectrogram.

2.6 Measurement secondary sound frequency

In experiments appear a rather constant frequency that can be heard in some remote cases between 100 and 200 Hz. We measure this frequency by taking the highest amplitude component between 100 and 200 Hz in the spectrogram.

2.7 Measurement of the amplitude amplification

Due to its shape and oscillating properties we expect the balloon to act as a sound box, amplifying the sound produced by the nut.

To measure this amplification we measure the sound produced by a piezoelectric transducer in the air at a given frequency, then compare it to the sound produced when a balloon is attached to the transducer under the same conditions. The difference in amplitude between the two experiments gives us the amplification for that frequency. We then obtain a continuous graph by sweeping between frequencies.

The amplitude considered here is the total amplitude of the sound, with all its frequencies.

2.8 Measurement of the amplitude of the main sound

Since the primary sound is the one with the highest fundamental frequency and does not overlap with other sound contributions in the studied frequency range, we extract its amplitude from the Fourier transform by integrating the peaks from 80% of the fundamental frequency (to account for the peaks width) to infinity.

3 Models

3.1 Predicted main sound frequency – nut hits on the membrane

The primary sound produced is due to the nut deforming the membrane and creating a pressure wave at a given frequency. The frequency at which a nut of side length l rolling without friction at a speed v hits the balloon is $f_{pred} = v/l$. Harmonics are also generated by the deformation.

3.2 Predicted secondary sound frequency – membrane vibration

A rubber balloon is an elastic medium with periodic boundary conditions, we thus expect it to have specific eigenfrequencies at which the membrane is going to oscillate and create a sound.

Following Baker [3] we model our balloon as a simple spherical elastic shell. Its eigenfrequencies are given by

$$f_n^2 = \frac{\alpha \pm \sqrt{\alpha^2 - 4(1 - \nu^2)[n(n+1) - 2]}}{2G}$$

where $\alpha = n(n+1) + 1 + 3\nu$, $G = \frac{(1 - \nu^2)\rho R^2}{E}$. R is the radius of the balloon, E, ν are its Young's modulus and Poisson's ratio respectively, and ρ is the rubber's density. The \pm sign yields two branches of eigenfrequencies, thereafter named *lower branch* and *upper branch*.

More simply, we can derive the dependency of the frequency in $1/R$ with a simple rope model. Assimilate the balloon sphere to a rope of length $L = 2\pi R$ with periodic boundary conditions. The wavelengths λ will be quantified, proportional to L/n where $n \in \mathbb{Z}$. Therefore, $f = c_{el}/\lambda \propto 1/R$ where c_{el} denotes the speed of sound in the elastic material.

4 Results

4.1 Influence of solid friction

The movement of the nut on the membrane is circular as Figure 4a shows that its corners' motion is sinusoidal. The chronophotography in Figure 4b confirms this rolling behaviour: when the nut topples over, its corner in contact with the membrane does not slide.

4.2 Rotational frequency of the nut

The frequency of the modulation of amplitude is plotted against the rotational frequency of the nut (captured by video) in Figure 5.

4.3 Elastic properties

Traction curves such as in Figure 6 give us an estimate on the Young's modulus of our balloons of 1–3 Mpa. Regular measurements of the thickness/width of the membrane give a Poisson's coefficient between 0.4 and 0.5, within expected ranges (theoretical value 0.5 for an elastic medium).

4.4 Main frequency – nut hits on membrane

We determine the primary frequency of the sound as a function of the radius of the balloon, the side length of the nut and its rotation frequency inside the balloon. The theoretical frequency is plotted against the experimental frequency in Figure 7.

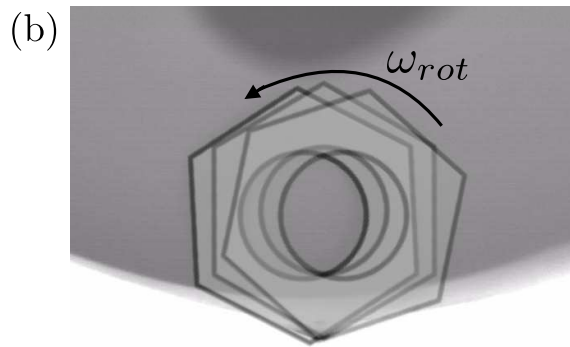
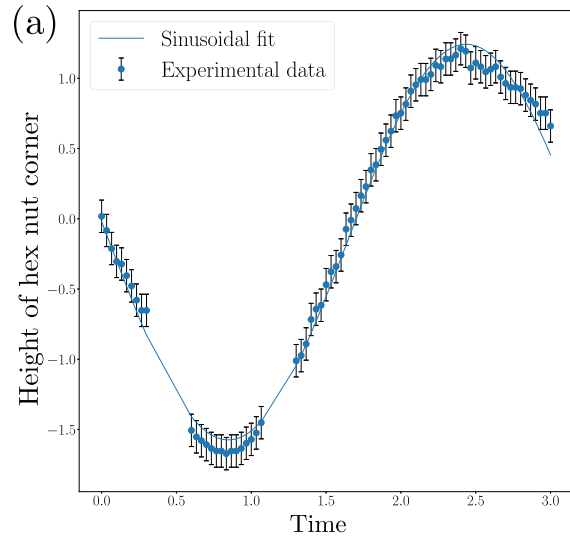


Fig. 4. (a) Experimental data of the height of a corner of the nut during one rotation of the nut extracted using Tracker (software). A sinusoidal fit is performed on the experimental data and plotted in solid line. (b) Superposition of three images of the nut rolling on the membrane taken with a high-speed camera at 3000 fps. For visualisation purposes the hex nut is redrawn.

We found no influence of the mass and width of the nut on this frequency.

4.5 Secondary frequency – membrane vibration

Using a high-speed camera at 3000 fps, we observe vibrations on the surface of the membrane. The absence of either visible nodal points or asymmetrical motion indicates that the fundamental mode is dominant as described in the model we used [3].

We determine the frequency of the sound produced by the membrane in function of the radius of the balloon. The experimental frequency is plotted against the inverse of the radius in Figure 7.

We found no influence of the mass, length, width and rotation frequency of the nut on the frequency.

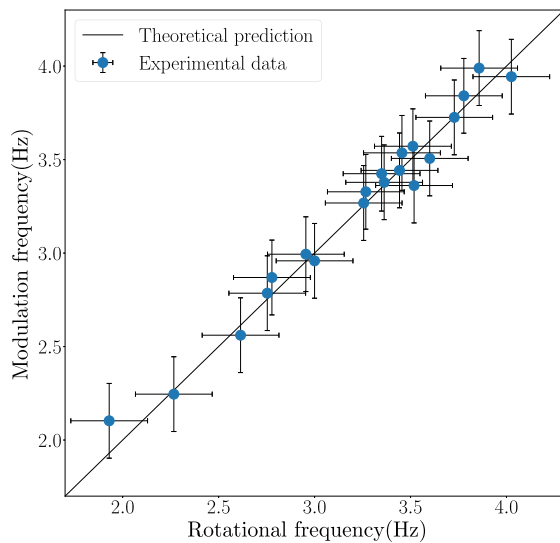


Fig. 5. Amplitude modulation frequency plotted against the macroscopic rotational frequency of the nut. The frequency was averaged over a period of 10 modulations for each experiment. The macroscopic rotational frequency was derived from videos of the balloon taken at 30 fps, using a regular camera.

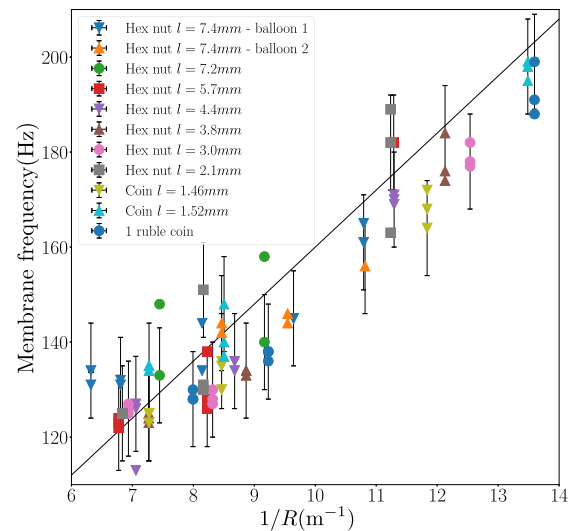
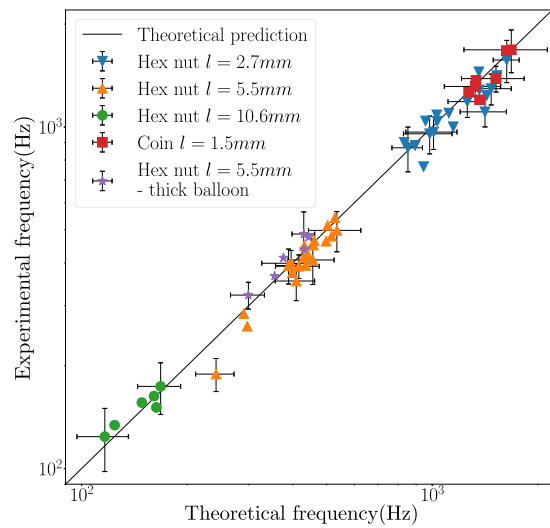


Fig. 7. (Top) Theoretical frequency of the sound plotted against the experimental main sound frequency. A wide range of balloon radius (3–15 cm) and different nuts/coins (see legend) were studied. Frequencies ranging from 100 Hz to little less than 2000 Hz were reached. The theoretical prediction is plotted as a black line. (Bottom) Lowest vibrational frequency of the balloon membrane plotted as a function of $1/R$. A wide range of balloon radius (3–15 cm) and different nuts/coins (see legend) were studied. Frequencies from 100 Hz to 200 Hz were reached.

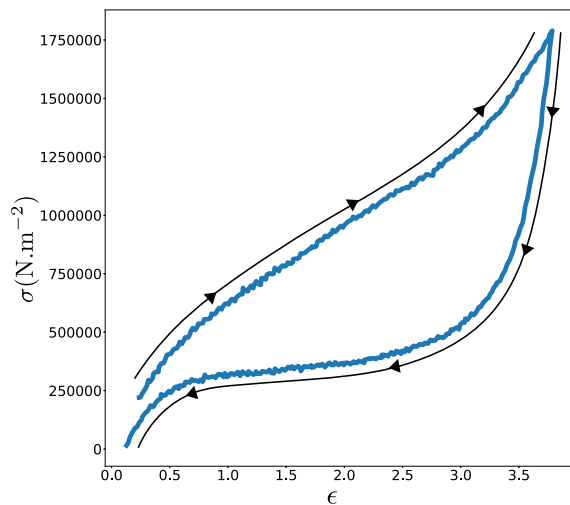


Fig. 6. Traction curve of an elastic rubber balloon. The stress σ is plotted as a function of the relative elongation of the band ϵ . Black arrows show the path of the deformation. Their is a non-linear stretching deformation (arrows upwards). The loosening (arrows downwards) does not follow the initial curve, a characteristic feature of the plastic domain.

4.6 Amplitude amplification

We plot the amplification due to the sound-box-like properties of the balloon against the frequency in Figure 8. The amplification is calculated by subtracting the amplitude

of the sound produced by the transducer alone from the sound of the transducer stuck to the balloon.

4.7 Amplitude of the main sound

In our experiments, we used the same type of balloon but varied its radius R as well as the parameters of the nut (mass m , width e and side length l).

Apx

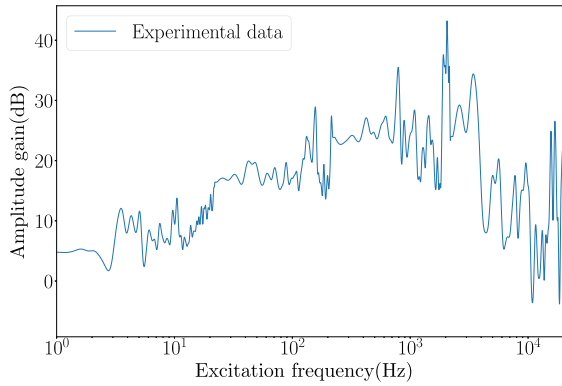


Fig. 8. Amplification (in dB) is plotted as function of the frequency at which a piezoelectric transducer excites the membrane. Amplification was derived from the difference of amplitude between the transducer vibrating alone and its action as it was put on the balloon. For convenience, a sweep of frequencies was performed. The distance to the microphone remains constant between the two sound samples.

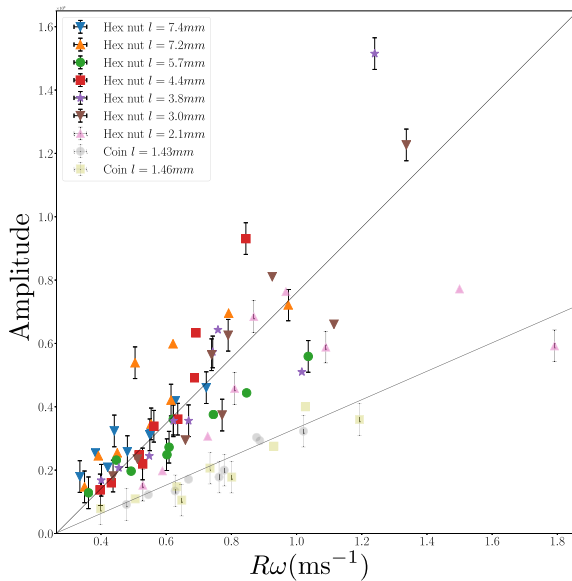


Fig. 9. The amplitude A plotted as a function of $R\omega$ for the same type of nuts, same rotation speeds and same balloon radii as above. Linear regressions are plotted for each type of nuts. Coin data points are plotted with low opacity due to deviation from the regression coefficient of the hex nuts.

We plot the amplitude A as a function of the translation velocity of the nut $R\omega$ in Figure 9.

We also plot the linear fits for all types of nuts.

5 Discussion

5.1 Rotation frequency of the nut

As shown in Figure 5, experiments attest that in our range of speeds and radii, the rotation frequency of the nut can be approximated with a good precision by the amplitude modulation's frequency.

In other experiments, we take the amplitude modulation's frequency as the rotational frequency, as it is significantly less time-consuming and experimentally constraining than tracking the nut on a video.

5.2 Main sound frequency – nut hits on membrane

Our model predicts a frequency varying as $f_{pred} = v/l$ using aforementioned notations. Assuming constant speed over the perimeter of the balloon this yields $f_{pred} = (2\pi R/l) \times f_{rot}$ where f_{rot} is the rotation frequency of the nut.

As shown at the top of Figure 7, experiments show a very good agreement between the predicts and experimental frequencies. We conclude that the main audible sound is indeed produced by the shocks of the nut's sides on the membrane of the balloon at a given frequency.

5.3 Secondary sound frequency – membrane vibration

As shown at the bottom of Figure 7, experimental frequencies are in good qualitative agreement with the predicted eigenfrequencies in [3] for both the lower and upper branch. The lower branch, very tightly packed, coincides with the main peak of the membrane's sound. The upper branch, more diluted, is harder to analyze, and corresponds to eigenmodes harder to excite with free boundary conditions.

Baker as well as our simple rope toy model predict a dependence of the eigenfrequencies in $f \propto 1/R$, which is experimentally verified and justifies our model.

5.4 Amplitude amplification

As shown in Figure 8, experiments show a roughly constant amplification over the audible range of +20 dB in the range of a 100 Hz to around 4000 Hz, which explains why we can hear the sound of the nut.

5.5 Amplitude of the primary sound

Results in Figure 9 show that for hex nuts, the amplitude of the sound produced collapses well under $R\omega$ (the translation velocity of the nut). Although we performed some in depth modelling of the amplitude, we were not able to provide any satisfactory account of experimental results.

A lower linear coefficient for coins as well as for the smallest nut at high speed suggest some saturation phenomena of the amplitude that could be due to the saturation of the deformation of the membrane (due to the smallness of the those nut's sides).

6 Dead ends and possible improvements

6.1 Higher order eigenfrequencies

Measuring higher order eigenfrequencies proves a very difficult task using Fourier transforms. Due to their smaller amplitudes they tend to overlap with other less significant signals or with one another, especially in the lower branch. A setup based on laser measurements as done by Kuo [8] would be more suited for such experiments.

6.2 Mechanical setup

Doing the experiments by hand induces non negligible uncertainties. We also used a mechanized setup via a lab shaker but did not present any such results here. Indeed, that setup has two major drawbacks: first of all it creates a nontrivial background noise, which can not easily be removed by simple algorithms, and masks most membrane frequencies. The other issue is that while using a mechanized setup we encountered a new phenomena of frequency modulation due to the forced excitations, which hinders our experiments. We believe this phenomena to occur the following way: to a given excitation frequency is associated a stable orbit in the balloon. If the nut is not initially on this orbit, it will move towards it due to the normal reaction on the balloon's surface. Due to inertia, it will however not stop at the stable orbit but overshoot it. This induces an up/down motion of the rotation plane, and thus a modulation of the sound. This is backed up by experimental data but we do not discuss it further here.

6.3 Influence of gas

Our model does not take into account the inner and outer gas. This has been studied by Kuo [8] but requires experimental data we do not have (such as the pressure difference across the membrane). We expect the gas to have no significant influence on the main sound's frequency, save for the heavy gases which could lead to non negligible dampening of the oscillations and thus a change in the harmonics' amplitude and frequency. We do expect a dependency of the membrane's eigenfrequencies with the gas's density.

6.4 Unexplained frequencies

During most experiments we consistently observe between 30 and 80 Hz a block of inaudible frequencies that seems relatively unaffected by experimental parameters. A quick analysis did not permit to determine whether this was only due to noise. We believe this block might be due to fine details on the nut's geometry but do not discuss it further here.

6.5 Theoretical model for the amplitude

Although results show an interesting collapse of the data of amplitude with $R\omega$ dependency and despite a thorough

research to provide a theoretical explanation of this dependency, we did not manage to provide any convincing proof. The issue residing in the large range of modelling hypotheses one can make which would require more experimental data with a wider range of different nuts to be tested.

7 Conclusion

In this article we have investigated the sound produced by a nut when it is made to roll inside a balloon, both experimentally and theoretically. After discussing the behavior of the nut on the membrane and explaining the amplitude modulation that one can hear when listening to the sound emitted we have studied the two main components of the sound emitted: membrane vibrations and the impact of the nut on the membrane. Regarding the membrane oscillations we showed experimentally that the frequency of the lower branch varies as the inverse of the radius of the balloon. Regarding the impact of the nut we derived the theoretical frequency of the sound that correlates very well with the main frequency component measured in the experiments. On the amplitude of the sound, we studied the effect of the balloon acting as a sound box and experimentally showed that in the range of frequencies at which the nut rolls the amplification of the sound is around 20 dB. For nuts, we experimentally showed a linear dependency of the amplitude of the sound emitted on the speed of nut.

This work is based on a problem proposed in the 2018 edition of the International Physicists' Tournament (IPT). We are grateful to Christophe Clanet, from the LadHyX, Guilhem Gallot from the LOB and Fabian Cadiz from the PMC at Ecole polytechnique for their fruitful suggestions and corrections brought to the core of this article. We also thank the teams from ParisSud at the French Physicists' Tournament (FPT) and the teams of Switzerland and Brazil at the IPT for the intense discussions we had in order to solve this problem.

Author contribution statement

Amaury Barral and Quentin Louis have contributed equally to this work.

References

1. H. Lamb, On the vibrations of an elastic sphere, *Proc. Lond. Math. Soc.* **1**, 189–212 (1881)
2. H. Lamb, On the vibrations of a spherical shell, *Proc. Lond. Math. Soc.* **1**, 50–56 (1882)
3. W.E. Baker, Axisymmetric modes of vibration of thin spherical shell, *J. Acoust. Soc. Am.* **33**, 1749–1758 (1961)
4. A. Silbiger, Nonaxisymmetric modes of vibration of thin spherical shells, *J. Acoust. Soc. Am.* **34**, 862 (1962)
5. A.R. Robinson, M.S. Zarghamee, A numerical method for analysis of free vibration of spherical shells, *AIAA J.* **5**, 1256–1261 (1967)

6. S.K. Panda, B.N. Singh, Nonlinear free vibration of spherical shell panel using higher order shear deformation theory—a finite element approach, *Int. J. Pres. Vessels Pip.* **86**, 373–383 (2009)
7. A. Goriely, M.B. Amar, Differential growth and instability in elastic shells, *Phys. Rev. Lett.* **94**, 198103 (2005)
8. K.A. Kuo et al., Small oscillations of a pressurized, elastic, spherical shell: model and experiments, *J. Sound Vib.* **359**, 168–178 (2015)

Cite this article as: Amaury Barral, Quentin Louis, Clément Brochet, Julie André, Anthony Guillen, Fang Goh, Angel Prieto, Thibault Guillet. Sound of a nut rolling inside an elastic rubber balloon, *Emergent Scientist* **3**, 6 (2019)

Bibliography

- [1] S. F. Hoerner. *Fluid-dynamic drag: practical information on aerodynamic drag and hydrodynamic resistance*. Hoerner Fluid Dynamics, 1965.
- [2] E. Achenbach. Distribution of local pressure and skin friction around a circular cylinder in cross-flow up to $re = 5 \times 10^6$. *Journal of Fluid Mechanics*, 34(4):625–639, 1968.
- [3] A. Thom. *An investigation of fluid flow in two dimensions*. HM Stationery Office, 1929.
- [4] Albert C Gross, Chester R Kyle, and Douglas J Malewicki. The aerodynamics of human-powered land vehicles. *Scientific American*, 249(6):142–152, 1983.
- [5] Yakovich Ilich Frenkel. Kinetic theory of liquids. 1955.
- [6] C. E. Brennen. *Cavitation and bubble dynamics*. Cambridge University Press, 2014.
- [7] J. P. Franc and J. M. Michel. *Fundamentals of cavitation*, volume 76. Springer science & Business media, 2006.
- [8] B. K. Ahn, T. K. Lee, H. T. Kim, and C. S. Lee. Experimental investigation of supercavitating flows. *International Journal of Naval Architecture and Ocean Engineering*, 4(2):123–131, 2012.
- [9] N. E. Joukowski. I. a modification of kirchhoff’s method of determining a two-dimensional motion of a fluid given a constant velocity along an unknown streamline. ii. determination of the motion of a fluid for any condition given on a streamline. *Rec. Math*, 25:121–278, 1890.
- [10] D. Riabouchinsky. On steady fluid motions with free surfaces. *Proceedings of the London Mathematical Society*, 2(1):206–215, 1921.
- [11] D. A. Efros. Hydrodynamic theory of two-dimensional flow with cavitation. In *Dokl. Akad. Nauk SSSR*, volume 51, pages 267–270, 1946.
- [12] T. Y. T. Wu, A. K. Whitney, and C. E. Brennen. Cavity-flow wall effects and correction rules. *Journal of Fluid Mechanics*, 49(2):223–256, 1971.
- [13] Z. Pan, A. Kiyama, Y. Tagawa, D. J. Daily, S. L. Thomson, R. Hurd, and T. T. Truscott. Cavitation onset caused by acceleration. *Proceedings of the National Academy of Sciences*, 114(32):8470–8474, 2017.
- [14] Lord Rayleigh. VIII. On the pressure developed in a liquid during the collapse of a spherical cavity. *The London, Edinburgh, and Dublin Philosophical Magazine and Journal of Science*, 34(200):94–98, 1917.
- [15] M. S. Plesset. The dynamics of cavitation bubbles. *Journal of applied mechanics*, 16:277–282, 1949.
- [16] M. S. Plesset and A. Prosperetti. Bubble Dynamics and Cavitation. *Annual Review Fluid Mechanics*, 9:145, 1977.
- [17] S. Gaggero, G. Tani, D. Villa, M. Viviani, P. Ausonio, P. Travi, G. Bizzarri, and F. Serra. Efficient and multi-objective cavitating propeller optimization: An application to a high-speed craft. *Applied Ocean Research*, 64:31–57, 2017.

- [18] R. E. A. Arndt. Recent advances in cavitation research. In *Advances in Hydrosience*, volume 12, pages 1–78. Elsevier, 1981.
- [19] J. R. Blake and D. C. Gibson. Cavitation bubbles near boundaries. *Annual review of fluid mechanics*, 19(1):99–123, 1987.
- [20] R. E. A. Arndt, R. L. Voigt Jr, J. P. Sinclair, P. Rodrique, and A. Ferreira. Cavitation erosion in hydroturbines. *Journal of Hydraulic Engineering*, 115(10):1297–1315, 1989.
- [21] M. Dular, B. Bachert, B. Stoffel, and B. Širok. Relationship between cavitation structures and cavitation damage. *Wear*, 257(11):1176–1184, 2004.
- [22] Y. Tomita and A. Shima. Mechanisms of impulsive pressure generation and damage pit formation by bubble collapse. *Journal of Fluid Mechanics*, 169:535–564, 1986.
- [23] W. Lauterborn and H. Bolle. Experimental investigations of cavitation-bubble collapse in the neighbourhood of a solid boundary. *Journal of Fluid Mechanics*, 72(2):391–399, 1975.
- [24] M. S. Plesset and R. B. Chapman. Collapse of an initially spherical vapour cavity in the neighbourhood of a solid boundary. *Journal of Fluid Mechanics*, 47(2):283–290, 1971.
- [25] R. Pecha and B. Gompf. Microimplosions: cavitation collapse and shock wave emission on a nanosecond time scale. *Physical review letters*, 84(6):1328, 2000.
- [26] G. E. Reisman, Y. C. Wang, and C. E. Brennen. Observations of shock waves in cloud cavitation. *Journal of Fluid Mechanics*, 355:255–283, 1998.
- [27] C. F. Naude and A. T. Ellis. On the mechanism of cavitation damage by nonhemispherical cavities collapsing in contact with a solid boundary. *Journal of Basic Engineering*, 83(4):648–656, 1961.
- [28] T. B. Benjamin and A. T. Ellis. The collapse of cavitation bubbles and the pressures thereby produced against solid boundaries. *Philosophical Transactions for the Royal Society of London. Series A, Mathematical and Physical Sciences*, pages 221–240, 1966.
- [29] A. Philipp and W. Lauterborn. Cavitation erosion by single laser-produced bubbles. *Journal of Fluid Mechanics*, 361:75–116, 1998.
- [30] R. Hickling and M. S. Plesset. Collapse and rebound of a spherical bubble in water. *The Physics of Fluids*, 7(1):7–14, 1964.
- [31] T. Covassin, R. Moran, and R. J. Elbin. Sex differences in reported concussion injury rates and time loss from participation: an update of the national collegiate athletic association injury surveillance program from 2004–2005 through 2008–2009. *Journal of athletic training*, 51(3):189–194, 2016.
- [32] G. W. Roberts, D. Allsop, and C. Bruton. The occult aftermath of boxing. *Journal of Neurology, Neurosurgery & Psychiatry*, 53(5):373–378, 1990.
- [33] J. Mez, D. H. Daneshvar, P. T. Kiernan, B. Abdolmohammadi, V. E. Alvarez, B. R. Huber, M. L. Alosco, T. M. Solomon, C. J. Nowinski, L. McHale, et al. Clinicopathological evaluation of chronic traumatic encephalopathy in players of american football. *Jama*, 318(4):360–370, 2017.

- [34] M. A. Kiraly and S. J. Kiraly. Traumatic brain injury and delayed sequelae: a review—traumatic brain injury and mild traumatic brain injury (concussion) are precursors to later-onset brain disorders, including early-onset dementia. *The Scientific World Journal*, 7:1768–1776, 2007.
- [35] B. E. Gavett, R. A. Stern, R. C. Cantu, C. J. Nowinski, and A. C. McKee. Mild traumatic brain injury: a risk factor for neurodegeneration. *Alzheimer’s research & therapy*, 2(3):18, 2010.
- [36] R. A. Stern, D. O. Riley, D. H. Daneshvar, C. J. Nowinski, R. C. Cantu, and A. C. McKee. Long-term consequences of repetitive brain trauma: chronic traumatic encephalopathy. *Pm&R*, 3(10):S460–S467, 2011.
- [37] E. S. Gurdjian, Verne L Roberts, and L M Thomas. Tolerance curves of acceleration and intracranial pressure and protective index in experimental head injury. *The Journal of Trauma*, 6:600–604, 1966.
- [38] H. R. Lissner, M. Lebow, and F. G. Evans. Experimental studies on the relation between acceleration and intracranial pressure changes in man. *Surgery, gynecology & obstetrics*, 111:329, 1960.
- [39] A. K. Ommaya, R. L. Grubb, and R. A. Naumann. Coup and contre-coup injury: observations on the mechanics of visible brain injuries in the rhesus monkey. *Journal of Neurosurgery*, 35(5):503–516, 1971.
- [40] E. J. Pellman, D. C. Viano, A. M. Tucker, I. R. Casson, and J. F. Waekerle. Concussion in Professional Football: Reconstruction of Game Impacts and Injuries. *Neurosurgery*, 53(4):799–814, 2003.
- [41] S. P. Broglio, B. Schnebal, J. J. Sosnoff, S. Shin, X. Feng, X. He, and J. Zimmerman. The Biomechanical Properties of Concussions in High School Football. *Med. Sci. Sports Exerc.*, 42(11):2064–2071, 2010.
- [42] W. N. Hardy, T. B. Khalil, and A. I. King. Literature review of head injury biomechanics. *International Journal of Impact Engineering*, 15(4):561–586, 1994.
- [43] T. El Sayed, A. Mota, F. Fraternali, and M. Ortiz. Biomechanics of traumatic brain injury. *Comput. Methods Appl. Mech. Engrg.*, 197:4692–4701, 2008.
- [44] B. K. Sreedhar, S. K. Albert, and A. B. Pandit. Cavitation damage: Theory and measurements - A review. *Wear*, 372-373:177–196, 2017.
- [45] Y. T. Wu and A. Adnan. Effect of Shock-Induced Cavitation Bubble Collapse on the damage in the Simulated Perineuronal Net of the Brain. *Scientific Reports*, 7(1):38–42, 2017.
- [46] P. Lubock and W. Goldsmith. Experimental Cavitation studies in a model head-neck system. *J. Biomechanics*, 13:1041–1052, 1980.
- [47] S. Rowson, G. Brolinson, M. Goforth, D. Dietter, and S. Duma. Linear and Angular Head Acceleration Measurements in Collegiate Football. *Journal of Biomechanical Engineering*, 131(6):061016, 2009.
- [48] S. M. Duma, S. J. Manoogian, W. R. Bussone, P. G. Brolinson, M. W. Goforth, J. J. Donnenwerth, R. M. Greenwald, J. J. Chu, and J. J. Crisco. Analysis of real-time head accelerations in collegiate football players. *Clinical Journal of Sport Medicine*, 15(1):3–8, 2005.

- [49] A. K. Ommaya. Mechanical properties of tissues of the nervous system. *Journal of Biomechanics*, 1(2):127–138, 2004.
- [50] M. Unnerbäck, J. T. Ottesen, and P. Reinstrup. ICP curve morphology and intracranial flow-volume changes: a simultaneous ICP and cine phase contrast MRI study in humans. *Acta Neurochirurgica*, 160(2):219–224, 2018.
- [51] C. J. J. Avezaat, J. H. M. Van Eijndhoven, and D. J. Wyper. Cerebrospinal fluid pulse pressure and intracranial volume-pressure relationships. *Journal of Neurology, Neurosurgery and Psychiatry*, 42(8):687–700, 1979.
- [52] M. Czosnyka and J. D. Pickard. Monitoring and interpretation of intracranial pressure. *Journal of Neurology, Neurosurgery and Psychiatry*, 75(6):813–821, 2004.
- [53] N. Bremond, M. Arora, S. M. Dammer, and D. Lohse. Interaction of cavitation bubbles on a wall. *Physics of Fluids*, 18(12), 2006.
- [54] N. Bremond, M. Arora, C. D. Ohl, and D. Lohse. Controlled multibubble surface cavitation. *Physical Review Letters*, 96(22):1–4, 2006.
- [55] N. A. Pelekasis, A. Gaki, A. Doinikov, and J. A. Tsamopoulos. *Secondary Bjerknes forces between two bubbles and the phenomenon of acoustic streamers*, volume 500. 2004.
- [56] R. Mettin, I. Akhatov, U. Parlitz, C. D. Ohl, and W. Lauterborn. Bjerknes forces between small cavitation bubbles in a strong acoustic field. *Physical Review E - Statistical Physics, Plasmas, Fluids, and Related Interdisciplinary Topics*, 56(3):2924–2931, 1997.
- [57] E. A. Neppiras and B. E. Noltingk. Cavitation produced by Ultrasonics. *Proceedings of the Physical Society. Section B*, 63(9):674–685, 1950.
- [58] G. E. Reisman, Y. C. Wang, and C. E. Brennen. Observations of shock waves in cloud cavitation. *Journal of Fluid Mechanics*, 355:255–283, 1998.
- [59] R. Pecha and B. Gompf. Microimplosions: Cavitation collapse and shock wave emission on a nanosecond time scale. *Physical Review Letters*, 84(6):1328–1330, 2000.
- [60] C. F. Naudé and A. T. Ellis. On the Mechanism of Cavitation Damage by Nonhemispherical Cavities Collapsing in Contact With a Solid Boundary. *Journal of Basic Engineering*, 83(4):648–656, 1961.
- [61] T. B. Benjamin and A. T. Ellis. The Collapse of Cavitation Bubbles and the Pressures thereby Produced against Solid Boundaries. *Philosophical Transactions of the Royal Society A: Mathematical, Physical and Engineering Sciences*, 260(1110):221–240, 1966.
- [62] A. Shima and Y. Tomita. Mechanism of Impulsive Pressure Generation and Damage Pit Formation by Cavitation Bubble Collapse. *Journal of the Society of Mechanical Engineers*, 90(819):164–169, 1985.
- [63] W. Lauterborn and A. Philipp. Cavitation erosion by single laser-produced bubbles. *Journal of Fluid Mechanics*, 361:75–116, 1998.
- [64] K. Ono, A. Kikuchi, M. Nakamura, H. Kobayashi, and N. Nakamura. Human head tolerance to sagittal impact-reliable estimation deduced from experimental head injury using subhuman primates and human cadaver skulls. *SAE Transactions*, pages 3837–3866, 1980.

- [65] Atsuhiko Nakagawa, Kazuyoshi Takayama, Miki Fujimura, Kaoruko Kato, Tomohiro Ohki, Atsushi Saito, and Teiji Tominaga. Pressure-dependent effect of shock waves on rat brain: induction of neuronal apoptosis mediated by a caspase-dependent pathway. *Journal of Neurosurgery*, 106:667–676, 2008.
- [66] C. Van Lierde, B. Depreitere, J. V. Sloten, R. Van Audekercke, G. Van Der Perre, and J. Goffin. Skull biomechanics - The energy absorbability of the human skull frontal bone during fracture under quasi-static loading. *Journal of Applied Biomaterials & Biomechanics*, 1:194–199, 2003.
- [67] M. Harrison. An experimental study of single bubble cavitation noise. *The Journal of the Acoustical Society of America*, 24(6):776–782, 1952.
- [68] E. Cramer and W. Lauterborn. Acoustic cavitation noise spectra. In *Mechanics and Physics of Bubbles in Liquids*, pages 209–214. Springer, 1982.
- [69] V. C. Suja and A. I. Barakat. A mathematical model for the sounds produced by knuckle cracking. *Scientific reports*, 8(1):4600, 2018.
- [70] S. L. Ceccio. Friction drag reduction of external flows with bubble and gas injection. *Annual Review of Fluid Mechanics*, 42:183–203, 2010.
- [71] E. Kawakami and R. E. A. Arndt. Investigation of the behavior of ventilated supercavities. *Journal of Fluids Engineering*, 133(9):091305, 2011.
- [72] L. Barbaca, B. Pearce, and P. Brandner. Experimental investigation of ventilated cavity flow over a 3d wall mounted fence. 2016.
- [73] E. Alyanak, V. Venkayya, R. Grandhi, and R. Penmetsa. Structural response and optimization of a supercavitating torpedo. *Finite Elements in Analysis and Design*, 41(6):563–582, 2005.
- [74] J. H. Choi, R. C. Penmetsa, and R. V. Grandhi. Shape optimization of the cavitator for a supercavitating torpedo. *Structural and Multidisciplinary Optimization*, 29(2):159–167, 2005.
- [75] E. Alyanak, R. Grandhi, and R. Penmetsa. Optimum design of a supercavitating torpedo considering overall size, shape, and structural configuration. *International Journal of Solids and Structures*, 43(3-4):642–657, 2006.
- [76] T. G. Lang and D. A. Daybell. Water tunnel tests of three vented hydrofoils in two-dimensional flow. *Journal of Ship Research*, 5(3):1–15, 1961.
- [77] Thomas G Lang. Base ventilated hydrofoil, February 12 1963. US Patent 3,077,173.
- [78] A. J. Acosta. Hydrofoils and hydrofoil craft. *Annual Review of Fluid Mechanics*, 5(1):161–184, 1973.
- [79] A. Rowe and J. M. Michel. Two-dimensional base-vented hydrofoils near a free surface: influence of the ventilation number. *Journal of Fluids Engineering*, 97(4):465–473, 1975.
- [80] R. Latorre. Ship hull drag reduction using bottom air injection. *Ocean engineering*, 24(2):161–175, 1997.
- [81] K. I. Matveev, T. J. Burnett, and A. E. Ockfen. Study of air-ventilated cavity under model hull on water surface. *Ocean Engineering*, 36(12-13):930–940, 2009.

- [82] V. N. Semenenko. Artificial supercavitation. physics and calculation. Technical report, Ukrainian Academy of Sciences Kiev Inst. of Hydromechanics, 2001.
- [83] V. N. Buyvol. Slender cavities in flows with perturbations. *Kiev: Naukova Dumka*, 1980.
- [84] G. V. Logvinovich. Hydrodynamics of flows with free boundaries, 1969.
- [85] R. N. Cox and W. A. Clayden. Air entrainment at the rear of a steady cavity. In *Proceedings of the Symposium on Cavitation in Hydrodynamics*, 1955.
- [86] L. A. Ephstein. Characteristics of ventilated cavities and some scale effects. In *Symp. IUTAM*, pages 173–185, 1981.
- [87] J. M. Michel. Some features of water flows with ventilated cavities. *ASME J. Fluids Eng*, 106(3):319–326, 1984.
- [88] C. E. Brennen. A numerical solution of axisymmetric cavity flows. *Journal of Fluid Mechanics*, 37(4):671–688, 1969.
- [89] A. H. Armstrong and K. G. Tadman. Axisymmetric cavity flow about ellipsoids. In *Proc. Joint Admiralty-US Navy Meeting on Hydroballistics*, 1954.
- [90] E. Y. Hsu and B. Perry. Water tunnel experiments on spheres in cavity flow. 1954.
- [91] P. Eisenberg and H. L. Pond. Water tunnel investigations of steady state cavities. Technical report, David Taylor Model Basin Washington DC, 1948.
- [92] I. U. Vakarelski, J. O. Marston, D. Y. C. Chan, and S. T. Thoroddsen. Drag reduction by leidenfrost vapor layers. *Physical review letters*, 106(21):214501, 2011.
- [93] M. M. Mansoor, I. U. Vakarelski, J. O. Marston, T. T. Truscott, and S. T. Thoroddsen. Stable-streamlined and helical cavities following the impact of leidenfrost spheres. *Journal of Fluid Mechanics*, 823:716–754, 2017.
- [94] R. C. Ackerberg. The effects of capillarity on free-streamline separation. *Journal of Fluid Mechanics*, 70(2):333–352, 1975.
- [95] V. H. Arakeri. Viscous effects on the position of cavitation separation from smooth bodies. *Journal of Fluid Mechanics*, 68(4):779–799, 1975.
- [96] I. U. Vakarelski, Derek Y. C. Chan, and S. T. Thoroddsen. Leidenfrost vapour layer moderation of the drag crisis and trajectories of superhydrophobic and hydrophilic spheres falling in water. *Soft Matter*, 10(31):5662–5668, 2014.
- [97] Sadatoshi Taneda. Visual observations of the flow past a sphere at reynolds numbers between 10 4 and 10 6. *Journal of Fluid Mechanics*, 85(1):187–192, 1978.
- [98] E. Achenbach. The effects of surface roughness and tunnel blockage on the flow past spheres. *Journal of fluid mechanics*, 65(1):113–125, 1974.
- [99] L. B. Torobin and W. H. Gauvin. The drag coefficients of single spheres moving in steady and accelerated motion in a turbulent fluid. *AIChE Journal*, 7(4):615–619, 1961.
- [100] A. M. Worthington and R. S. Cole. Impact with a liquid surface studied by the aid of instantaneous photography. paper ii. *Philosophical Transactions of the Royal Society of London. Series A, Containing Papers of a Mathematical or Physical Character*, 194:175–199, 1900.

- [101] G. Birkhoff and E.H. Zarantonello. Jets, wakes, and cavities. *Academic, New York*, 1957.
- [102] T. T. Truscott, B. P. Epps, and J. Belden. Water entry of projectiles. *Annual Review of Fluid Mechanics*, 46:355–378, 2014.
- [103] A. May. Vertical entry of missiles into water. *Journal of Applied Physics*, 23:1362–1372, 1952.
- [104] A. May. Water entry and the cavity-running behavior of missiles. Technical report, NAVSEA Hydroballistics Advisory Committee Silver Spring MD, 1975.
- [105] M. Lee, R.G. Longoria, and D.E. Wilson. Cavity dynamics in high-speed water entry. *Physics of Fluids*, 9(3):540–550, 1997.
- [106] T. Von Karman. The impact on seaplane floats during landing. 1929.
- [107] J.W. Glasheen and T.A. McMahon. Vertical water entry of disks at low froude numbers. *Physics of Fluids*, 8(8):2078–2083, 1996.
- [108] J.W. Glasheen and T.A. McMahon. A hydrodynamic model of locomotion in the basilisk lizard. *Nature*, 380(6572):340, 1996.
- [109] R. Bergmann, D. Van Der Meer, S. Gekle, A. Van Der Bos, and D. Lohse. Controlled impact of a disk on a water surface: cavity dynamics. *Journal of Fluid Mechanics*, 633:381–409, 2009.
- [110] N. J. Adams and C. B. Walter. Maximum diving depths of cape gannets. *The Condor*, 95:734–736, 1993.
- [111] P. A. Prince, N. Huin, and H. Weimerskirch. Diving depths of albatrosses. *Antarctic Science*, 6:353–354, 1994.
- [112] A. S. Brierley and P. G. Fernandes. Diving depths of northern gannets: acoustic observations of sula bassana from an autonomous underwater vehicle. *The Auk*, 118(2):529–534, 2001.
- [113] B. Chang, M. Croson, L. Straker, S. Gart, C. Dove, J. Gerwin, and S. Jung. How seabirds plunge-dive without injuries. *Proceedings of the National Academy of Sciences*, 113(43):12006–12011, 2016.
- [114] A. M. Worthington. *A study of splashes*. Longmans, Green, and Company, 1908.
- [115] V. Duclaux, F. Caillé, C. Duez, C. Ybert, L. Bocquet, and C. Clanet. Dynamics of transient cavities. *Journal of Fluid Mechanics*, 591:1–19, 2007.
- [116] S. Gaudet. Numerical simulation of circular disks entering the free surface of a fluid. *Physics of Fluids*, 10:2489–2499, 1998.
- [117] D. Gilbarg and R. A. Anderson. Influence of atmospheric pressure on the phenomena accompanying the entry of spheres into water. *Journal of Applied Physics*, 19:127–139, 1948.
- [118] C. Duez, C. Ybert, C. Clanet, and L. Bocquet. Making a splash with water repellency. *Nature Physics*, 3:180–183, 2007.
- [119] J. M. Aristoff and J. W. M. Bush. Water entry of small hydrophobic spheres. *Journal of Fluid Mechanics*, 619:45–78, 2009.

-
- [120] S. Gekle and J. M. Gordillo. Generation and breakup of Worthington jets after cavity collapse. part 1. jet formation. *Journal of Fluid Mechanics*, 663:293–330, 2010.
- [121] K. G. Bodily, S. J. Carlson, and T. T. Truscott. The water entry of slender axisymmetric bodies. *Physics of Fluids*, 26(7):072108, 2014.
- [122] W. Xia, C. Wang, Y. Wei, and J. Li. Experimental study on water entry of inclined circular cylinders with horizontal velocities. *International Journal of Multiphase Flow*, 2019.
- [123] N. Kim and H. Park. Water entry of rounded cylindrical bodies with different aspect ratios and surface conditions. *Journal of Fluid Mechanics*, 863:757–788, 2019.
- [124] A. Andersen, U. Pesavento, and Z. J. Wang. Unsteady aerodynamics of fluttering and tumbling plates. *Journal of Fluid Mechanics*, 541:65–90, 2005.
- [125] K. Ellingsen and F. Risso. On the rise of an ellipsoidal bubble in water: oscillatory paths and liquid-induced velocity. *Journal of Fluid Mechanics*, 440:235–268, 2001.
- [126] P. C. Fernandes, P. Ern, F. Risso, and J. Magnaudet. On the zigzag dynamics of freely moving axisymmetric bodies. *Physics of Fluids*, 17(9):098107, 2005.
- [127] P. Ern, F. Risso, D. Fabre, and J. Magnaudet. Wake-induced oscillatory paths of bodies freely rising or falling in fluids. *Annual Review of Fluid Mechanics*, 44:97–121, 2012.
- [128] S. F. Hoerner and H. V. Borst. *Fluid-dynamic lift: practical information on aerodynamic and hydrodynamic lift*. LA Hoerner, 1985.
- [129] C. Cohen, B. Darbois-TeXier, G. Dupeux, E. Brunel, D. Quéré, and C. Clanet. The aerodynamic wall. *Proc. R. Soc. A*, 470:20130497, 2014.

Titre : Cavitation & Supercavitation : Obtenir un projectile profilé stable

Mots clés : cavitation, supercavitation, dynamique de bulles, cavité ventilée, réduction de trainée, entrée dans l'eau, instabilité

Résumé : La supercavitation utilise le changement de phase du liquide-vapeur au mouvement rapide d'un projectile pour le profiler et ainsi réduire sa trainée. Dans cette thèse, nous abordons la supercavitation sous différents aspects : la cavitation induite par accélération en environnement confiné, la réduction de trainée engendrée par la cavité d'air et la stabilité des trajectoires des objets ainsi profilés. Plus précisément, nous nous intéressons dans un premier temps, à la fois expérimentalement et théoriquement, à la croissance des bulles de cavitation. Après avoir montré que cette croissance n'est possible que dans une enceinte déformable, nous prouvons, dans le cas particulier où la dépression à l'origine de l'apparition de ces bulles est transitoire, que leur dynamique suit l'équation de Rayleigh-Plesset et que leur rayon maximal peut être prédit analytiquement. Si la vitesse du projectile est assez grande, les bulles de cavitation grossissent et coalescent pour former une unique

bulle, accrochée à la surface du projectile et située dans son sillage: c'est le régime dit de supercavitation. Nous montrons que ce régime peut être reproduit dans un canal hydraulique "classique", à faible vitesse, en injectant de l'air à la surface du projectile. Avec ce dispositif expérimental, nous démontrons que la taille relative de la bulle est uniquement déterminée par un paramètre adimensionnel. Dans le cas d'une sphère, nous mesurons la modification de trainée ainsi engendrée. Enfin, le système global { sphère + bulle } peut être considéré comme un projectile profilé de densité inhomogène. Nous montrons que de tels projectiles profilés, suivent des trajectoires courbes après leur impact dans l'eau. Nous démontrons, à la fois expérimentalement et théoriquement, que la forme de leur trajectoire est déterminée par leur vitesse d'impact, leur forme et la position de leur centre de gravité.

Title : Cavitation & Supercavitation: From a bluff to a stable streamlined projectile

Keywords : cavitation, supercavitation, bubble dynamics, ventilated cavity, drag reduction, water entry, instability

Abstract : Supercavitation uses the phase transition liquid-gaseous, triggered by the fast motion of a projectile, to streamline its shape and reduce its drag. In this thesis, we address several aspects of supercavitation: cavitation triggered by acceleration in a confined geometry, drag reduction induced by the air cavity and the stability of the trajectory of such streamlined projectiles. More precisely, we first study both experimentally and theoretically the growth of cavitation bubbles. After showing that their growth is uniquely possible in a deformable container, we prove, in the case of a transient pressure drop, that the dynamic of the bubbles follows the Rayleigh-Plesset equation and that their maximum radius can analytically be predicted. If the velocity of the projectile is high enough, the bubbles grow and coalesce to form a large bubble pinned at the surface of the projectile and lo-

cated in its wake: this is the so-called supercavitation regime. We show that this regime can be mimicked in "regular", low velocity, hydrodynamic tunnel via air injection at the surface of the projectile. In this set-up, we demonstrate that the relative size of the bubble is governed by a unique dimensionless parameter. In the case of a sphere, we measure the drag modification induced by the presence of the bubble. Finally, the overall system { sphere + bubble } is analogous to a inhomogeneous streamlined projectile. We show that such streamlined projectiles can follow curved paths, following their impact on water. We demonstrate, both experimentally and theoretically, that the morphology of their trajectory is governed by the impact velocity, their shape and the position of the center of mass of the projectile.